THE EFFECTS OF SURFACTANTS ON FREE-SURFACE FLOWS

Thesis by

Amy E. Warncke

In Partial Fulfillment of the Requirements

for the Degree of

Doctor of Philosophy

California Institute of Technology

Pasadena, California

1997

(Submitted May 22, 1997)

Dedicated to my parents,

Ronald and Deborah Warncke

and to my future husband

John W. Lang

Acknowledgments

First of all, I would like to thank my advisor, Mory Gharib, for his support and guidance over these past four years. Also, Thomas Roesgen for his help in developing some of the experimental techniques I utilized, as well for the guidance he also lent me. I would like to thank all those in Mory's research group for the various times when I had a question, someone was usually around who knew the answer. And, I would like to acknowledge my fellow classmates -- in particular those with whom I have shared an office with through the years -- for their friendship and advice as well.

In addition I would like to thank Manooch Koochesfahani, without whose initial guidance as an undergraduate I would never have discovered the desire to research fluid mechanics, and without whom I would not have been lead to attend Caltech.

Last, but not least, I am grateful for the support and guidance through the years by my parents, Ronald and Deborah Warncke, and for the unwavering faith and support from my fiancé, John W. Lang, often when I needed it the most.

Financial support for the research came from the Office of Naval Research (Contract # N00014-94-1-0596). Also, the National Science Foundation and Zonta International Amelia Earhart Fellowship Award provided financial support during my graduate studies.

Abstract

This experimental investigation into the nature of free surface flows is to study the effects of surfactants on the boundary condition at the free surface and the resulting flow field. In particular, the flow field associated with a stationary Reynolds ridge was investigated as well as the wake behind a surface-piercing cylinder, where experimental techniques such as Digital Particle Image Velocimetry and a new surface slope measurement technique were utilized.

Results show a large change in the flow field in the free-surface vicinity depending on the presence of surface tension gradients and thus shear stresses at the free surface. In particular, the boundary layer beneath a Reynolds ridge was measured and it is shown that the primary source of vorticity at the free surface can be attributed to the free surface deceleration at the ridge. Also, in the wake of the cylinder, depending on the surface condition, the connection of the shedding vortex filaments was found to be greatly altered with the propensity of surface tension gradients to redirect the vorticity near the free surface to that of the surface-parallel component. Thus it is shown that surfactants can dramatically alter the flow field due to the change in the free-surface boundary condition and resulting vorticity generation and conversion in the vicinity of the free surface.

Table of Contents

List of Figures

Chapter 1

Introduction

1.1 Background

1.1.1 Surfactants

In recent years, the role that surfactants can play, with respect to the dynamics of free-surface flows, has been realized to be of significant importance in understanding the behavior of vorticity and turbulence in general at a free surface. Surfactants, or surface contaminants, have the tendency to reduce the surface tension proportional to the respective molecular concentration at the free surface. Surfactants also tend to have an affinity to stay at a free surface. Soluble surfactants have a molecular structure such that they have both a hydrophilic (water-liking) and hydrophobic (water-hating) end, and insoluble surfactants, such as oil, do not mix with the fluid medium and collect at the free surface. The molecules then tend to arrange themselves with the hydrophobic end out of the water free surface and spread to a monolayer, or one molecule thick sheet across the free surface. As a result, the overall concentration of a surfactant within the bulk of the fluid may be minimal, while that at the free surface is of important significance. Thus, small amounts of surface-active agent need only be present to contaminate a free surface.

The damping, or calming effect, that surfactants can have on waves at a free surface is a well known fact. Ancient mariners used to dump vats of oil over the sides of ships during storms to calm the waves and allow safer passage through the rough seas. Also, Benjamin Franklin once dumped oil onto the surface of a small lake during a storm to demonstrate the damping of the waves, or as more commonly known these days the Marangoni effect. He also was the first to speculate that the oil in fact spreads to a film

only one molecule in thickness. This damping is due to the fact that when a wave deforms at the free surface, the monolayer acts like an elastic membrane such that a stretching of the free surface causes the molecular concentration of the surfactant to decrease due to the larger surface area caused by the free-surface deformation. This lower concentration in the stretched area results in a surface tension gradient which pulls on the free surface causing a force in the opposite direction to the deforming motion and damping the wave.

In addition to the differences between insoluble and soluble surfactants, the chemical and physical properties of surfactant films can vary dramatically. In general, the characteristics of films, such as the dilitational and shear viscosities, are difficult to measure as they generally depend on the local concentration and often exhibit visco-elastic effects. Finally when trying to study the films that occur naturally, such as that at the ocean surface, it is difficult if not impossible to fully understand the properties of such films due to the variation in composition.

1.1.2 Ship Wakes

The particular interest of surfactants these days is their relevance to free-surface flows at the ocean surface, in particular to that of ship wakes. Naturally occurring surfactants, many of biological nature, abound at our ocean surfaces and thus can play a large role in the nature of the wake that is generated behind a ship. One must keep in mind that typical Reynolds numbers of these wakes are on the order of 10^8 and along with the complexity of these flow fields, their full comprehension is difficult to grasp. As a result, various components of the wake need to be understood and explained before a full understanding of these flows can be gained.

Of significant importance is the fact that the features of these wakes do not decay as rapidly as one might expect. This results in the fact that surface signatures of these wakes persist for many miles behind these ships and in many cases are observable by satellite imaging (see Figure 1.1). What in fact makes these wakes most visible is the formation of

two large bands of concentrated surfactants that form parallel to the ship's direction of motion, or on both sides of the wake. Within these bands ocean waves are damped to a significantly larger extent, thus making them easily observable when looking at the ocean surface.

The formation of these bands, see Figure 1.2, is due to the fact that the wake of a ship consists of an underlying flow field made up of two counter-rotating vortical structures whose axis are parallel to the free surface and to that of the ship's direction of travel. The formation of these structures, due to the shedding of the boundary layer from the ship's hull, results in an upwelling in the center of the wake which brings up fresh, clean water from the bulk fluid and pushes to the side the contaminated water that consisted of the ocean surface. Keeping in mind that in an unbounded domain such as the ocean surface, there are no walls as in the experimental case which contain the film and provide a means of compressing it. Thus in the unbounded domain a minimum tangential velocity at the surface is required to break the film apart and create a Reynolds ridge, where this velocity is equivalent to the speed of sound of the surfactant film. It has been observed that this velocity is on the order of 2 m/s, and is dependent on the elasticity and thickness of the film. The demarcation between this clean surface and that of the contaminated water surface is marked by what is known as a Reynolds ridge. The contaminated surface, or bands into which the surfactants have been compressed, damp any waves in that area making the distinction between the clean surface easily visible.

1.1.3 The Reynolds Ridge

A Reynolds ridge is a free-surface flow phenomenon that was actually first documented by Henry David Thoreau. (See Figure 1.3 for a schematic of the flow field.) While studying a small stream he noticed that when there was a slight fixed obstruction in the flow at the free surface, i.e. a twig or leaf, a small "ridge" appeared on the water surface upstream of the obstruction. Reynolds was the first to account for the fact that a

surface tension gradient exists at the ridge, where in the case of the obstructed flow the obstruction allowed for the collection of the surfactants and the formation of a monolayer upstream of it. He also realized that in the case of a spreading film, a ridge is also formed at the leading edge of the spreading monolayer. However, it was not until 1970 that McCutchen hypothesized that a boundary layer was formed beneath the film and that the ridge, or slight rise in surface height ahead of the monolayer, was due to the retardation of the flow within the boundary layer.

Harper & Dixon (1974) formed the first quantitative theory of the flow in the vicinity of a stationary Reynolds ridge met by an oncoming uniform flow. They derived an analytical approximation of the flow field in the boundary layer and also derived theoretical surface height profiles across the ridge using simplified boundary conditions at the free surface and thin airfoil theory. Due to the minuscule nature of the Reynolds ridge, the first experimental investigations of the ridge included only shadowgraph (Sellin,1968) and surface slope measurements (Scott,1982) using the reflection of a laser beam off the free surface. Scott's slope measurements found good agreement with Harper & Dixon's predictions.

1.1.4 Other Previous Work

To break down the complexity of the ship wake problem, a lot of work has been done to study simple free-surface interactions of vortical flows. However, only a few experimental/computational studies have looked at the presence of surfactants on the free surface. Gharib & Weigand (1996) looked at the connection of an inclined vortex ring to a free surface where the free surface was both clean and contaminated. They found that in the clean case the ring connected and then subsequently formed two smaller rings. In the contaminated case, the bottom of the ring did not connect with the free surface as it did in the clean case to form two rings, rather it rebounded slightly and just the one ring remained. Hirsa et al. (1995) experimentally looked at the free-surface interaction of a

vortex pair aligned parallel to the free surface, while computationally this problem was studied by Tryggvason et al. (1992) and Tsai & Yue (1995). It was observed that in the contaminated case, opposite sign vorticity was generated at the free surface similar to that of a solid boundary. While in the clean case, no opposite sign vorticity was generated at the boundary. Finally, Willert (1992) looked at the free-surface interaction of "modulated vortex pairs." Because of the bends in the vortex tubes, a connection process occurs similar to that observed by Gharib & Weigand when the free surface is clean. However, in the contaminated case this connection process did not occur in nearly the same manner. Instead the opposite sign vorticity generated, at the free surface due to the boundary layer formed starting at the Reynolds ridges generated due to the cleaning of the surface by the overall flow field of the vortex pairs, formed "rings" which connected to the free surface. While due to the strain field generated in the boundary layer, the modulated vortex pairs did not connect to the surface as observed in the clean case.

1.2 Objective

Thus, the goal of this study is to gain insight into more of the basic behavior of the vorticity distribution at the free surface with the presence of surfactants. This insight will help explain the nature not only of the overall flow field present in ship wakes, but also the behavior of vorticity generation and conversion near the free surface due to the presence of surfactants in turbulent flows. On the finer scales, turbulence is composed of nothing more than the interaction of small eddies or vortex filaments. To understand then the nature of turbulence for various free-surface boundary conditions, it is best first to understand the more elemental flows.

First, to look at the nature of the vorticity generation in the vicinity of the Reynolds ridge is of significant importance. To understand the basic mechanism behind this vorticity generation believed to exist in the boundary layer and the connection between the surface tension gradient is an important first step. Also, flows such as that of convecting surface

normal vortex filaments found in the wake of a surface-piercing cylinder, and how the vortex connection at the free surface changes depending on the free-surface boundary condition need also to be understood.

However, due to the minuscule nature of the Reynolds ridge, experimental work to understand this flow field has been difficult to conduct. Thus, with the latest developments in Digital Particle Image Velocimetry (DPIV) to measure this free-surface boundary layer is no longer impossible. Along with the development of new optical techniques to measure the free surface slope and surface tension gradient simultaneously, insight can be gained into the mechanism of vorticity generation at the free surface which results in a boundary layer. In addition, the wake generated by a surface-piercing cylinder is also studied. The basic flow field involved, that of surface normal vortex filaments shed from the cylinder, will allow an elemental study of the presence of surfactants on the near-surface vorticity distribution of this simple bluff body wake.

Chapter 2

Theory

2.1 Coordinate System

When studying a free surface, which by definition is free to move and deform, it is best to define a local curvilinear coordinate system as that depicted in Figure 2.1. Here **s** is the surface tangential coordinate, **r** is the surface normal coordinate, and **z** is normal to the plane defined by **r** and **s**. In the case presented, curvature will only be assumed to exist in the **rs** plane, and the radius of curvature of the free surface at a point is denoted by R. In addition, the angle of the free surface is also measured with respect to **g**, the gravity vector pointing downward, and is denoted by θ.

However, for some of the results to be presented it is realized that the free surface deformation with respect to the magnitude of the velocity field is negligible. Most results will be presented where a global orthogonal **xyz** coordinate system (see Figure 2.2) is used, with **s** corresponding to **x** and **r** corresponding to **y** at the free surface. In this coordinate system u,, v, and w are the corresponding velocity components of the velocity vector **u**. This results in a vorticity vector defined as

$$\omega = \nabla \times \mathbf{u} = \begin{pmatrix} \frac{\partial w}{\partial y} - \frac{\partial v}{\partial z} \\ \frac{\partial u}{\partial z} - \frac{\partial w}{\partial x} \\ \frac{\partial v}{\partial x} - \frac{\partial u}{\partial y} \end{pmatrix} = \begin{pmatrix} \omega_x \\ \omega_y \\ \omega_z \end{pmatrix} \tag{2.1}$$

2.2 The Free Surface

2.2.1 Boundary Conditions

First of all, for the global coordinate system where surface deformations are small and the surface is considered flat, the boundary conditions and the resulting vorticity at the free surface must be understood. There are three cases which may be considered: (1) the solid stationary boundary (the case of a moving solid boundary will not be considered), (2) the clean free surface, and (3) the contaminated free surface.

In the case of a solid surface with the no-slip condition in effect, by definition then both the u and w components of the velocity field must be zero at the surface. Using these conditions in the equation for the vorticity, the result is that ω_y is equal to zero. Thus at a solid wall only surface parallel vorticity can exist at the surface.

In the case of a clean free surface, or by definition a 'shear free' surface, the shear stress at the surface is equal to zero. Or as written below for a fluid element (see Figure 2.1) where the y face represents the free surface

$$\tau_{yx} = \mu\left(\frac{\partial u}{\partial y} + \frac{\partial v}{\partial x}\right) \cong \mu\frac{\partial u}{\partial y} = 0 \tag{2.2}$$

$$\tau_{yz} = \mu\left(\frac{\partial w}{\partial y} + \frac{\partial v}{\partial z}\right) \cong \mu\frac{\partial w}{\partial y} = 0 \tag{2.3}$$

where the gradients in the v velocity component are approximately zero due to the flat free surface assumption. The result is then that ω_x and ω_z are equal to zero. Thus for a clean free surface with no curvature only surface normal vorticity can exist at the free surface. The significance of this condition is that vortex filaments may exist whose vorticity is parallel to the free surface, but only in a region just below it. In addition, because vortex filaments can not terminate within a fluid due to the laws of vortex dynamics, these filaments will connect normally at the free surface.

Finally in the case of a contaminated surface, where the presence of surfactants can result in surface tension gradients which in turn must be balanced by shear stresses in the fluid, the zero shear stress condition is no longer imposed and all components of vorticity may be present at the free surface. Returning then to the curvilinear coordinate system where the surface may have significant curvature, the shear stress is defined as

$$\tau_{rs} = \mu\left[\frac{\partial u_s}{\partial r} - \frac{u_s}{R+r} + \frac{R}{R+r}\left(\frac{\partial u_r}{\partial s}\right)\right]_{r=0} \tag{2.4}$$

In turn, this shear stress must be balanced at the free surface such that the boundary condition is

$$\tau_{rs} = \tau_{AIR} + \frac{\partial \sigma}{\partial s} + \left(\kappa^s + \mu^s\right)\frac{\partial^2 u_s}{\partial s^2} \tag{2.5}$$

where σ is the surface tension and κ^s and μ^s are correspondingly the dilitational and shear viscosities of the monolayer film as set forth by Edwards et al. (1991) (note in general for most surfactant films $\kappa^s > \mu^s$). Also, their values are highly dependent on the molecular concentration of the surfactant in that their corresponding magnitudes decrease with decreasing concentration.

2.2.2 Vorticity and Vorticity Flux

The parallel vorticity may also be written using the local curvilinear coordinate system at the free surface as

$$\omega_z = \left[-\frac{\partial u_s}{\partial r} - \frac{u_s}{R+r} + \frac{R}{R+r}\left(\frac{\partial u_r}{\partial s}\right)\right]_{r=0} \tag{2.6}$$

Next using (2.4) and (2.5) the parallel vorticity may be rewritten as

$$\omega_z = -\frac{\tau_{AIR}}{\mu} - \frac{1}{\mu}\left(\frac{\partial \sigma}{\partial s} + \left(\kappa^s + \mu^s\right)\frac{\partial^2 u_s}{\partial s^2}\right) - 2\frac{u_s}{R} + 2\frac{\partial u_r}{\partial s} \tag{2.7}$$

This equation, as shown in part by Lugt (1987,1988), Lundgren (1988) and Gharib & Weigand (1995), manifests the four sources of vorticity that can be present at a free surface. These are:

(1) the shear stress imposed by the adjoining fluid which in the case of air is considered negligible,

(2) effects of surfactants from surface tension gradients and acceleration/ deceleration of the monolayer film,

(3) curvature of the free surface, and

(4) vertical motion of the free surface which is only present in the case of unsteady flows.

Thus all parallel vorticity at a free surface must be attributed to one of these sources.

Using the same coordinate system, the vorticity flux or vorticity transport equation at a free surface is derived (Rood, 1995 and Gharib, 1992). The equation of continuity in a curvilinear coordinate system (evaluated at the free surface) is written as

$$\frac{\partial u_s}{\partial s} + \frac{\partial u_r}{\partial r} + \frac{u_r}{R} = 0 \tag{2.8}$$

and the s-momentum equation as

$$\frac{\partial u_s}{\partial t} + u_s \frac{\partial u_s}{\partial s} + u_r \frac{\partial u_s}{\partial r} + \frac{u_s u_r}{R} = -\frac{1}{\rho}\frac{\partial p}{\partial s} - g\cos\theta + \nu\left(\frac{\partial^2 u_s}{\partial s^2} + \frac{\partial^2 u_s}{\partial r^2} + \frac{1}{R}\frac{\partial u_s}{\partial r} - \frac{u_s}{R^2} + \frac{2}{R}\frac{\partial u_r}{\partial s} - \frac{u_r}{R^2}\frac{\partial R}{\partial s} \right) \tag{2.9}$$

which was first derived by Lugt (1987).

Differentiating (2.6) with respect to r, one derives an equation for the surface-parallel vorticity flux at the free surface as

$$\nu\left[\frac{\partial \omega_z}{\partial r}\right]_{r=0} = -\frac{\partial^2 u_s}{\partial r^2} - \frac{1}{R}\frac{\partial u_s}{\partial r} + \frac{u_s}{R^2} - \frac{1}{R}\frac{\partial u_r}{\partial s} + \frac{\partial^2 u_r}{\partial r \partial s} \tag{2.10}$$

Next, differentiating the continuity equation with respect to s and evaluating it at the free surface (r=0), the last term in (2.10) is also represented as

$$\frac{\partial^2 u_r}{\partial r \partial s} = \frac{u_r}{R^2}\frac{\partial R}{\partial s} - \frac{1}{R}\frac{\partial u_r}{\partial s} - \frac{\partial^2 u_s}{\partial s^2} \tag{2.11}$$

Substituting (2.11) into (2.10) one realizes that the long string of terms on the right-hand side is equal to the negative of the bracketed terms in the s-momentum equation and thus

$$-\nu\left[\frac{\partial \omega_z}{\partial r}\right]_{r=0} = \frac{\partial u_s}{\partial t} + u_s\frac{\partial u_s}{\partial s} + u_r\left(\frac{\partial u_s}{\partial r} + \frac{u_s}{R}\right) + \frac{1}{\rho}\frac{\partial p}{\partial s} + g\cos\theta \tag{2.12}$$

Because the coordinate system is defined locally with the origin on the free surface and moving with it, u_r is equal to zero and the above equation becomes

$$\nu\left[\frac{\partial \omega_z}{\partial r}\right]_{r=0} = -\left(\frac{\partial u_s}{\partial t} + u_s\frac{\partial u_s}{\partial s} + \frac{1}{\rho}\frac{\partial p}{\partial s} + g\cos\theta\right) \tag{2.13}$$

This is the vorticity transport equation at a free surface where a positive value of the right hand side denotes a positive flux of positive vorticity at the free surface into the fluid. Note as well, that the right hand side can be categorized into an unsteady term and a change of total head, H, along s where H is defined as

$$H = \frac{1}{2}u_s^2 + \frac{p}{\rho} + gs\cos\theta \tag{2.14}$$

2.2.3 The Reynolds Ridge

In the case of a Reynolds ridge which is stationary in a free stream flow as shown in Figure 1.3, the flow is considered steady. As a result, the time dependent term in (2.13) is neglected and the vorticity flux equation for this particular flow field is written as

$$\nu\left[\frac{\partial \omega_z}{\partial r}\right]_{r=0} = -u_s\frac{\partial u_s}{\partial s} - \frac{1}{\rho}\frac{\partial p}{\partial s} - g\cos\theta \tag{2.15}$$

where only the change in total head is significant. These terms can be categorized as those from acceleration/deceleration and curvature, where the pressure term is dependent on curvature because the pressure at the free surface is defined as

$$p \cong p_{ATM} - \frac{\sigma}{R} - \frac{\kappa^s}{R}\frac{\partial u_s}{\partial s} \tag{2.16}$$

where the equations set forth in Edwards et al. were used to derive this equation. Thus if the curvature is small, i.e. θ approximately ninety degrees and R>>1, the vorticity transport equation can be rewritten as

$$\nu\left[\frac{\partial \omega_z}{\partial r}\right]_{r=0} \cong -u_s\frac{\partial u_s}{\partial s} \tag{2.17}$$

2.3 Non-Dimensional Parameters

2.3.1 The Reynolds Ridge

Harper and Dixon were the first to non-dimensionalize the flow field for a stationary Reynolds ridge. The Reynolds number, which inherently represents the balance between inertial and viscous forces, they defined as

$$Re = \left(\frac{\Pi_f}{\mu U}\right)^2 \tag{2.18}$$

where Π_f is the surface pressure of the contaminated surface. Surface pressure is defined by $\Pi=\sigma_0-\sigma$ where σ_0 is the surface tension of the uncontaminated fluid or clean free surface. However, due to the nature of this flow field, where the balance is occurring between inertial, viscous, and surface tension effects, it is difficult to say that the above definition provides any meaning in the traditional sense of the Reynolds number where Re=UL/ν, for some length scale L. For (2.18) if the free stream velocity U is increased, the Reynolds number decreases, which is the opposite of what is expected.

Another Reynolds number which may be defined is based on the boundary layer flow which evolves beneath the ridge. In keeping with traditional boundary layer theory the Reynolds number is defined as

$$Re_x = \frac{Ux}{\nu} \tag{2.19}$$

where x is the downstream distance from the origin of the boundary layer, or leading edge of the surfactant film.

2.3.2 The Surface-Piercing Cylinder

When studying the wake of a surface-piercing cylinder, the definition of the Reynolds number is of the traditional sense where

$$Re_d = \frac{Ud}{\nu} \tag{2.20}$$

and d is the diameter of the cylinder. In addition, the Froude number is also defined based on the diameter of the cylinder as

$$Fr_d = \frac{U}{\sqrt{gd}} \tag{2.21}$$

Finally, for this flow field surface tension effects can also be considered a factor, and a Weber number is defined as

$$We_d = \frac{\rho U^2 d}{\sigma} \tag{2.22}$$

Chapter 3

Experimental Procedure

3.1 Generating the Flow Field

3.1.1 Water Tunnel Facility

To generate the flow field of a stationary Reynolds ridge, a free-surface recirculating water tunnel facility was chosen. The tunnel, as shown in Figure 3.1, was manufactured by Engineering Laboratory Design, Inc. and has a 6" wide by 6" high Plexiglas test section which is 30" long. Additional optical access is also available through a downstream Plexiglas window. The tunnel itself is constructed of laminated fiberglass reinforced plastic in which the interior flow sections are glass smooth. Flow straighteners, just downstream of the plenum, consist of a series of perforated plates, screens, and honeycomb after which a contraction section is placed to accelerate the flow through the test section. The flow is generated by a 1/2 HP centrifugal pump capable of delivering 112 GPM, and is controlled with a manual speed control potentiometer to adjust the test section velocity. The tunnel was filled with approximately 30 gallons of distilled water to obtain the highest possible water purity.

3.1.2 Surfactant Monolayer

The surfactant chosen for these experiments was sodium dodecyl sulfate (SDS), a soluble surfactant. SDS was chosen due to its easy accessibility as well as its large range in surface tension versus concentration. In a review article, Chang & Franses (1995) show

that SDS has a range from 72 mN/m (that of pure water) at very low concentrations down to approximately 40 mN/m at a 10 mM equilibrium concentration.

The surfactant SDS, which comes in solid form, was added to the free surface to allow the growth of the monolayer. Before each run, the monolayer present in the tunnel due to naturally occurring surfactants was removed via a vacuum device which "sucks" the surface clean. Next the surfactant was added, and if too much was present the vacuum was used to remove part of the monolayer to control the placement of the Reynolds ridge within the test section. The velocity in the test section was adjusted for various cases ranging from 8 cm/s to 18 cm/s depending on the experiment. Note that a change in the velocity also affected the placement of the ridge. Based on (2.18) with a free stream flow of 9 cm/s for the case presented in the results the Re was approximately 1200.

3.1.3 The Surface-Piercing Cylinder

A small brass rod of diameter 3.175 mm was used as a cylinder to create the desired flow field. This resulted in a range of Reynolds numbers of 350 to 460 for a free-stream flow of 11 cm/s to 15 cm/s. The resulting Froude number range was from 0.62 to 0.85, thus remaining below the critical value of 1.0. The Weber number ranged from 0.53 to 1.43 which indicated the near equality of surface tension forces to inertial effects. The cylinder was attached above the free surface to a small manually controlled traverse which allowed for some ease of maneuverability of the cylinder within the test section.

3.2 DPIV System

The Digital Particle Image Velocimetry (DPIV) system used was one similar to that presented by Willert & Gharib (1991), so great detail will not be described as to the processing technique. The basis of the method is that two images of the flow, which have been seeded with particles illuminated by a light source, are captured with a known time

difference between where the particle positions are correlated to generate a velocity field. The flow was seeded using 14 μm glass coated spheres constructed to be approximately neutrally buoyant in water. For the close-up view of the Reynolds ridge, to obtain the required seeding density the particles were injected just ahead of the last screen and upstream of the contraction section so that no disturbance of the flow in the test section resulted.

A plane within the flow was illuminated using a Lexel Model 95 argon-ion laser with a power capability of 3 to 4 Watts. As shown in Figure 3.1, a laser sheet is generated with the use of a cylindrical lens, while other mirrors are used to direct the sheet into the test section depending on the plane of flow that was studied. In the case of the close-up view of the Reynolds ridge, a 105 mm lens attached to a bellows was used on the camera to image a 5 mm X 3 mm area of the flow. The plane studied was one parallel to the flow yet perpendicular to the free surface to image the two-dimensional flow field of the Reynolds ridge (see Figure 1.3). In later cases this is referred to as a center cross-section.

In the case of the cylinder wake, a downstream view of the flow was acquired (using the downstream optical access window to image this plane) where the sheet was thickened using another quite large focal length cylindrical lens. The thickening of the sheet, from about 2 mm to 6 mm, allowed for the particles to remain illuminated during the exposure time of an image pair. Due to the large distance between the camera and plane imaged, a 180 mm lens attached to an adjustable bellows was used. The other two planes imaged were surface-parallel cross-sections, as well as a center cross-section parallel to the flow (see Figure 3.2). The surface-parallel cross-section was imaged through the use of a mirror placed below the test section at which the camera was directed, and thus the light imaged by the camera was not distorted by passing through the free surface. For this case, a 135 mm lens with a 12 mm extension ring was used for imaging the flow.

The laser beam was shuttered using a Conoptics Model 303 optical shutter. The shutter was controlled by a General Pixels VTG-100 timing box where the camera signal

was used as an input to the box which generated a timing signal according to the programmed exposure and delay times. Typical exposure and delay times were on the order of milliseconds depending on the area imaged and speed of the flow.

The flow was imaged using a Pulnix CCD camera with a CCD size of 768 X 480 pixels. The camera was run in continuos mode such that the first image of a pair was taken at the end of the 1/30th of a second exposure when the laser sheet was unshuttered, and the second image at the start of the next 1/30th of a second exposure depending on the delay time. This results in a sampling of the velocity field of the flow every 1/15th of a second. Initially the images were captured onto laser disc and later digitized to a binary format for processing. The DPIV program was typically run using a 32 X 32 pixel size processing window and a step size of either 8 or 16 pixels. This resulted in a resolution of approximately 200 μm for the close-up view of the Reynolds ridge, and approximately 1 mm resolution for all other views studied. The program produced both velocity and vorticity data. In the cases where averaged data was needed, 500 or more velocity files were averaged together to obtain values of the average velocity and vorticity as well as the Reynolds stresses.

3.3 Shadowgraph and Lenslet Array Technique

The light source utilized for generating the beam of collimated light was a Cuda Products Corporation Model 1-150a single port fiber optic illuminator with 150 Watt capability. The fiber optic cable end was placed behind a pinhole to create a point source of light. This source was shown onto a 29" focal length mirror which created an approximate 3" diameter beam of collimated light. A flat free surface mirror was then used to reflect the beam upwards through the bottom of the test section as shown in Figure 3.1 to pass through the free surface.

For the shadowgraph imaging, a shuttered Pulnix CCD camera, with a 50 mm lens and 12 mm extension ring, was used to image a polished glass screen placed above the free surface onto which the collimated light shown after passing through the test section. Again, initially the images were captured onto laser disc after which a sequence could either be transferred to video, or single frame images could be digitized. The area imaged was approximately 3 cm X 2 cm capturing the whole width of the cylinder wake. This technique visualizes the free surface by using the fact that the light rays will be deflected according to the free-surface slope. Thus a concave surface, or depression, will appear as a dark region while a convex surface will tend to focus the light and result in a brighter or whiter region in the image. Note then that the Reynolds ridge appears as a bright white line in the greyscale images due to its convex surface deformation.

The new lenslet imaging technique (Roesgen et al., 1997) uses the same beam of collimated light as generated for the shadowgraph setup, however a lenticular array was placed just above the free surface through which the light passed as shown in Figure 3.3. The lenslet technique is similar to shadowgraph in that it relies on the same principle -- the bending of the light rays as they pass through a deformed free surface. However, this technique provides a quantitative measurement of the light displacement which then allows for a calculation of the free surface slope. The resulting equation for the slope measurement is (Roesgen et al., 1997)

$$\alpha = \left(\frac{n_A}{n_F - n_A} \right) \phi \tag{3.1}$$

where Snell's law was used and α is the slope measured from the reference slope of zero, ϕ is the local angle of incidence of the refracted light, and n_A and n_F are the refractive indices of the air and fluid respectively. The linear relation between ϕ and Δx, the displacement of the focal point in pixels, is generally governed by the equation $\Delta x = F\phi$ where F is the focal

length of the lenslets. However, experimentally it is hard to say that the measurement is taking place exactly at the focal plane, and in some cases the camera was purposely focused away from the focal plane to increase sensitivity of the measurement (Roesgen et al., 1997). As a result, the linear relation between the displacement and ϕ is found through a calibration measurement. Thus with a displacement measurement of each focal point imaged by the camera in the focal plane, a measurement of the free surface slope at each focal point is obtained. The advantage to this technique is that it provides a planar measurement or mapping of the free surface at one instant of time, unlike previous measurements of the Reynolds ridge.

The glass lenticular array used has a local focal length of 12 mm, is hexagonal in spacing, and has a distance of 0.2 mm between each lenslet center (or diameter D of 0.2 mm for each lenslet). This results in a F-number, or F/D, equal to 60, which is quite large but necessary for the technique to work successfully (Roesgen et al., 1997). A Pulnix CCD camera with a 50 mm lens and 12 mm extension ring was used to image the focal plane of the lenticular array which resulted in an image of the focal points (a sample image is shown in Figure 3.4). These images were again first captured onto laser disc, later digitized, and then analyzed through a data processing scheme (Roesgen et al., 1997) similar to DPIV in that it is basically an image correlation of the focal points to measure each one's displacement. The displacement vector was broken down into a x-slope component and y-slope component for each focal point as the choice of vector representation of the data. A calibration during each experiment was performed to obtain the corresponding relationship between the slope and displacement in pixels of the focal points. To achieve this a 2 degree glass wedge was used to generate a known slope displacement of a single focal point, where a pinhole mask was used in front of the array to isolate a single focal point. The displacement of the focal point where the wedge was in and out of the optical path of light passing through the particular focal point allowed for a

calibration measurement and a linear relationship between the slope and displacement is found using (3.1).

The sensitivity of the technique can be calculated using some of the calibration data. In a case where the focal plane was slightly out of focus, a displacement measurement using the 2 degree wedge was found to be $8.5X10^{-4}$ radians/pixel. The scale factor for the image was calculated to be $2.2X10^{-2}$ mm/pixel. The effective focal length then of the lenslet array (or calibration factor) was then 25.9 mm (/radian). Typically with digital correlation techniques a sensitivity displacement of 0.1 pixel is achieved. In addition to using (3.1), one finds that the sensitivity of the technique is calculated to be for this case as $2.6X10^{-4}$ radians (Roesgen et al., 1997).

In studying the Reynolds ridge, due to it's two-dimensional nature over the measurement area the x-slope measurement was averaged over the y-axis which results in the free surface slope and height profiles shown in the results. This lenslet technique was also applied in the case of the cylinder wake to map the free surface height within the wake simultaneously with the DPIV measurement. The surface height was calculated from the slope measurements using a least-squares two-dimensional integration technique using both the x and y slope components at each point (Roesgen et al., 1997).

3.4 Surface Tension Measurement Technique

The above lenslet technique was utilized as a surface slope measurement to ultimately measure a two-dimensional surface tension gradient such as that associated with a Reynolds ridge due to its two-dimensional flow field. The surface tension measurement relies upon the fact that water molecules are charged, and thus when a strong electric field is applied in the near region of the free surface a surface deformation will result proportional to the strength of the electric field. However, the surface properties itself, i.e. the local surface tension, will determine the amplitude of the deformation -- if the surface tension is low then the deformation will be large as there is less elastic resistance of the

surface to be deformed and vice versa. Thus a known electric field is applied to the free surface and the slope of the deformation is measured from which an amplitude is extracted and a surface tension gradient in two dimensions is measured.

The electric field is applied through the use of a glass slide (to allow optical access to the surface for the lenslet measurement) 10 cm by 5 cm in dimension which is coated with an electric film in a striped manner (strips aligned parallel to long width of the slide) and placed in the test section such that the stripes are aligned with the flow. The electric strips have a pitch of 1.5 mm where the pattern (not to scale) is shown in Figure 3.5, and thus at a given time the strips have alternating signs of voltage in that there are two separate circuits. The resulting deformation over the surface is a two dimensional sinusoidal pattern as shown in Figure 3.6 where in this case the ridge is present. Thus across the ridge in the x-direction the amplitude of the sinusoidal pattern changes, with respect to the value of the surface tension in that near vicinity, which is measured using the lenslet technique.

To apply a strong enough electric field, two Kepco bipolar operational power supply/amplifiers are used providing up to 500 volts (low current) where each is separately wired to an electro-coated pattern on the slide. A function generator is used to provide a 1 KHz square wave (10 V amplitude) signal to the first amplifier. The second amplifier is wired to the first to run in synchronous mode yet provide voltage of opposite sign to that of the first one. Initially the technique was tested where each amplifier provided a constant positive/negative corresponding voltage, however it was found that the free-surface deformation of the described sinusoidal shape was more stable when the voltage was oscillated at a high frequency.

First the reference pattern of the lenslet focal points is acquired where the voltage is off and the surface is flat. Next, the voltage is turned on where the ridge is downstream of the test area (thus a clean surface present and surface tension constant) and another set of reference images is acquired. These will tell of any tilt which the slide may have with respect to the free surface plane, i.e. a linear variation in amplitude would result due to its

proportionality to the distance between the electrode strips on the slide and the free surface. Next, a sequence of images is acquired where the ridge is in the test area. As before, the measurement is decomposed into a x-slope measurement (which measures the slope across the ridge) and a y-slope measurement (which measures the amplitude of the sinusoidal deformation) and using a computer program the reference measurements are applied to the data and a two-dimensionally averaged (in the y-direction) relative surface tension gradient across the ridge is measured. Note that the technique will be described in greater detail in a forthcoming paper.

Chapter 4

Results and Discussion

4.1 The Reynolds Ridge

First of all, the velocity and vector field for one set of images in an experimental run is shown in Figure 4.1 where the free stream flow (U) is approximately 9 cm/s. This is the first experimental observation of the boundary layer that forms beneath a Reynolds ridge. From the velocity data the free surface velocity, u_s, was extracted for 8 velocity files taken during the same run where each data file was referenced to the x-location peak value of deceleration due to the fluctuating position of the ridge between image pairs. This data is shown in Figure 4.2 and the simultaneous free surface height measurement using the lenslet technique is shown in Figure 4.3. Note that the deceleration in the surface velocity occurs in the region of the peak height in surface deformation. This sharp deceleration at the free surface is due to the fact that the flow is meeting head on the compressed monolayer which is almost stationary (note that the velocity at the surface does not go to zero but rather reaches a small magnitude of about 2 cm/s and starts to gradually decrease). From the u_s values the deceleration term in (2.17) can be calculated and the results are shown in Figure 4.4. Note that the large fluctuations ahead of the peak vorticity flux value are due to the small fluctuations in a large magnitude of velocity which is present before the deceleration occurs.

Also using the velocity data, the displacement thickens of the boundary layer can be measured where the traditional definition is used as

$$\delta = \int_0^\infty \left(1 - \frac{u}{U}\right) dx \tag{4.1}$$

This data is plotted in Figure 4.5 along with the theoretical flat plate profile where

$$\delta = 1.7208\left(\frac{\nu x}{U}\right)^{1/2} \tag{4.2}$$

It is observed that the displacement thickness magnitude is the same for the theoretical flat plate with the exception that near the leading edge the theory of course breaks down and the data instead shows a dramatic jump in the small region of deceleration. The surface shear stress is also extracted from the velocity data and is plotted in Figure 4.6 along with the theoretical flat plate profile where

$$\tau = 0.4696\mu\left(\frac{U^3}{2\nu x}\right)^{1/2} \tag{4.3}$$

Here beyond the origin at x=0.22 cm good agreement between the two is seen, and the trend of an initial peak in shear stress which then decreases is observed as expected. However, the data shows more of a trend of approaching zero at a faster rate. Also, three boundary layer profiles for the case shown in Figure 4.1 are shown in Figure 4.7. Here a slight steepening in the slope of the profile near the surface is observed as expected with the decreasing shear stress.

In addition another run where the ridge was located ahead of the test area is shown in Figure 4.8, the simultaneous height measurement in Figure 4.9, and the corresponding boundary layer profiles in Figure 4.10. Thus it is observed that farther downstream of the ridge, the profiles show a steepening which of course reflects the fact that the shear stress is decreasing as well at the free surface. This fact is also evident in the vorticity plot of Figure 4.8 in that the maximum vorticity (or sharpest slope in the boundary layer profile due to the small magnitude of the v component of the velocity field) is moving down and away from the free surface. Because the shear stress boundary condition at the surface is wholly dependent on the properties of the film as shown in (2.5), this free-surface

boundary layer shows the characteristics of a flat plate boundary layer in the presence of a pressure gradient.

Figure 4.11 shows the measured shear stress values for three cases where the ridge is slightly upstream (height profile corresponding to Figure 4.9). Here it is observed that further downstream the shear stress is decreasing, and in some cases measured to be zero. According to theory, the shear stress measurements shown in Figures 4.6 and 4.11 must be balanced by the surface tension gradient and viscous effects of the film. Using the new surface tension measurement technique data was acquired simultaneously with DPIV, and averaged over almost 1000 measurements. The corresponding height profile and relative surface tension measurements in the vicinity of the ridge are shown in Figure 4.12. These results show a drop in surface tension over the whole length of the ridge, rather than just in the vicinity of the peak where the deceleration was observed. Also, a slight rise in surface tension is observed after the inflection point in the height profile. Recall that this is the region where the boundary layer profiles approach a zero shear stress, and perhaps the flow does separate slightly at the surface but not to a large enough sense to be measured -- although some zero values of shear stress were recorded in Figure 4.11. Given that the initial curvature of the ridge does provide a curved boundary which the flow must follow, however this curvature is small in comparison to the effect that is observed. Rather, it is the fact that the shear stress must approach zero and then turn positive at the free surface which enforces this condition and pushes the maximum strain field deeper into the flow.

4.2 The Surface-Piercing Cylinder

4.2.1 Shadowgraph Visualization

Initially, shadowgraph visualization was performed to acquire a basic impression of the flow field for the various cases where the ridge is in the near wake of the cylinder, upstream of the cylinder or contaminated case, and far downstream of the cylinder or the

clean case. It was found that qualitatively for varying speeds the resulting flow was similar except for increased surface deformation at higher velocities.

For the flow field where the surface is clean, Figure 4.13 shows three different Reynolds number cases varying from 350 to 560 where the free-stream flow is moving from left to right. Qualitatively they are similar in that the vortex tubes shed from the cylinder are easily visible as dark circular regions in the images due to the convex surface deformation created by the vorticity in the flow. Next, the flow field where the ridge is far upstream of the cylinder, or where the wake is completely contaminated, is observed in Figure 4.14. Note a the dramatic change in the flow field has occurred in that the deformation of the free surface has been greatly reduced if not become negligible. Finally, the case where the ridge is in the wake of the cylinder is presented in Figures 4.15 and 4.16. The first figure shows the case where the ridge is "unattached" to the cylinder and one observes a transformation in the surface curvature behind the Reynolds ridge. Here as the vortex tubes are shed from the cylinder and interact with the ridge a large disruption of the flow field is obvious and what appears to be a stretching of these filaments seems to be observed. Figure 4.16 show three Re cases where the ridge has "attached" itself to the cylinder similar to the behavior observed in shock waves. Note that for the higher Re cases the stable attachment length behind the cylinder appears to be larger.

Figure 4.17 shows one particular Reynolds number case of 460 where the ridge is located at different positions with respect to the cylinder, and this attachment process of the ridge to the cylinder is observed. Next, Figure 4.18 shows a sequence of images where the cylinder has been moved 2 cm upstream and thus the flow field farther down in the wake is observed. It is interesting to study the effect on the surface curvature, and thus surface vorticity, as a vortex filament convecting with the flow interacts with the Reynolds ridge.

Finally, a case was observed (Figure 4.19) where the ridge was located downstream of the cylinder yet the surface deformation shown in Figure 4.13 was not

observed. What occurred in this case, as will be discussed further in the results to be presented, is that the cylinder itself was coated with surfactant and acted as a contaminant source shedding surfactant into the wake. This led to a much lower level of surface deformation similar to that observed in Figure 4.14. It should be noted also for this case that the attachment process was not observed. Overall, the shadowgraph results show that a large variation of the flow field is observed due to the presence of surfactants and thus an alteration in the alignment of vorticity in the wake from that of the clean case.

4.2.2 Surface-Parallel Cross-Section Velocity Data

For this spatial cut of the flow field three different velocity cases were investigated, however actual DPIV data will only be presented for one case where Re=350. The other higher velocity data were all qualitatively similar to the case presented. First of all, for the clean case a sequence of vector/vorticity plots are shown in Figure 4.20. The results are as one would have predicted from the shadowgraph data where the Karman vortex street is observed in the cylinder wake. Next, Figure 4.21 shows a sequence where the ridge is upstream of the cylinder. Note how in this case the flow seems to display the characteristics of a much lower Re wake and the low velocities and vorticity levels are characteristic of the weak surface deformation observed in the shadowgraph cases. Finally, Figure 4.22 displays the free-surface cross-section where the ridge is in the near wake of the cylinder. One can see the drop in velocity as the flow meets the ridge, and the stretching of the vorticity field as the filaments pass through the ridge. The drop in circulation of the vortex filaments at the free surface was measured as compared to the clean case as the filaments cross the ridge. The normalized data is presented in Figure 4.23 and shows a loss of circulation in the z-direction in excess of 80% as the filaments pass through the ridge, while that observed due to dissipation in the clean case is minimal.

Data was acquired simultaneously with the lenslet technique for the case where the ridge is in the transition process of attachment to the cylinder. These results, shown in

Figure 4.24, indicate that the shape of the ridge when attached to the cylinder follows the outer edge of the vortex filaments as they are forming on the cylinder, forming what looks similar in compressible flow the shape of a bow shock. This would explain that at higher Re this circulating region around the cylinder is much larger, because of the greater magnitude of vorticity in the wake, leading to a larger "bow shock" and thus a longer attachment length. These results intuitively make sense as the Reynolds ridge shape is highly dependent on the momentum of the flow in it's near vicinity. This fact is also observed in the shadowgraph data where the ridge is in the near wake of the cylinder where the shape resembles the wake velocity profile, and also as well in any general observance of the ridge when in the tunnel as it is curved when approaching the walls of the test-section due to the momentum deficit found in the boundary layer which forms on the side walls.

For the case where the ridge was upstream of the cylinder, two additional cuts at 0.55 cm (about 1.7 cylinder diameters) and 1.10 cm (about 3.5 cylinder diameters) below the free surface were studied. Velocity and vorticity field sequences for these two cases are shown in Figures 4.25 and 4.26. These results show that farther down into the flow, the increasing similarity the wake has to that of the clean surface case. The middle cut at 0.55 cm portrays a stretching of the vortex filaments even while still attached to the cylinder. Data for the clean case of these cuts was taken but the same flow field of that presented at the free surface was only observed, verifying the two-dimensional nature of the vortex filaments shed from the cylinder when the surface is clean.

Finally, an interesting case was observed and a sequence of velocity/vorticity plots is shown in Figure 4.27 where the laser sheet was at the free surface height and Re=410. This case was taken where the ridge was far downstream of the cylinder, yet after processing some of the preliminary data the clean wake was not being observed as was described above. What in fact happened was that the facility was left untouched overnight with the cylinder in the water, and when turning the tunnel on the next day surfactant had

collected onto the part of the cylinder left submerged. It was then noticed that when the cylinder was lowered deeper into the water, the clean wake previously discussed was observed. Thus, in the case presented in Figure 4.27 what is happening is that the cylinder is acting as a contaminant source with the shed surfactant causing high surface tension gradients within the wake. Notice that the surfactant seems to cause an area of slower surface velocity in the line of sight directly behind the cylinder. This results in regions that appear to be surface shear layers on the sides of the wake. The lower velocity and high surface tension gradients would account for the large decrease in surface deformation observed in the shadowgraph data of this case. Also, due to the high surface tension gradients within the wake the vorticity magnitude of the shedding filaments in the surface normal direction has been reduced which also leads to lower surface deformation.

4.2.3 Downstream Cross-Section Velocity Data

First, for the clean case six different downstream distance vorticity plots averaged from 500 velocity files for Re=410 are shown in Figure 4.28. Observable is a surface-parallel vorticity component existing in the vicinity of the free surface. The large vorticity contours far beneath the surface in the plots taken at X=1.0 and 2.0 may be due to the fact that when acquiring the images some of the laser light reflected off the cylinder producing a lighter background region and may have affected the image processing performed in the DPIV program. Note that in the plot farthest downstream (X=6.0 or almost 20 cylinder diameters downstream) these signs of vorticity result in a net upwelling of fluid into the center of the wake similar to that found in ship wakes shown in Figure 1.2. The question is whether or not this is in fact one vortex pair that is moving side to side within the wake, or two vortex pairs sitting stably within the wake. It is also interesting to note that the size of these structures is on the same order as the diameter of the cylinder. Figure 4.29 exhibits two vorticity plots, averaged from only 10 velocity files each, by skipping every other file. Note the high turbulence level of the flow field even over 10 averaged images.

If one looks at the sequence shown for the surface-parallel cross-section, from the DPIV acquisition capability the flow is sampled every 1/15th of a second, and note that at any certain position downstream at approximately each time difference one sees one vortex filament pass through. Thus, at every other sampling (every 1/7.5 seconds) a same sign vortex filament will pass through a downstream position. As a result one can see that in fact the vorticity contours in Figure 4.28 actually represent only one vortex pair that is placed on the inside edge of a vortex filament weaving between the filaments creating a side-to-side motion within the test area, and thus averaged appear at a certain downstream distance as two vortex pairs. Farther downstream it appears as only one vortex pair with the centers far apart, as what appears to be the inside vortex pair further upstream actually overlap and average to zero vorticity because the vortex pair is spreading apart at a faster rate than the growth of the wake. The same features are present in the lower Re=350 case with correspondingly lower values for the vorticity.

Next, the case where the ridge is downstream of the cylinder (unattached) but ahead of the laser sheet is presented. Figure 4.30 shows the vorticity plots for the clean case and the ridge case for Re=350, laser sheet 4 cm downstream of the cylinder and ridge approximately 2 cm downstream of the cylinder. Here a larger component of vorticity is observed by the increase in strength of the vorticity of the two center vortex structures. This corresponds to a turning of the vortex filaments such that a realignment is taking place and surface-parallel vorticity has been converted from the original surface-normal component of the vortex filaments. However, the outside vortex structures associated with the clean case are still present indicating that total conversion has not taken place. However, Figure 4.31 shows the same conditions except at a higher Re=410, and now a total conversion of the vorticity has taken place and a much larger strength vortex pair is observed and no evidence of the vorticity generated in the clean case is seen. Note that at higher Re, larger gradients in surface tension and velocity are present at the ridge.

Before presenting further results, the issue of the secondary flow that is apparent in the surface film due to the boundary layer on the side walls of the tunnel should be addressed. The vorticity layer that is present near the free surface when the ridge is upstream of the laser sheet is due to a circulating flow that is generated in the film behind the ridge and before the growth of the film is too large such that shearing motion in the film is retarded by the film's rigidity or high shear viscosity (in the cases presented this condition was not reached far downstream but was observed at times when the tunnel was first turned on before the film was vacuumed off). This flow, observed by both Scott (1982) and Kenning & Cooper (1966), is comprised of two recirculating regions shown in the schematic of Figure 4.32. The lower momentum of the flow beneath the film near the walls allows for a velocity in the film up the sides of the tunnel, near the ridge crosses over to the center of the tunnel, and on the centerline of the tunnel a downstream velocity is present. Figure 4.33 shows vorticity field in the tunnel, when the camera is positioned on the centerline and the ridge is 2 cm ahead of the laser sheet, and manifests the surface-parallel vorticity that is present from this secondary flow in the film. Thus depending on the positioning of the camera with respect to the centerline, different values of the vorticity layer at the free surface are observed. However Figure 4.34 shows just one example where two cases have the same flow conditions but different cylinder placement with respect to the centerline, and this secondary flow does not affect the features generated due to the free-surface boundary condition but rather acts more like a "background" vorticity that is pasted onto the flow field.

Next, the case where the cylinder was contaminated is discussed where the Re=350, laser sheet 4 cm behind cylinder and in case with the ridge the ridge is located 2 cm behind the cylinder in the near wake. First, the case where the ridge is downstream of the laser sheet, Figure 4.35a shows that due to the surface tension gradients caused by the spreading contamination off the cylinder, a larger conversion of the vortex filaments to the surface-parallel component is observed. These filaments in fact interact with the free

surface compressing the surfactants into the middle of the wake and form two small opposite sign structures due to the shear generated from the surface tension gradients similar to that observed by Hirsa et al. (1995). However plot(b) shows the case where the ridge is ahead of the laser sheet and again the turning of the filaments is observed, but the small structures near the surface are of the opposite sign as those in plot(a). One possible cause for vorticity of this sign to be generated is that the curvature of the ridge upstream due to the wake of the cylinder is of the sign to produce surface normal vorticity of the same sign as the vortex filaments and in the strain field of the boundary layer is turned to the surface-parallel direction. The reason why these structures are not seen in the case where the surface was not contaminated by the cylinder is that in that case the filaments are not turned until they cross the ridge and thus are much closer to the surface and not as far apart, i.e. any vorticity generated from the curvature of the ridge would just add on to the filament vorticity. While in this case, the filaments are turned initially due to the large surface tension gradients behind the cylinder and thus propagate downstream and tend to lower slightly and spread apart due to their induced velocities on eachother -- as is observed by comparing the centers of the vortex pairs for these two cases.

Finally, the case considered is that where the ridge is located approximately 7 cm upstream of the cylinder. The laser sheet was located at two different downstream distances from the cylinder of 1.75 cm (about 5.5 diameters) and 3.75 cm (about 12 diameters). Figure 4.36 shows the vorticity contours from 500 averaged velocity files at Re=410. The data taken close to the cylinder shows the counter-rotating vortex pair observed in the previous case, however at a larger distance away from the free surface. Note that the size of these vortex tubes is on the same order as the diameter of the cylinder. Basically the boundary layer from the ridge has pushed this pair down into the flow. Farther downstream one sees that this pair has moved slightly deeper into the flow field as well as spreading apart slightly. The loss in circulation farther downstream is due mostly to the fact that the filaments are not turned as dramatically and most of the vorticity is not

parallel to the free surface as was in the case farther upstream. The smaller vortex pair of the opposite sign present near the free surface in the upstream case is due to the lower large vortex pair interacting with the contaminated surface shedding off opposite sign vorticity. The vorticity is generated as the vortex pair below compresses the surface directly above leading to surface tension gradients which impose a shear stress on the fluid resulting in a vorticity flux at the free surface.

4.2.4 Center Cross-Section Velocity Data

The velocity results for this cross-section are shown in Figure 4.37 where Re=350. The cylinder edge is located at x=0 and the ridge for the contaminated case was located approximately 7 cm upstream of the cylinder. The vector field reveals that in the clean case the higher momentum fluid is located in the vicinity of the free surface, while in the contaminated case due to the presence of the boundary layer there exists a definite downwelling of the higher velocity fluid behind the cylinder. The vorticity plots, shown in Figure 4.38 show the high concentration of positive vorticity created from the boundary layer just behind the cylinder, while farther downstream in the clean case no surface parallel vorticity in the y-direction is found to exist. Also, a weak negative value shear layer is observed below the boundary layer. This corresponds to the fact that the shedding filaments cannot terminate within the fluid yet must also detach from the observed surface-parallel vortex filament seen in the downstream cross-section. As a result in this shear layer region the shedding filaments will pair and connect to eachother similar to the case of the that for a solid wall. The vorticity near the free surface present in the clean case can be attributed to the higher surface curvature in the near vicinity of the cylinder which also causes the slight downwelling. The zigzag vortex pair near the free surface observed in the downstream views is not present here as it has no set position but is convecting downstream with the flow as it is formed and thus averages out.

Data was acquired for the case where the ridge was located in the wake of the cylinder, but looked quite similar to the contaminated case presented in that the boundary layer causes a downwelling of the fluid. In addition, this data was not quite as clean because of the fluctuating position of the ridge (especially at lower velocities) it could move sometimes up to a centimeter while the data was being acquired. Overall it is observed that the results from this cross-section only seem to show the effects of the boundary layer and it's resulting strain field on the flow rather than the effects which can be attributed only to surface contamination.

4.2.5 Reynolds Stress Data

In the cross-sections where the data was averaged for 500 velocity files, Reynolds stress contours for this data was also calculated. First, for the downstream cross-sections the Reynolds stress computed was $-\overline{v'w'}$ using the coordinate system defined earlier. The Reynolds stress results for the case previously presented of Re=410 are shown in Figure 4.39 where the surface was contaminated and the ridge 7 cm upstream of the cylinder. The contours match up with the large vortex pair generated by the turning of the vortex filaments shed from the cylinder. The largest fluctuations in velocity, or Reynolds stress, is thus associated with these turned vortex filaments.

Next, the case where the ridge is in the wake of the cylinder is presented with Re=410 where a total conversion of the vorticity was observed, and Figure 4.40a shows that the largest Reynolds stress is indeed associated with the turned vortex filaments. However, for the same conditions but Re=350 where the vorticity was not completely converted plot (b) exhibits lower Reynolds stress values, though still associated with the vortical structures. The case of the contaminated cylinder, shown in Figure 4.40c, shows that again because the filaments have turned due to the large surface tension gradients in the wake, and the higher Reynolds stress values are associated with the vortex tubes. Note as

well the higher values of Reynolds stress for this flow field compared to those in plots (a) and (b).

For the clean case, three different downstream distances are shown to represent the Reynolds stresses in Figure 4.41. Close to the cylinder at 1 cm downstream, higher stresses are observed due to the violent nature of the flow as the vortices are shed. However, farther downstream there is some degree of Reynolds stress associated with the zigzag vortex structure (as also seen in the plot at X=1.0) but is dropping off quickly until at the farthest distance downstream of 6 cm the stresses have become minimal in magnitude and not really associated with the weak vortical zigzag structure observed in the vorticity plots.

The center cross-sectional data for the Reynolds stress ($-\overline{u'v'}$) is shown in Figure 4.42 for the clean and contaminated case discussed in the previous section. Note that for the free-stream velocity of 13 cm/s and the ridge 7 cm upstream for the contaminated case, this results in a Re value for the boundary layer on the order of 10^3. Thus the boundary layer is still well within the laminar range and as expected no significant Reynolds stress is present within the boundary layer. Rather in this case, the downwelling observed in the velocity profiles pushes the vortex filaments downward where there is significant Reynolds stress present. In the clean case, this higher value of the Reynolds stress is present closer to the free surface and in the vicinity of the breaking off of the vortex filaments in the shedding cycle and can be attributed to high fluctuations in the surface curvature in this region and the violent nature of the flow as it is shedding.

Chapter 5

Conclusions

5.1 The Reynolds Ridge

From the results, the magnitudes of the first and third terms on the right-hand side of (2.15) can be estimated. It is evident from the surface slope profiles across the ridge that the angle θ remains near 90 degrees such that the magnitude of the $g\cos\theta$ is small compared to the deceleration term. However, from the calculated results of the deceleration term it is observed that an order of magnitude of four is reached thus justifying the assumption that the curvature terms are negligible and that the primary source of vorticity flux in the case of the stationary Reynolds ridge is due to the surface deceleration as assumed in (2.17). Note as well the small region of approximately 0.5 mm over which occurs this deceleration of the flow as it meets the surface tension gradient of the film. From the results, it is observed that these two regions coincide as large surface tension gradients subsist within the film to which such a large shear stress at the surface can be attributed. However, the region over which the surface tension gradient takes place is much larger (approximately spanning 10 mm) some of which occurs before the deceleration of the flow is observed (although the steepest gradient is recorded in this region). It is interesting to note as well, that this region over which the deceleration is taking place is associated with the peak elevation in the surface height profile as one would expect from the simple Bernoulli assumption. However, after this a slight downward component is detected within the velocity field as the flow moves downward into the boundary layer and a relatively large drop in elevation is observed in the free surface profile. The vorticity flux at the free surface due to the deceleration is then convected downstream into the observed

boundary layer, and this slight amount of dissipation thus associated with the flow field results in a net loss of free surface elevation behind the Reynolds ridge. In other words, the deceleration has caused a net change in total head to occur and this is manifested downstream of the ridge as a slight loss in surface height.

The boundary layer profiles steepen in slope further downstream of the ridge. This steepening of the profiles can be attributed to the decrease in shear stress within the film due to the change in sign of the surface tension gradient near the inflection point of the height profile. This results in a lower, if not positive, shear stress at the free surface and thus a steeper slope of the boundary layer profile as it approaches the free surface. However, these profiles also resemble those of a flat plate boundary layer in the presence of a pressure gradient. Note that the curvature of the free surface, like that of a curved solid surface to which a flow must go around, thus also results in a slight pressure gradient at the surface moving downstream of the ridge -- this fact is particularly evident at the inflection point within the surface height profile for it is at this region of the flow where the peak vorticity in the boundary layer has moved deeper into the fluid resulting in a steepening of the boundary layer profiles close to the surface. It is interesting to note that when observing the flow far downstream of the ridge, the film itself may have an upstream velocity component. In this case, somewhere upstream of this region the flow must have separated from the free surface resulting in a reverse flow of the film at the surface. Thus the boundary layer profile in the near region of the free surface is highly dependent on the conditions of the film. This is because the resulting variations in surface tension gradients may drive the film to in fact reverse the flow field in some regions to maintain continuity of the film itself as a separate two-dimensional flow field.

Overall, the results from the experiments in which the Reynolds ridge has been studied exemplify the fact that for this flow field the surface tension gradient due to the presence of the monolayer is the boundary condition to which the fluid dynamically conforms by decelerating rapidly over a small region at the free surface. This results in a

large vorticity flux at the free surface and is convected and diffused downstream into the observed boundary layer.

5.2 The Surface-Piercing Cylinder

5.2.1 Clean Surface Model

First of all, for the clean case a model of the flow is presented in Figure 5.5. The model shows the Karman vortex street characteristic for this low Reynolds number flow field. However, the interaction of the strong vortex filaments, which must connect normally at the boundary, with the free surface create regions of high surface curvature as evident in the shadowgraph visualizations. This resulting surface curvature, where with each vortex filament as it is being shed creates a circular region of surface depression which in turn results in a region where upwelling must occur on the inside edges of these filaments. This region is most distinctly observed in the bright area surrounded by three vortex filaments seen in the clean shadowgraph visualization.

The sub-surface flow associated with an upwelling is that of a counter-rotating vortex pair which pushes the fluid upwards in the center of the pair. Also looking at the instantaneous shadowgraph, one can see the zigzag bright region associated with this vortex pair as it moves with the filaments. This vortex pair was visualized in the downstream view at various downstream cross-sections and also explained in Figure 5.2 as to how the observed vorticity field results. Basically, the inside position of the pair is dependent on the growth of the wake, or the placement of the inside edge of the vortex filaments, while the width between the pair is dependent on its interaction with the free surface, i.e. a vortex pair at a free surface of this sign will have the tendency to push apart. Thus the initial strong vorticity, associated with the large surface curvature, of the pair pushes the centers outward at a faster rate than the growth of the wake as the zigzag filament is convected downstream with the surface-normal filaments.

Thus the cylinder wake in the case of a clean surface shows the characteristics of large surface deformation due to the normally connecting shedding vortex filaments. This high curvature generates a vortex pair of the surface-parallel component which curves between the shedding filaments and convects downstream with the flow.

5.2.2 Contaminated Surface Model

For the case where the ridge is upstream of the cylinder, the resulting flow field is that of one similar to the solid surface case where the boundary layer generated from the ridge turns the filaments to the surface-parallel direction using the resulting strain field. The shedding filaments are not allowed to connect to the free surface as in the clean case due to the strong strain field within the boundary layer. Thus something similar to a horseshoe vortex is created as shown in the schematic (see Figure 5.3). Farther downstream a vortex pair of opposite sign is present due to the interaction of the larger lower pair with the contaminated free surface similar to that observed in other experiments. However, this vortex pair is weaker farther downstream as the horseshoe filament pair is also weaker. Also to meet the vorticity condition, similar to that of a solid boundary case, the vortex filaments will shed from the cylinder and pair and connect below the horseshoe filament. These connecting filaments in the average vorticity plot of Figure 4.38b create the observed negative vorticity shear layer below the positive vorticity boundary layer. One can also see evidence of the connection of the shedding vortices in this region in Figure 4.26 where the shedding filaments are moving close to eachother as they connect as shown in Figure 5.3.

5.2.3 Contaminated Cylinder Model

The fact that for this case a total turning of the vortex filaments is observed truly shows the effect surfactants can have on the free surface flow field. From the

shadowgraph for this case one can see that the surface deformation is significantly reduced in this case because the filaments are not connecting normally to the surface. However, because no ridge exists upstream of the cylinder there is no *uniform* strong boundary layer, or strain field, in the near region of the free surface to prevent the connection process by turning the vortex filaments to the surface-parallel component. Rather as was noted in the DPIV results, a region of slower fluid is generated in a thin wake behind the cylinder thus resulting in large velocity gradients and shear stresses which form to balance the surface tension gradients. This gradient is in the y-direction or across the wake. The resulting vorticity flux into the surface due to this shear stress is in the surface-parallel component in the x-direction, or the same component into which the filaments are redirected. It is thus these regions of high shear stress which help prevent the filaments from connecting totally normal to the free surface. As a result, the filaments get stretched to the surface-parallel direction by the decelerated flow field in the thin wake behind the cylinder similar to the contaminated surface case but without the interference of the boundary layer.

5.2.4 Flow Model of Ridge in Near Cylinder Wake

This last flow field is rather a combination of the first two as shown in Figure 5.4. The initial wake of the cylinder is that of the clean case where the filaments are connected normally due to the shear-free boundary condition at the surface. However, as the filaments are convected into the ridge, the vorticity is redirected to the surface-parallel component. Also as evidence from the results, this conversion is dependent upon the strength the of the ridge and thus the strength of the surface tension gradient. It was observed that for the lower speed case, and thus a lower deceleration occurring at the ridge and a lower vorticity flux into the surface-parallel component within the boundary layer, a total conversion of the vorticity was not observed. Rather some evidence of the vortex filaments still containing surface-normal vorticity is present, i.e. the contours associated

with the zigzag vortex pair present in the downstream cross-section data as well as the smaller value of vorticity in the turned filaments. However, for the higher speed case a total conversion was observed due to the higher strain field in the boundary layer and higher surface tension gradient as shown in Figure 5.5.

5.3 General Summary

Overall, the goal of the experiment was performed. Using new and existing experimental techniques, a particular aspect of free-surface flows was studied. The results show that the flow field in the vicinity of the free surface can be altered dramatically due to the production of vorticity from surface tension gradients associated with the presence of surfactants. It has been shown that the deceleration, due to the presence of shear stresses produce by the film at the free surface, is the primary term from which the vorticity flux is produced. Already, the damping effects of surfactants on free-surface deformation was a well known fact, however in this case it was shown that surfactants can alter the flow near the free surface by altering the free surface boundary condition. In that of a clean case, it is known that vortex filaments must connect normally at a shear-free surface and as was shown in the clean cylinder wake. However, it was also shown that the surface tension gradients can dramatically alter the connection process and provide a mechanism of vorticity conversion from one component to another depending on the "strength" of the gradient.

The relevance these results have to the aspect of the study of turbulence near a free surface is quite evident. By understanding these lower Reynolds number flow fields, one gains insight as to how higher Reynolds number or turbulent flow fields may in fact act as well. Turbulent structures, or essentially small eddies or vortex filaments, will thus behave differently depending on the free-surface boundary condition. The results presented show the tendency of large surface shear stresses, associated with surface tension gradients, to

redirect vortex filaments from the normal component to the surface-parallel component and to in fact generate vorticity in the surface-parallel direction.

In particular with respect to ship wakes, one can see the significance of this result. It is well known that surfactants abound at the ocean surface. And in fact, the passing of a large ship has the effect of, if anything, redistributing even more surfactants to the surface than were previously present (i.e. bubbles generated in the turbulent flow and breaking bow wave will collect surfactants from the sub-surface water and bring them to the surface). It is also known that in the far field ship wake a large counter-rotating vortex pair is found to persist which generates an upwelling in the middle of the wake pushing the surfactants to the side which form concentrated bands rendering the wake easily observable. Keeping in mind the far-field wake of a ship is also a highly turbulent flow field, the importance of understanding the distribution and dissipation of vorticity within the wake is clearly evident. Thus, if the presence of surfactants has the effect of redirecting the vorticity component near a free surface to the surface-parallel direction this may have the consequence of "feeding" vorticity into the large counter-rotating pair and in essence contributing to it's long persistence. One must also keep in mind the generation of vorticity from the Reynolds ridge itself, as shown in the boundary layer in Figure 1.2, will tend to separate a farther distance out from the wake and in fact form a structure of opposite sign which will push the fluid towards the wake on the far outer edge -- this can help account for the bands of concentrated surfactants and why these bands do not spread away from the wake. As a result, when looking at any flow field where a free surface is present, one must be aware of the fact that surfactants can play a significant role in its behavior -- particularly the distribution, generation, and dissipation of vorticity.

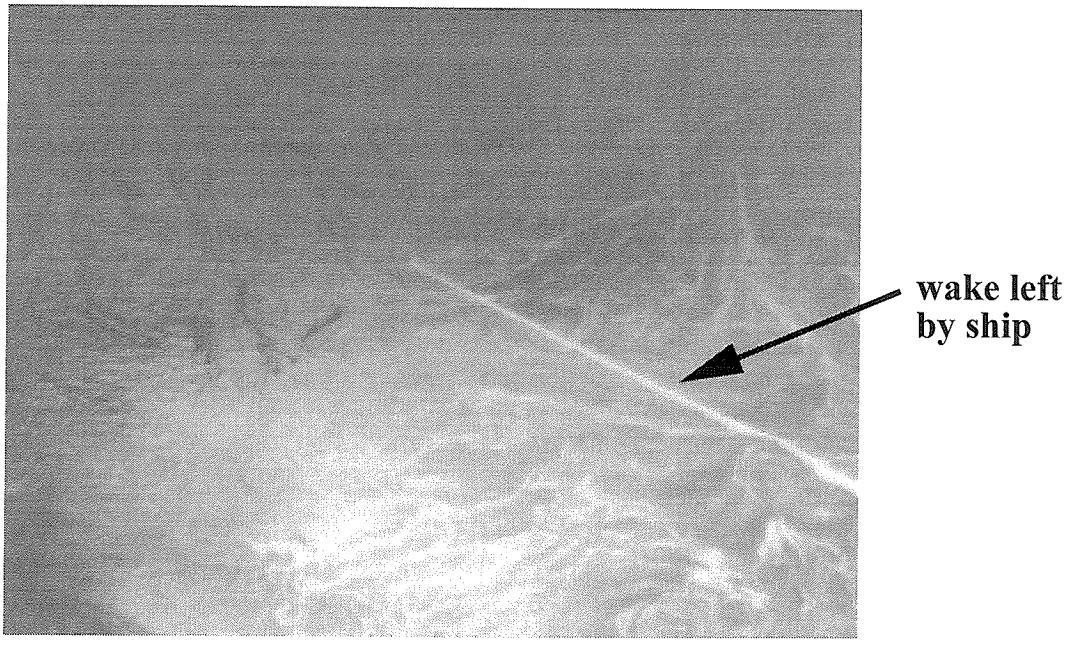

Figure 1.1: Image of a ship wake in the presence of an oil slick.

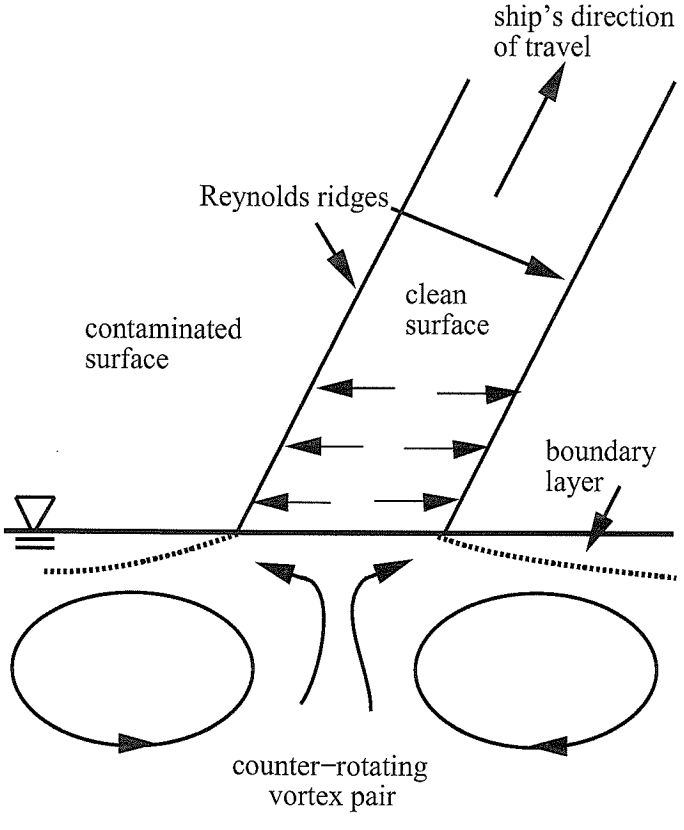

Figure 1.2: Schematic of flow field in the far wake of a ship.

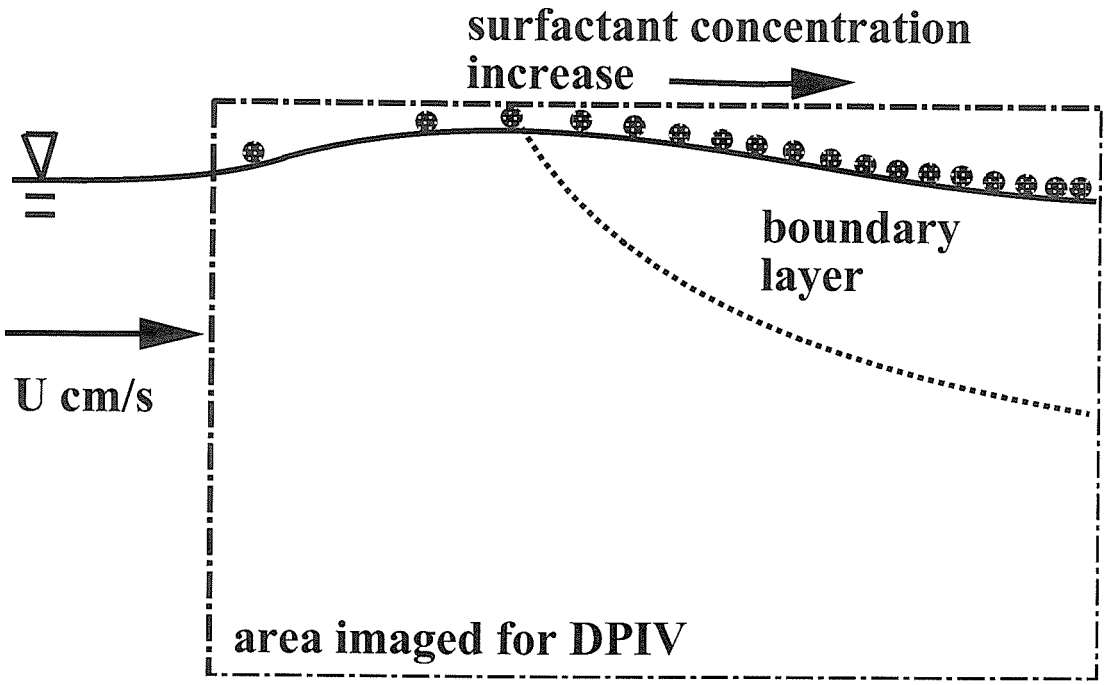

Figure 1.3: Schematic of flow field near a Reynolds ridge.

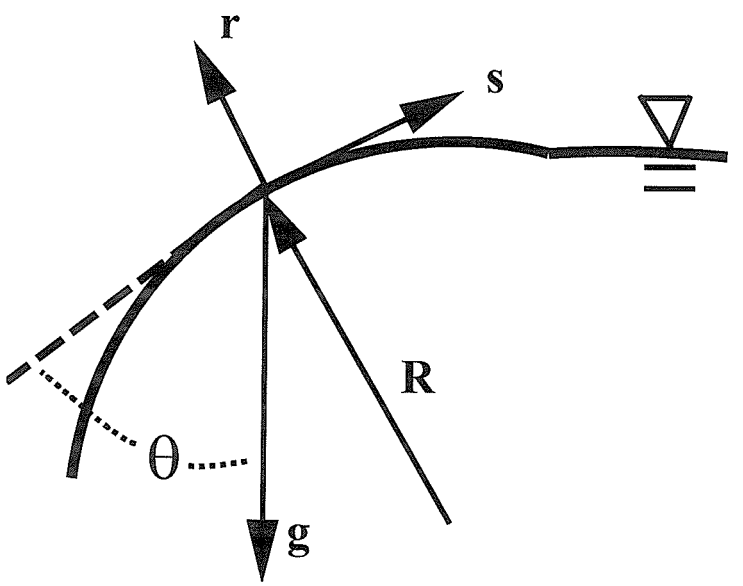

Figure 2.1: Local curvilinear coordinate system.

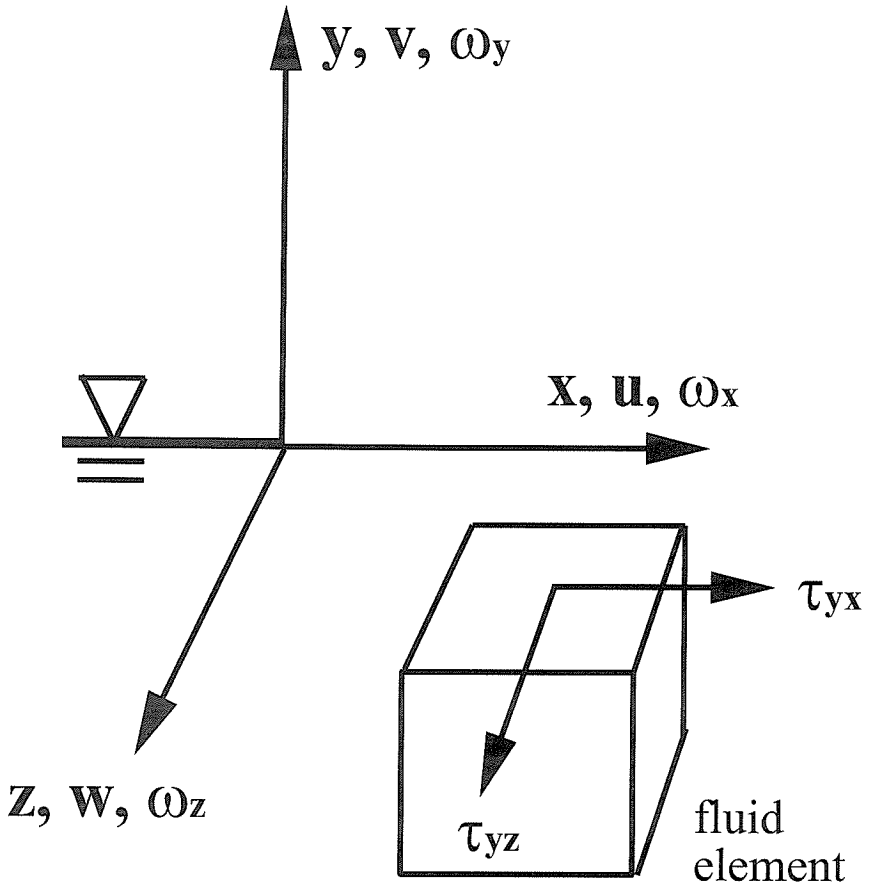

Figure 2.2: Global orthogonal coordinate system.

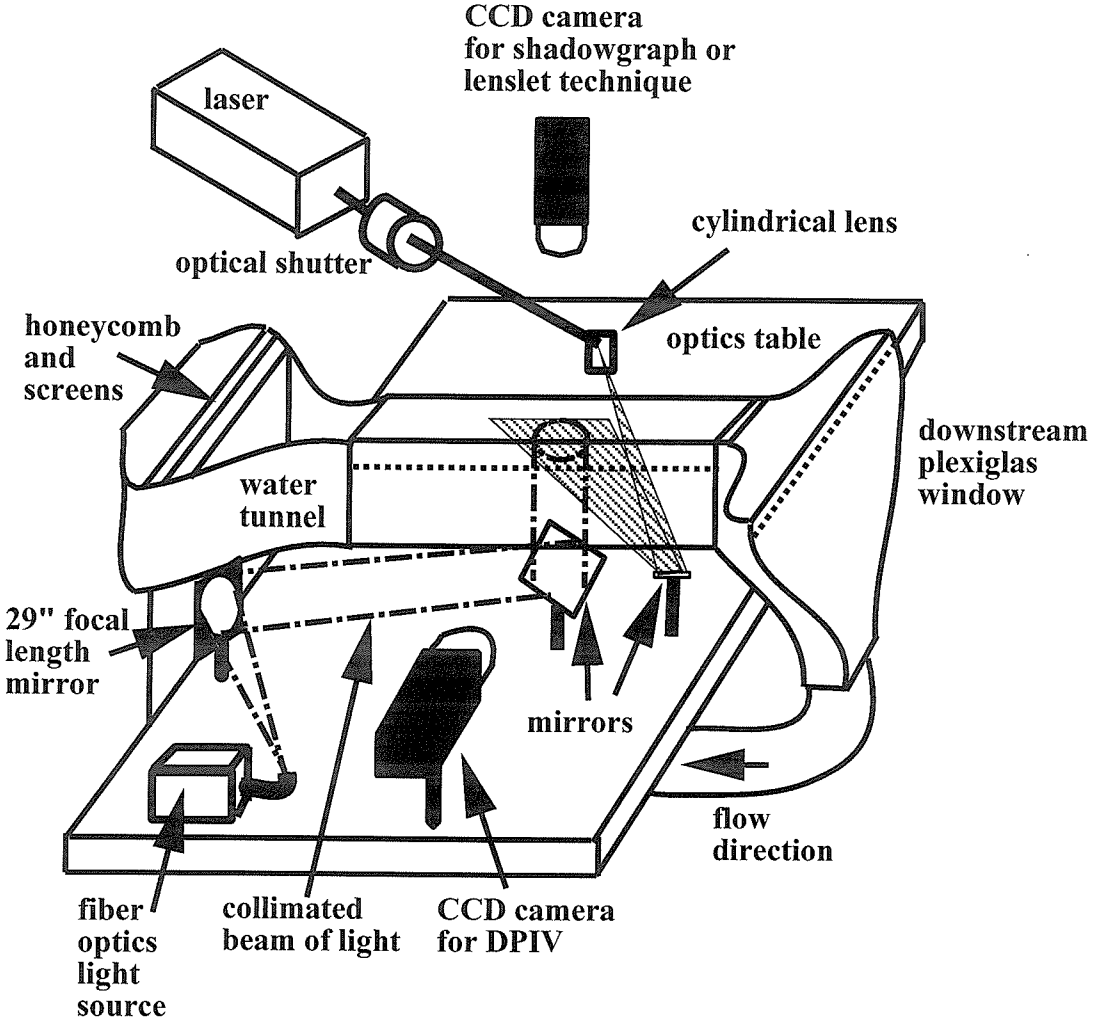

Figure 3.1: Experimental setup.

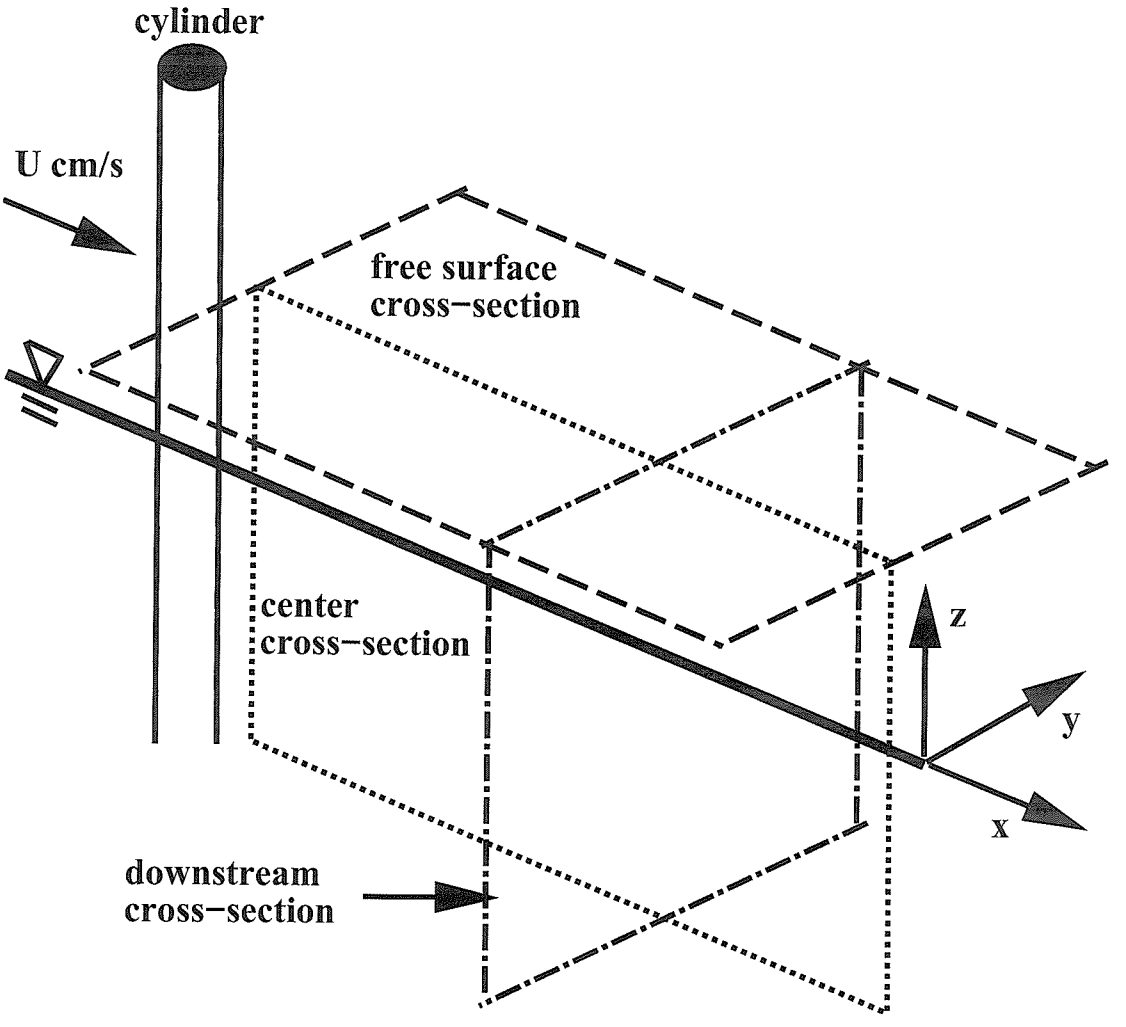

Figure 3.2: Schematic of cylinder flow field and the cross-sections studied.

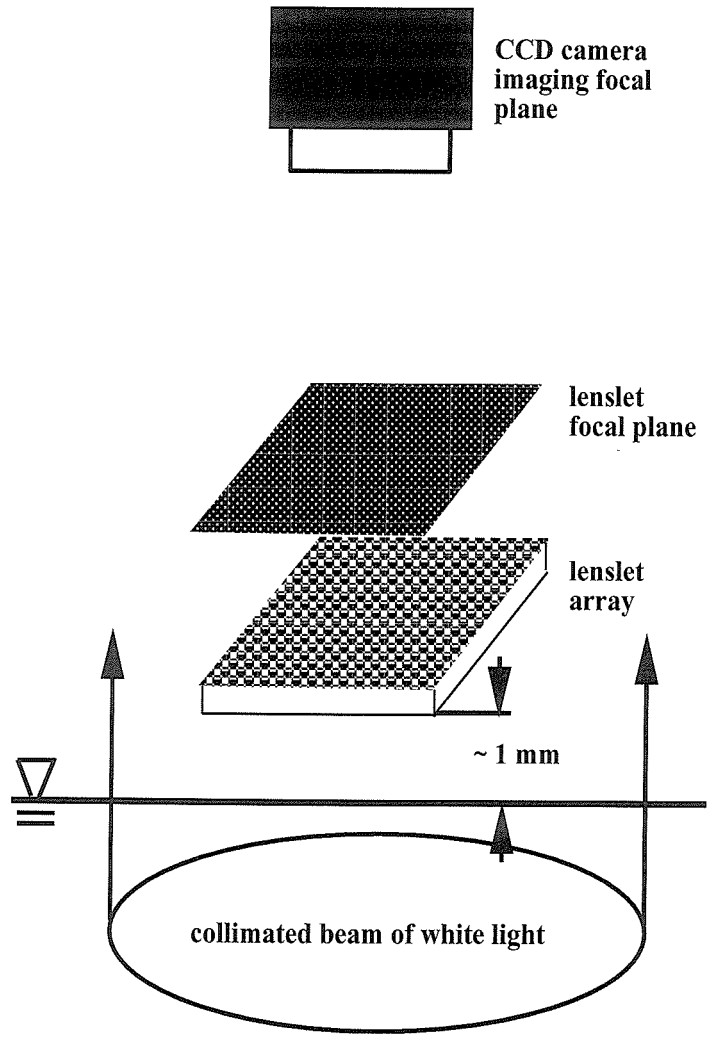

Figure 3.3: Schematic of lenslet technique.

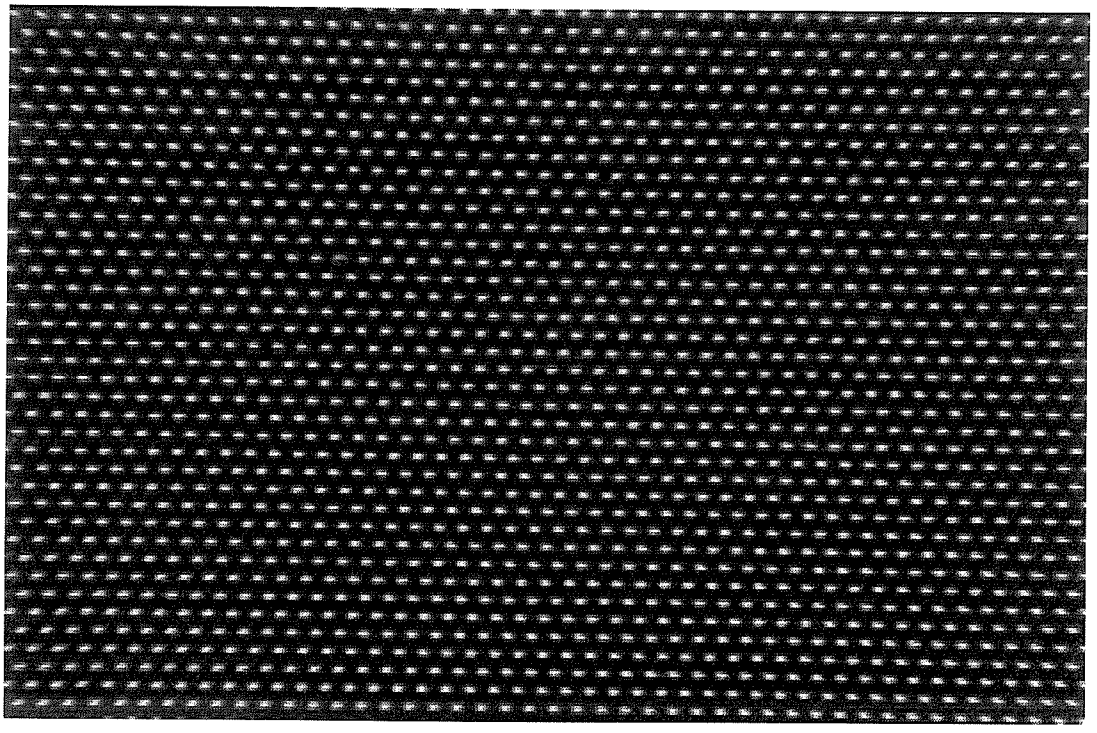

Figure 3.4: Sample image acquired by the CCD camera of the lenslet focal plane.

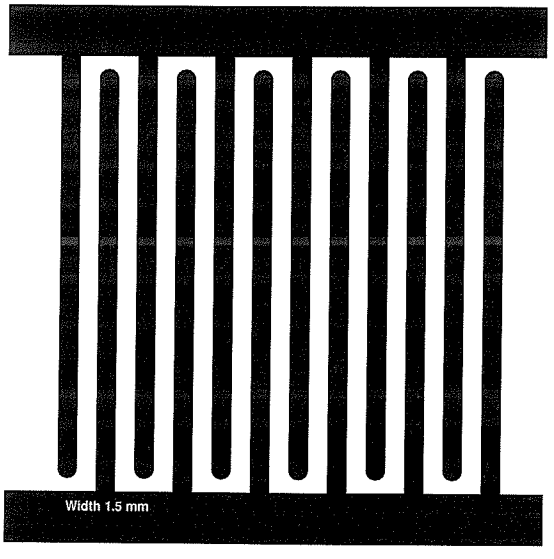

Figure 3.5: Electrode pattern that is electro-coated onto the glass slide (not to scale).

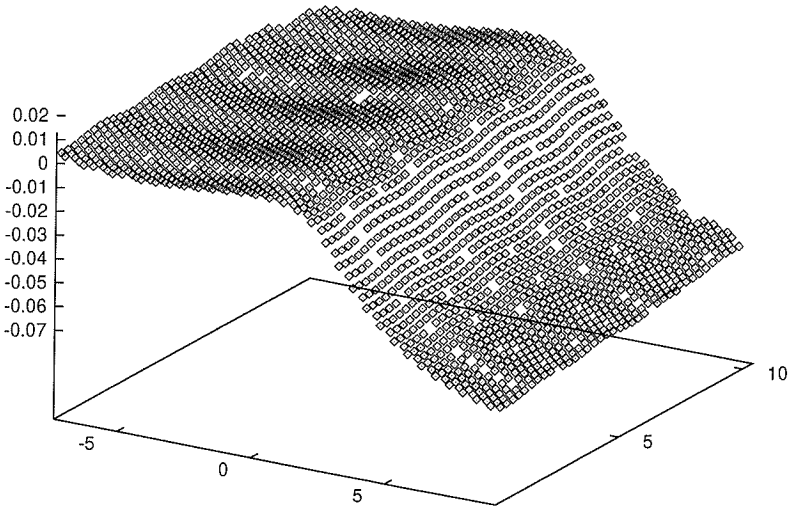

Figure 3.6: Surface deformation when voltage applied and ridge present (axis are in mm).

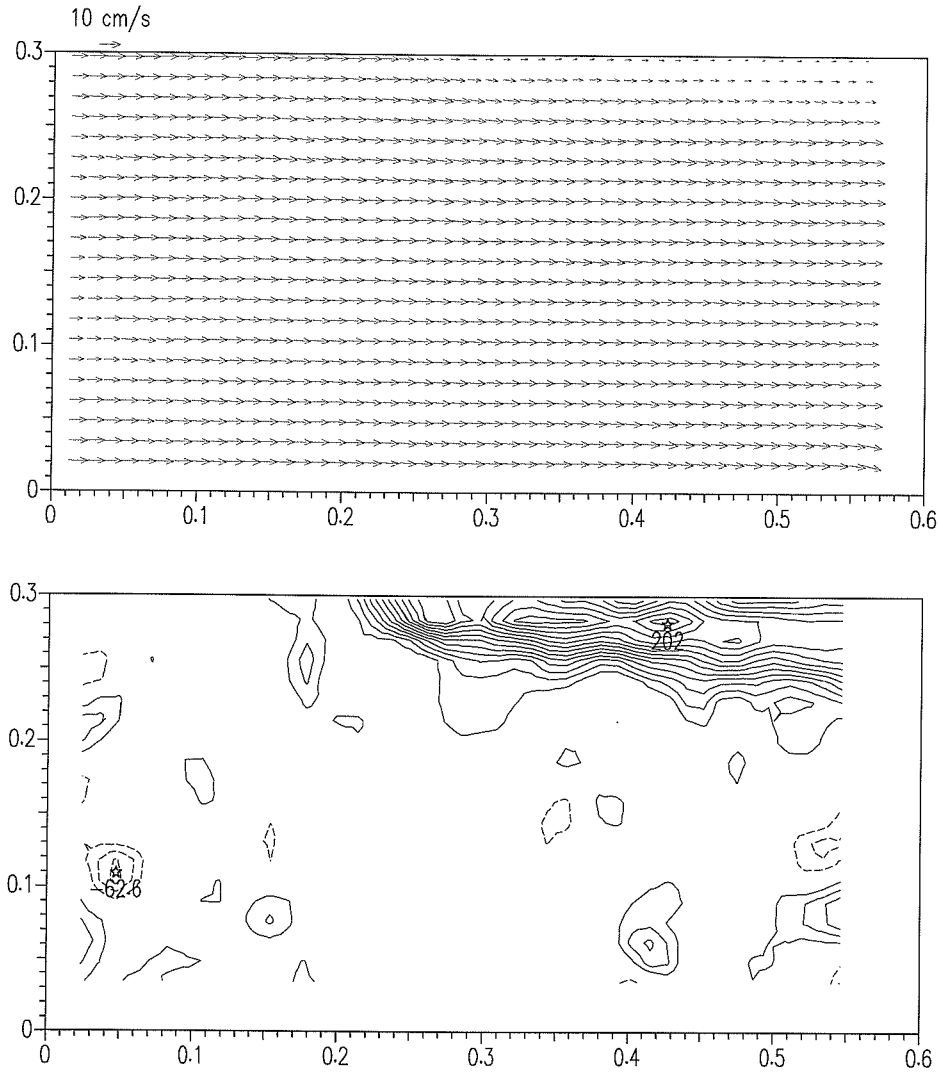

Figure 4.1: Velocity vector field (top) and corresponding vorticity contours (levels 15,30,45,...1/s) for the boundary layer beneath a Reynolds ridge. Axis are in cm.

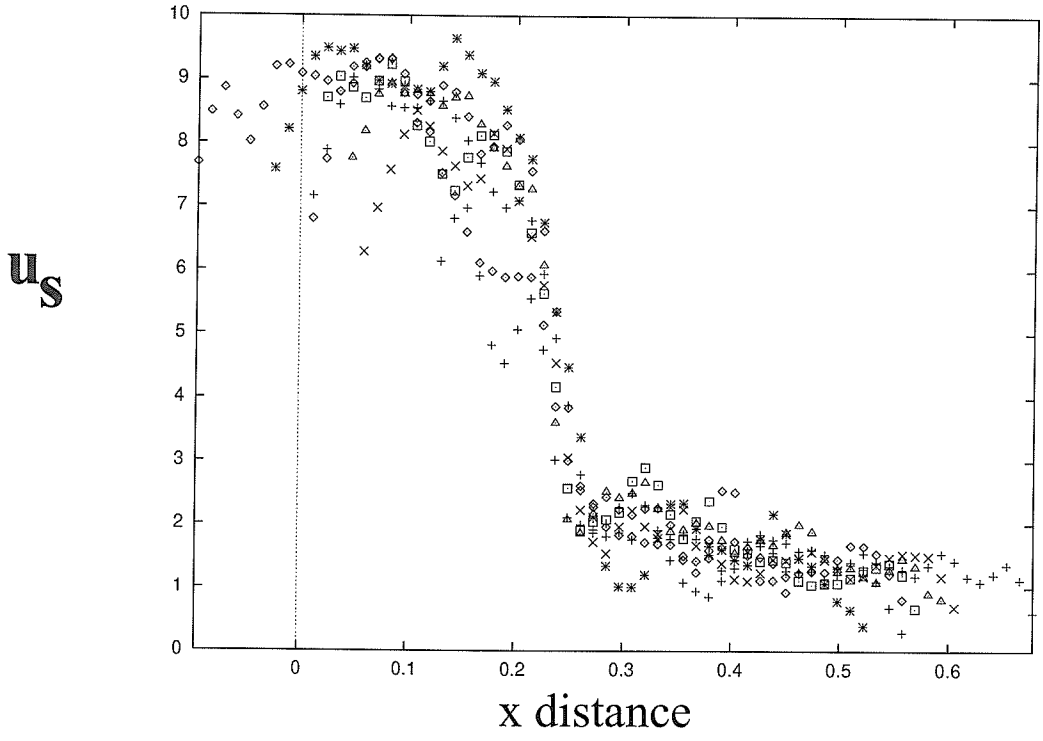

Figure 4.2: Free surface velocity (u_s) in cm/s vs. x distance (cm) for 8 velocity files.

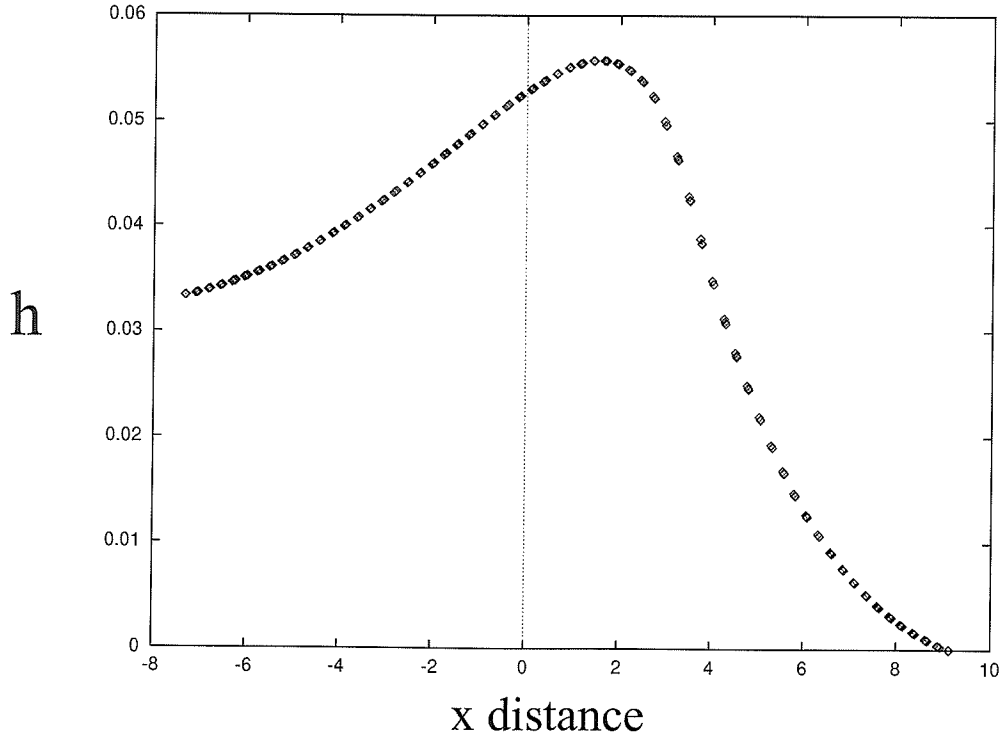

Figure 4.3: Simultaneous surface height (mm) vs. x distance (mm) across the Reynolds ridge.

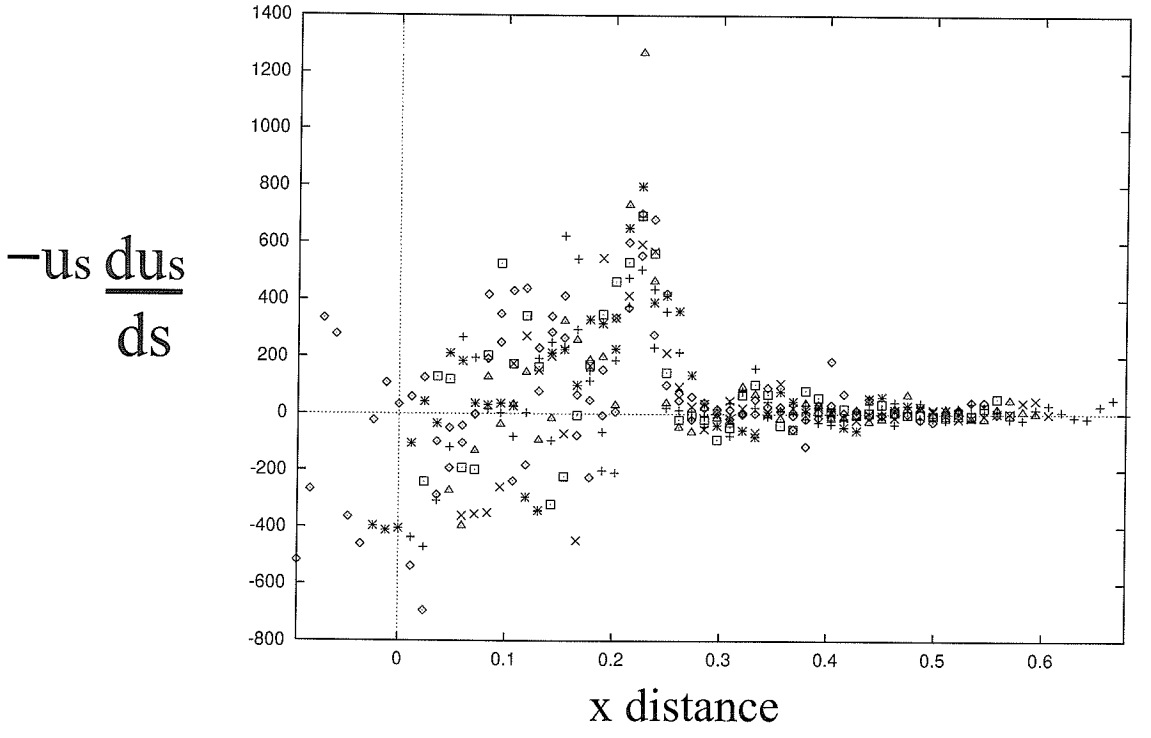

Figure 4.4: Free surface vorticity flux ($-u_s du_s/ds$) in cm/s^2 vs. x distance (cm).

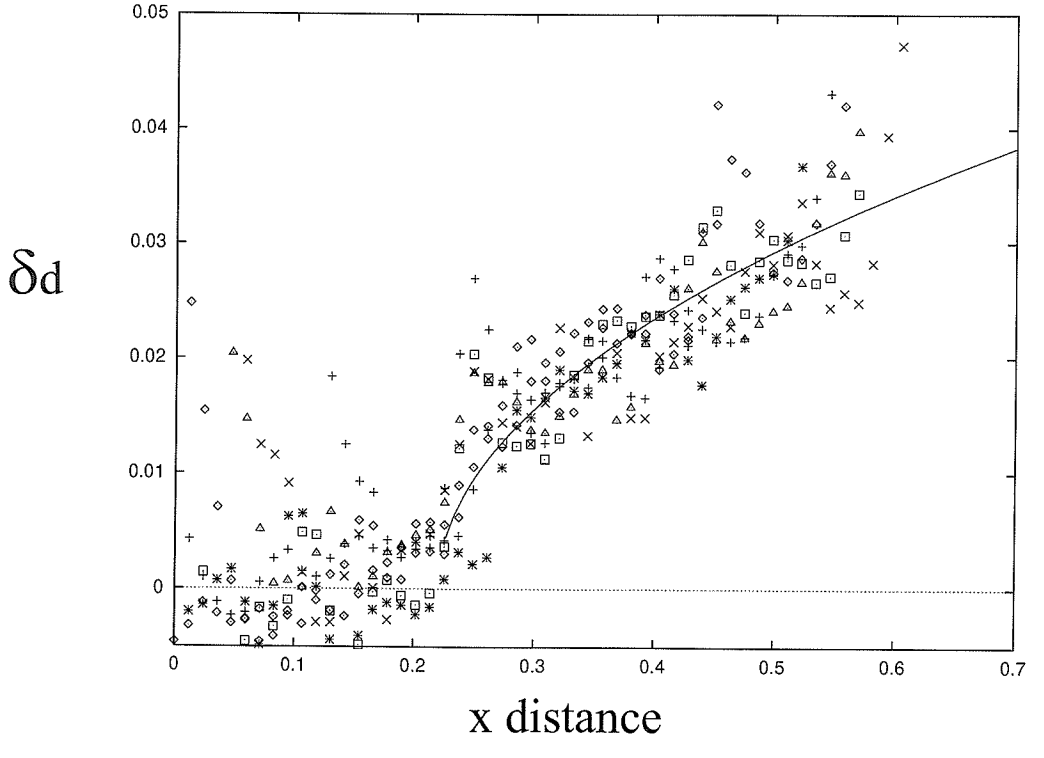

Figure 4.5: Measured displacement thickness (cm) vs. x distance (cm) along with the theoretical flat plate profile (solid line) with an origin at x=0.22 cm.

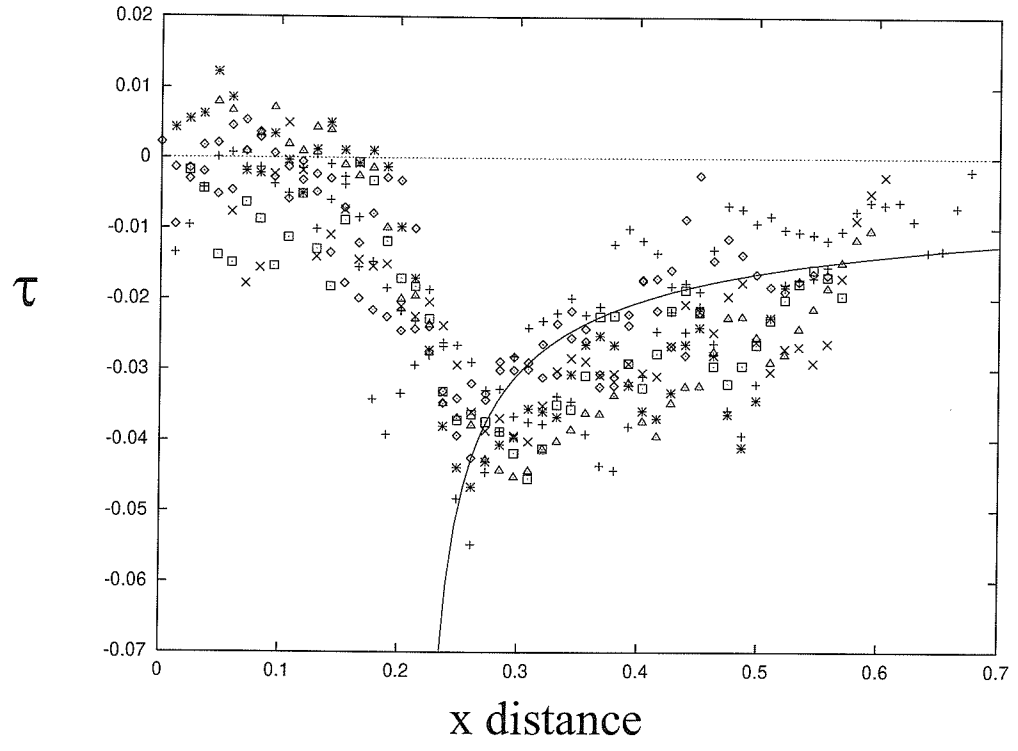

Figure 4.6: Measured surface shear stress (τ) in N/m^2 vs. x- distance (cm) along with the flat plate theoretical profile (solid line) with the origin at x=0.22 cm.

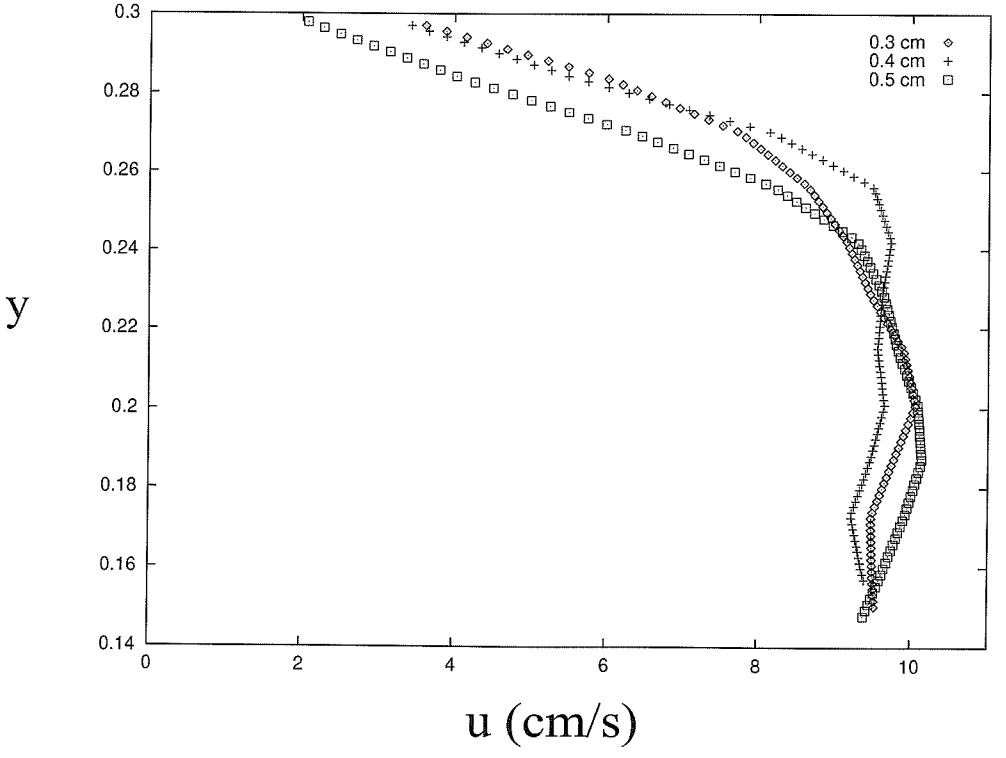

Figure 4.7: Boundary layer profiles. Here y-distance in cm (free surface at 0.3 cm) vs. velocity (u) at three downstream x-distances (see Figure 4.1).

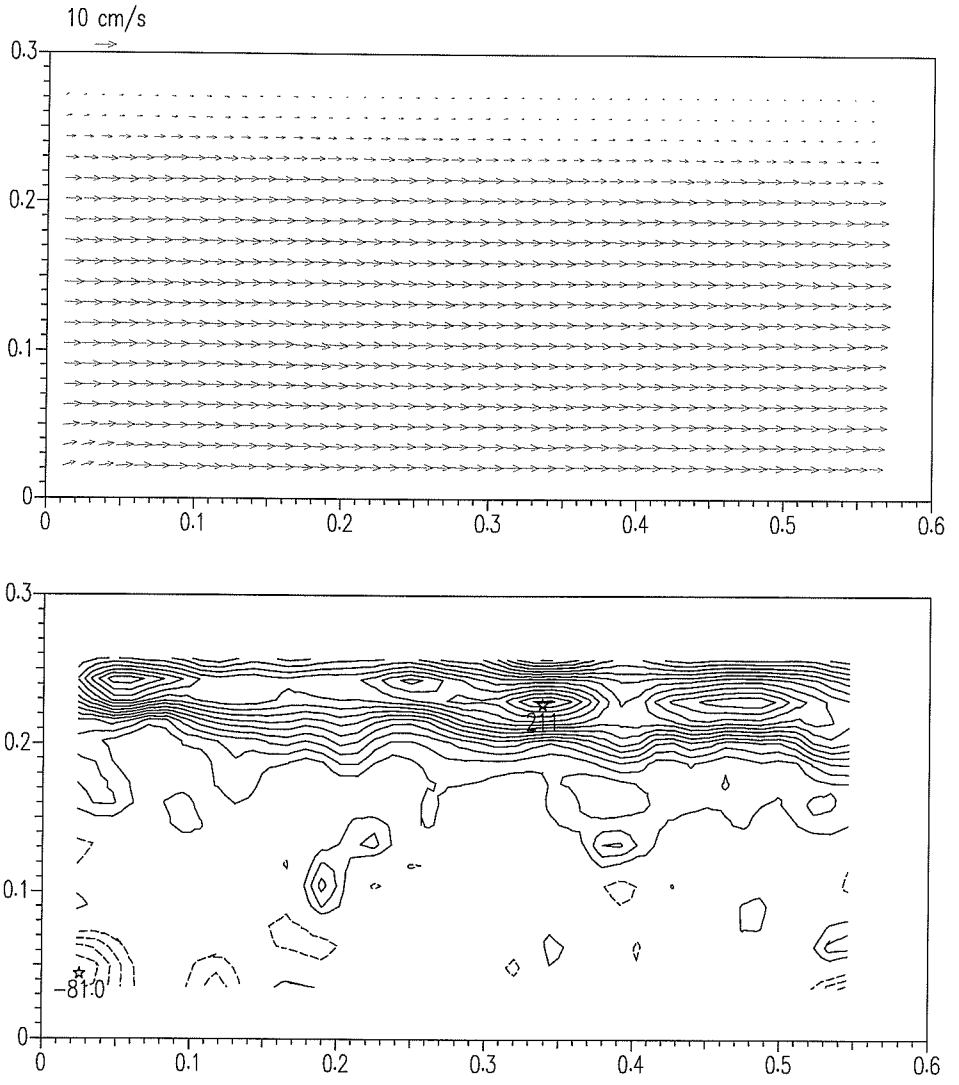

Figure 4.8: Velocity (top) and vorticity (contour levels 15,30,45,...1/s) for a case where the test area is further downstream of the ridge. Axis are in cm.

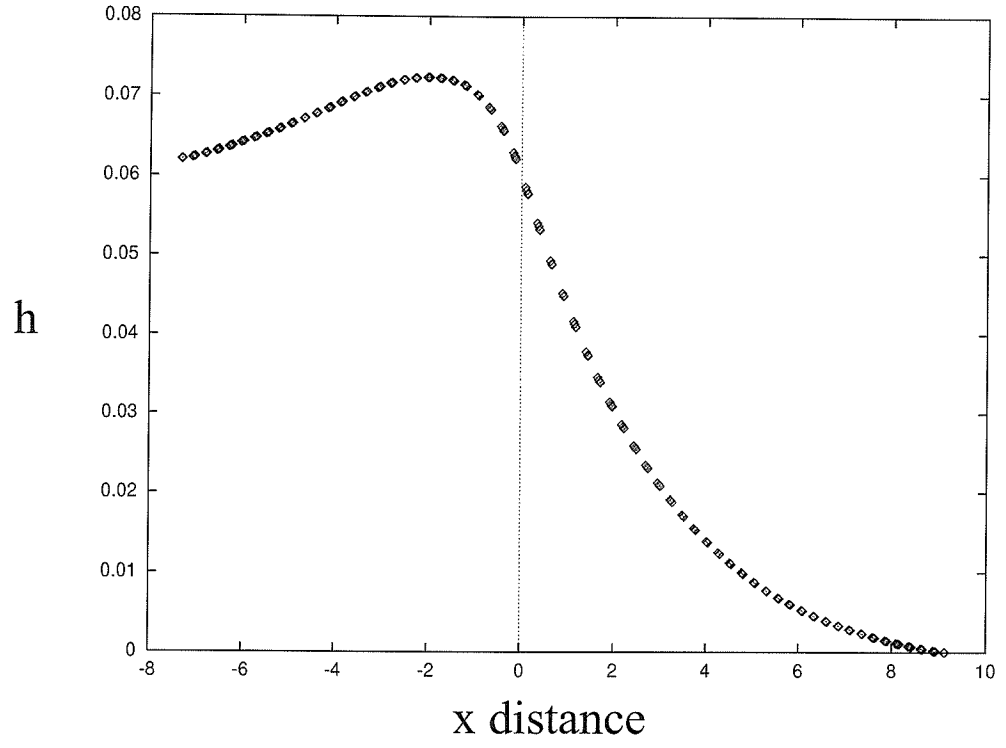

Figure 4.9: Simultaneous height profile (mm) vs. x-distance (mm) across the Reynolds ridge corresponding to Figure 4.8.

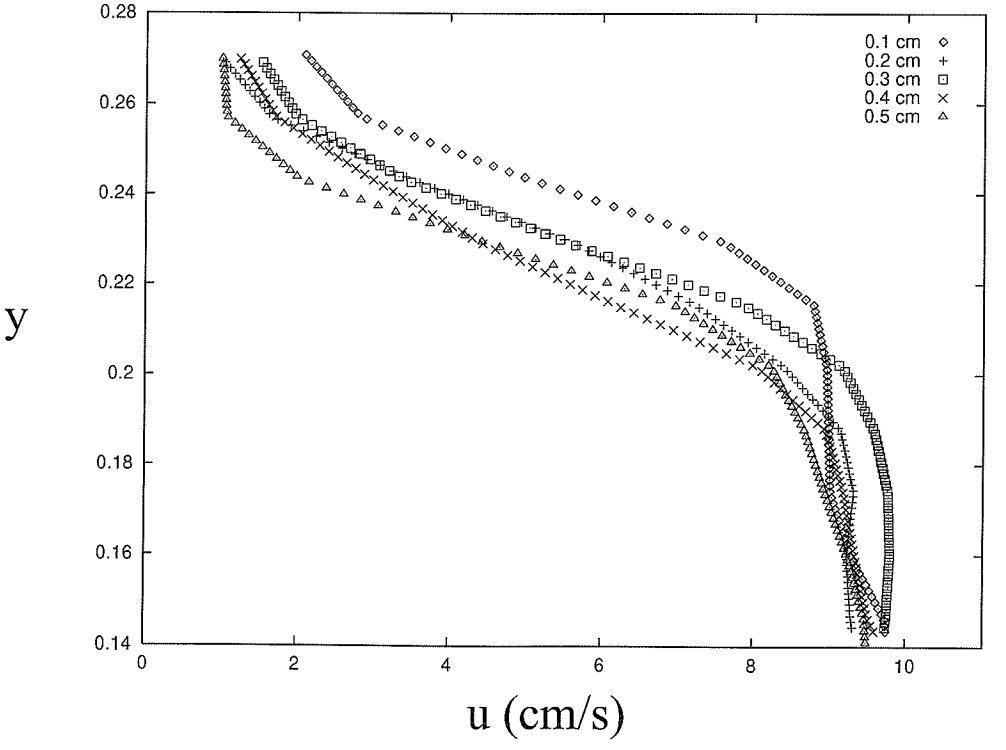

Figure 4.10: Boundary layer profiles where ridge slightly upstream. Here y-distance in cm (free surface at 0.27 cm) vs. velocity (u) at five downstream x-distances (see Figure 4.8).

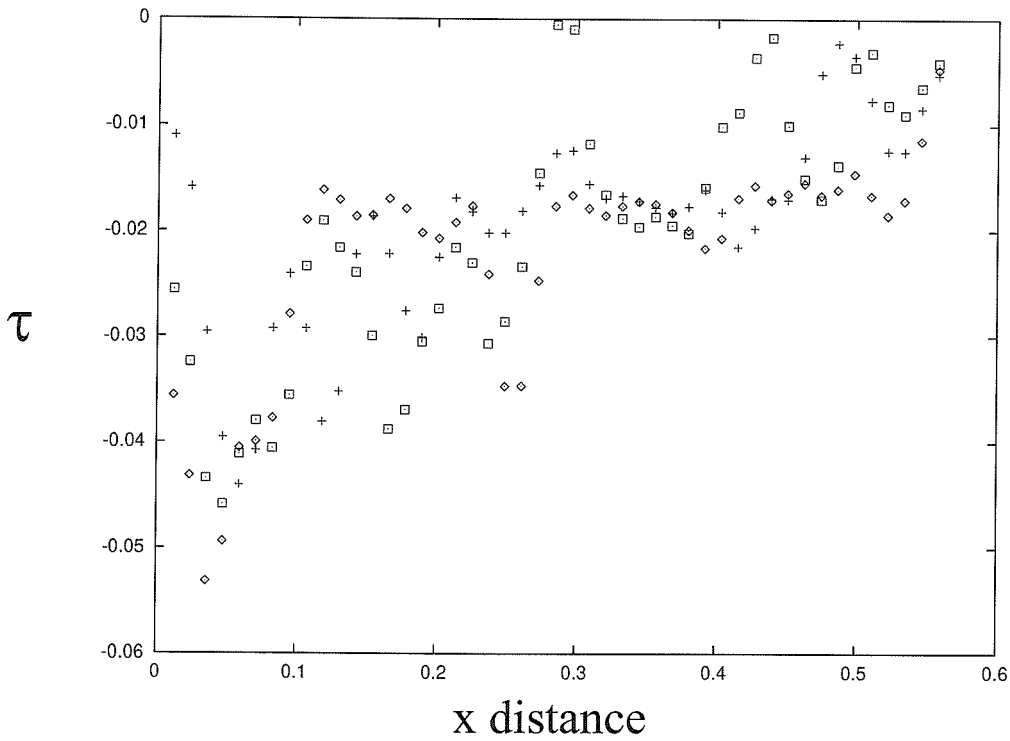

Figure 4.11: Measured surface shear stress (τ) in N/m^2 vs.x-distance (cm) where ridge slightly upstream.

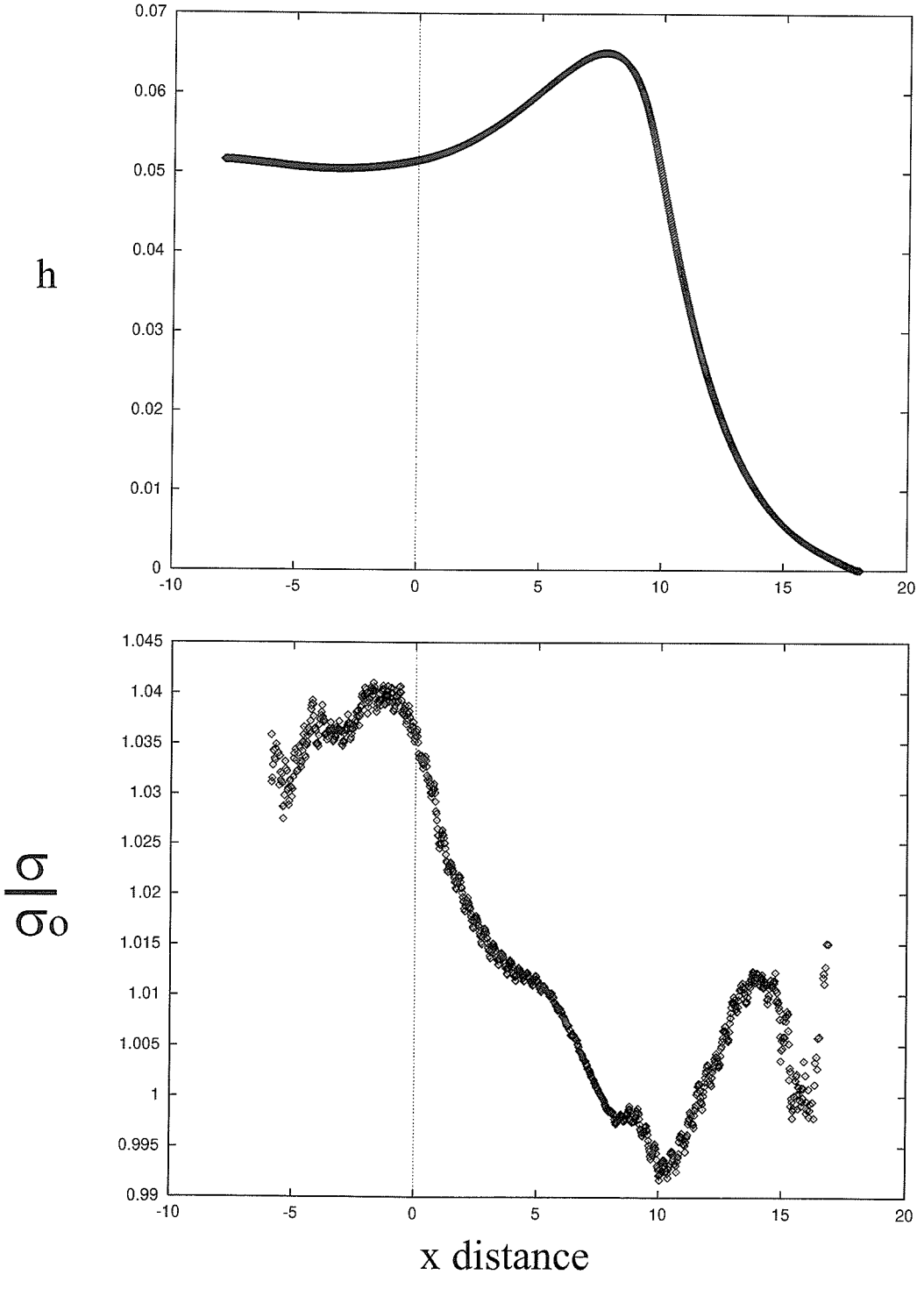

Figure 4.12: Measured surface height in mm vs. x-distance in mm (top) and relative surface tension vs. x-distance (bottom) across the Reynolds ridge.

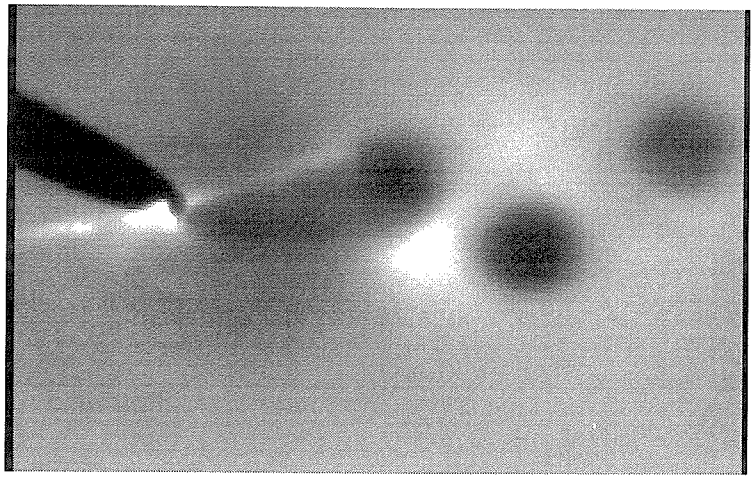

Re=350

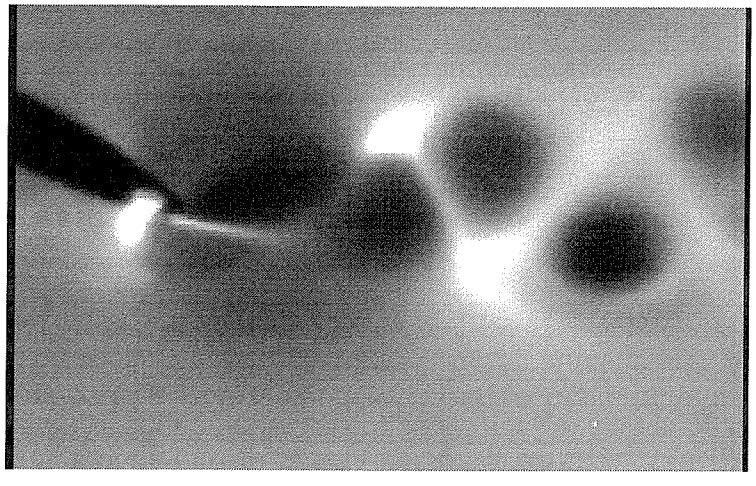

Re=460

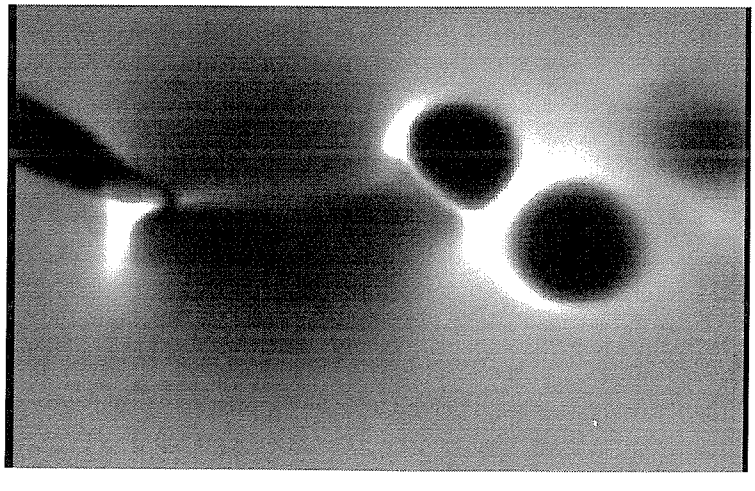

Re=560

Figure 4.13: Shadowgraph images for cylinder near wake with a clean free surface (area imaged approximately 3 cm X 2 cm).

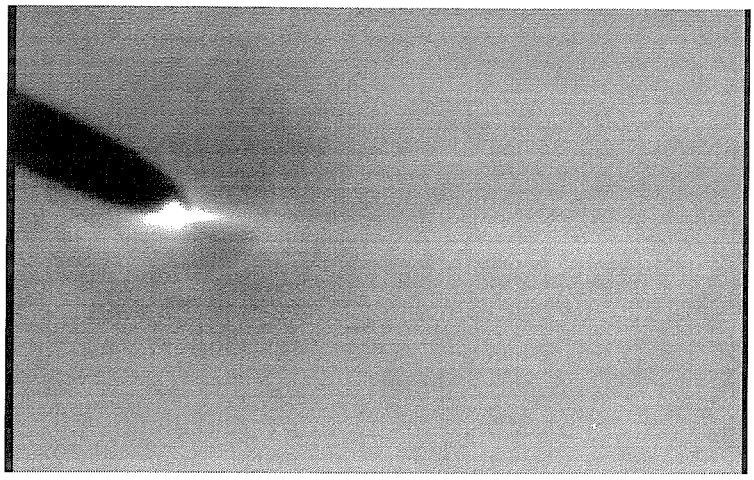

Re=350

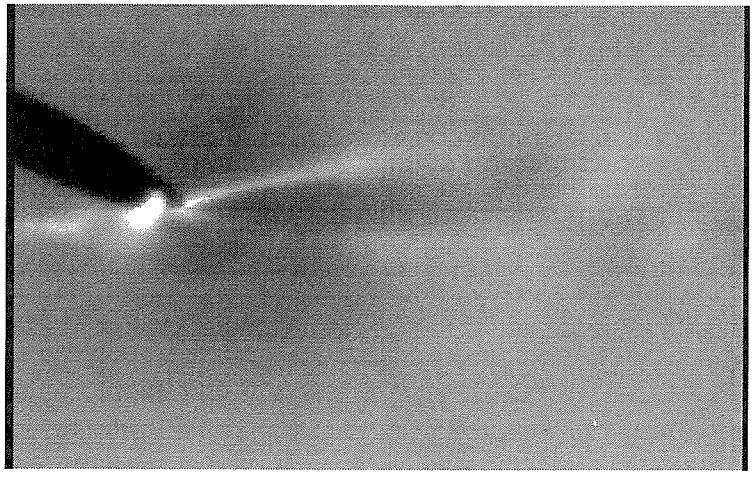

Re=460

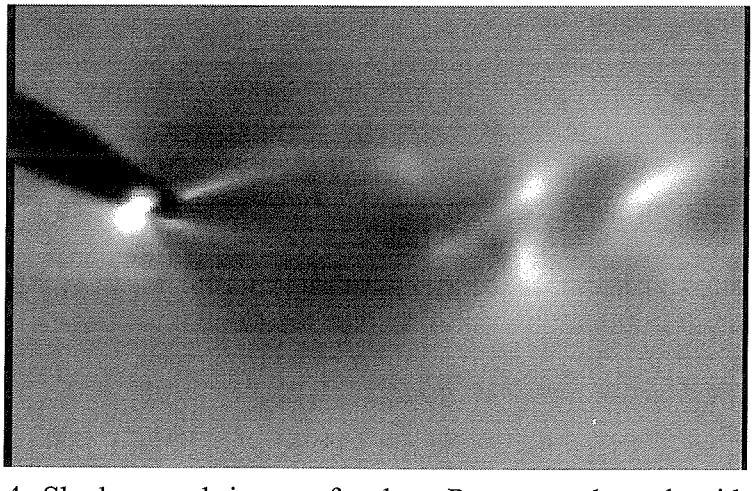

Re=560

Figure 4.14: Shadowgraph images for three Re cases where the ridge is upstream of the cylinder (contaminated wake).

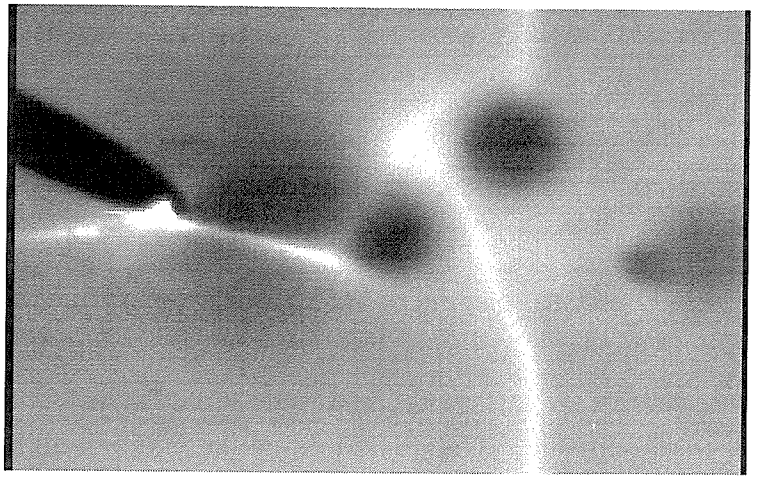

Re=350

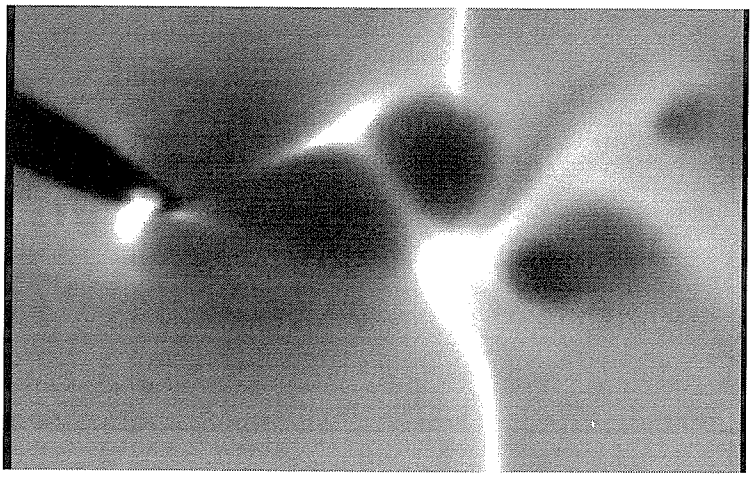

Re=460

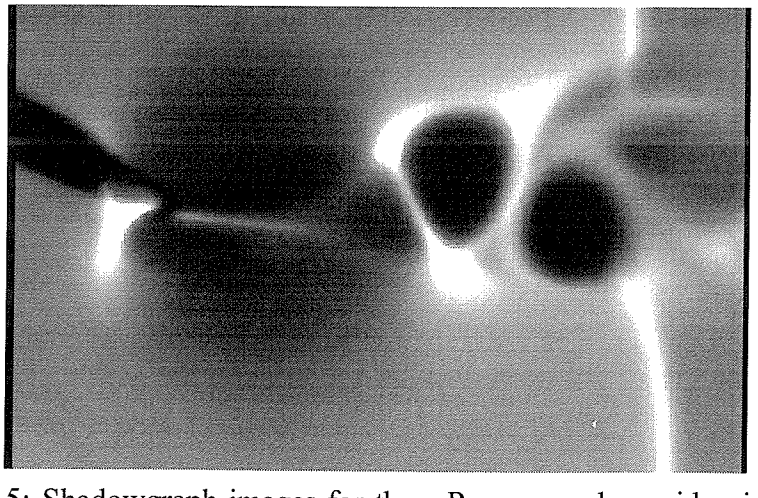

Re=560

Figure 4.15: Shadowgraph images for three Re cases where ridge is in the wake of the cylinder (unattached).

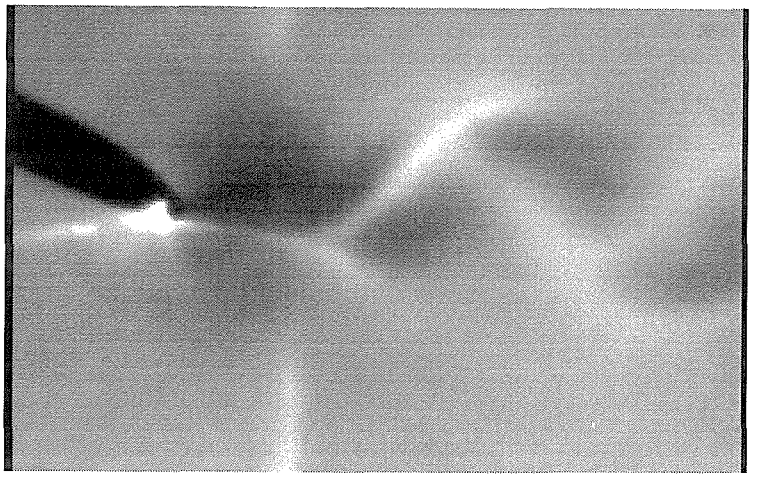

Re=350

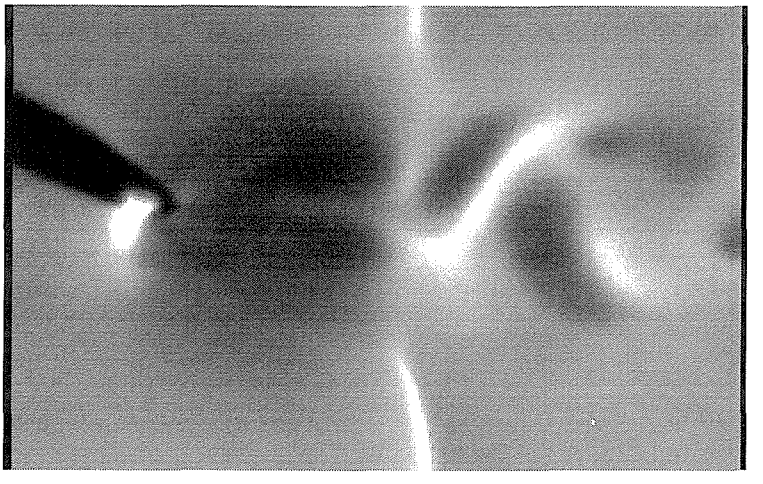

Re=460

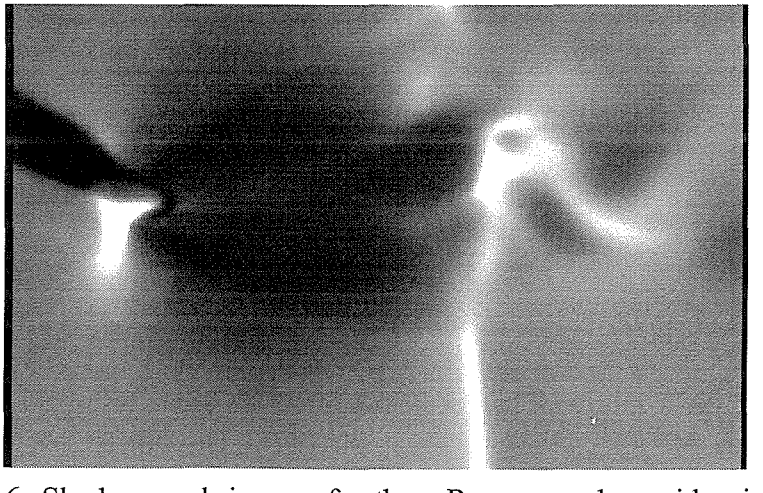

Re=560

Figure 4.16: Shadowgraph images for three Re cases where ridge is in the wake of the cylinder (attached).

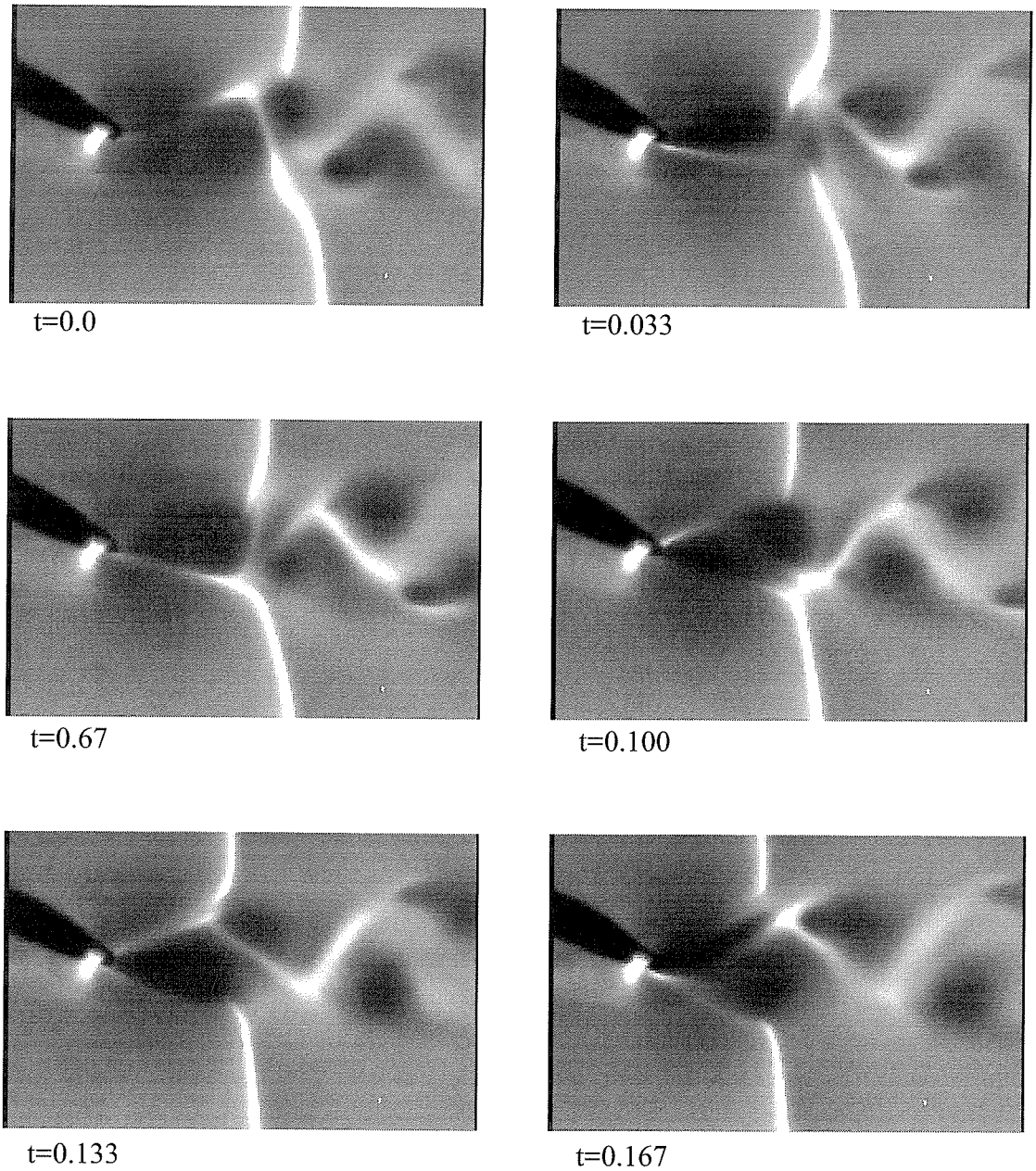

Figure 4.17: Sequence of shadowgraph images for Re=460 with ridge in the near vicinity of the cylinder (showing the attachment process).

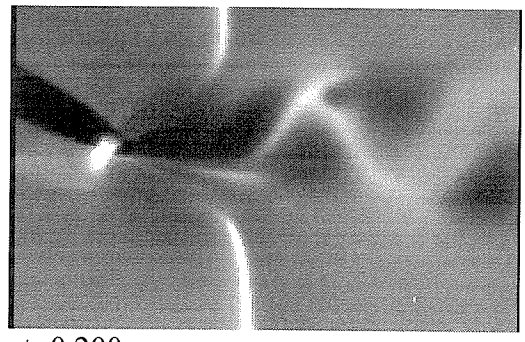

t=0.200

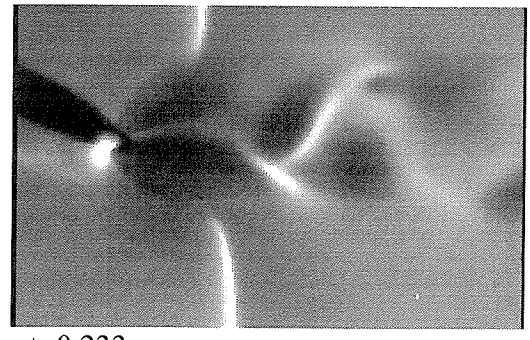

t=0.233

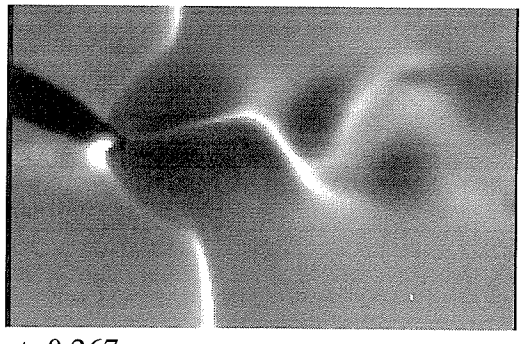

t=0.267

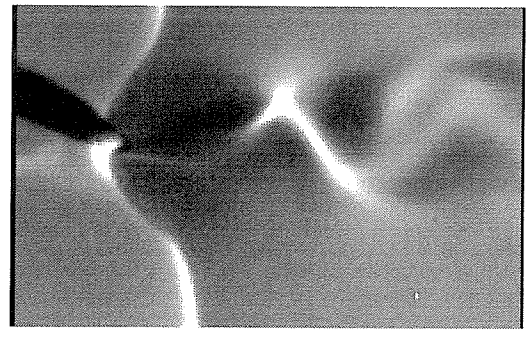

t=0.300

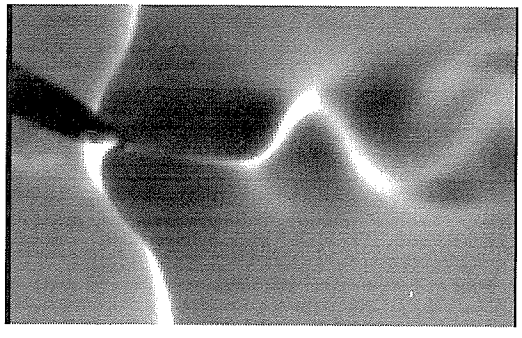

t=0.333

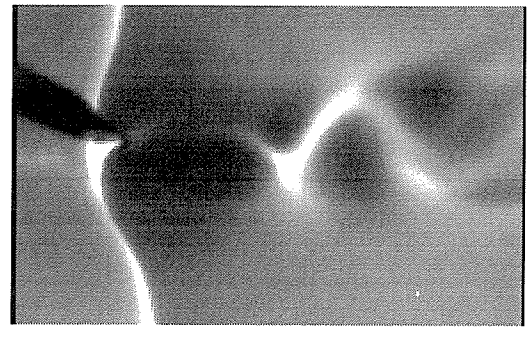

t=0.367

Figure 4.17: continued.

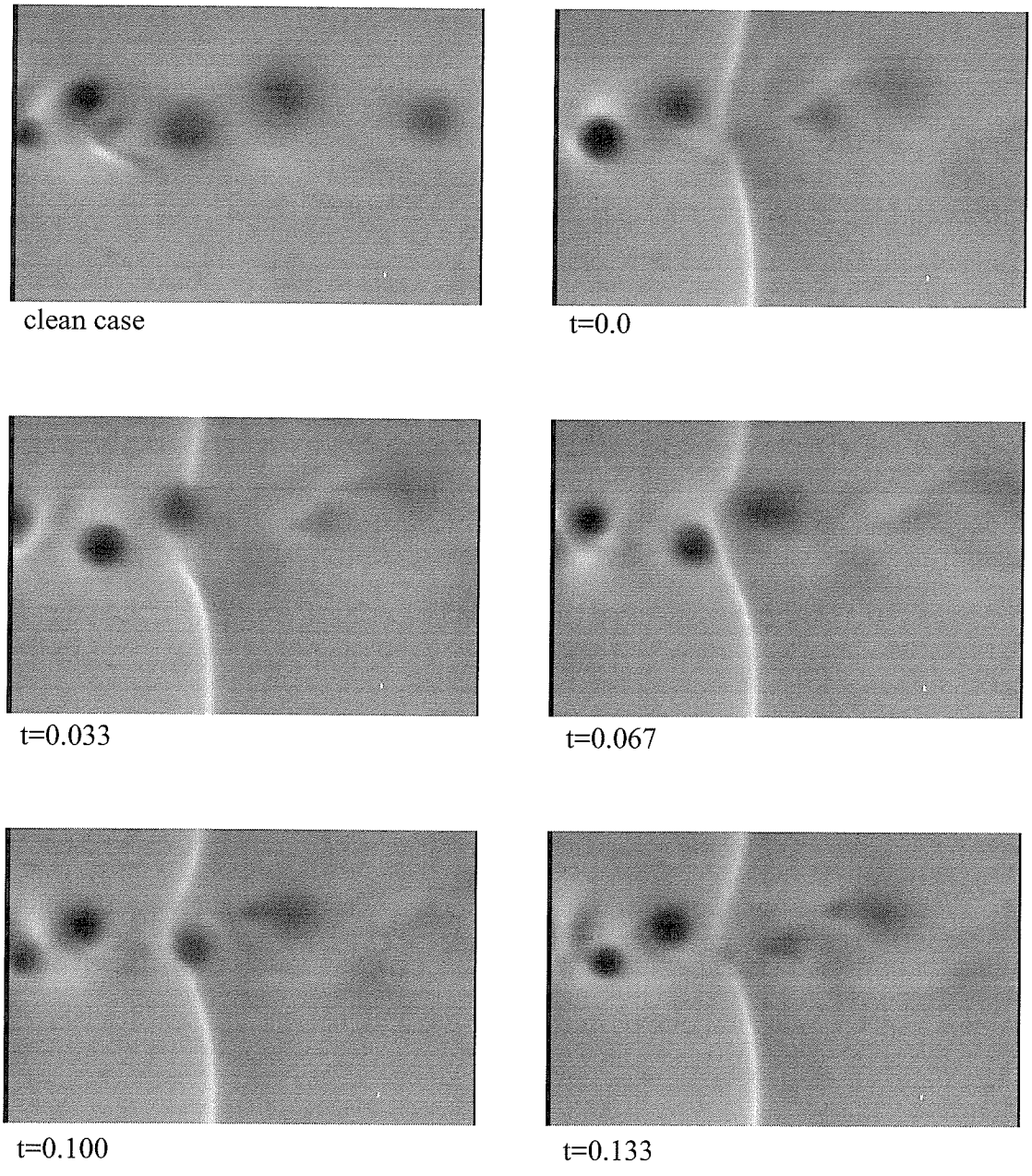

Figure 4.18: Shadowgraph images farther down in the wake (Re=460 and cylinder was moved 2 cm upstream compared to previous images).

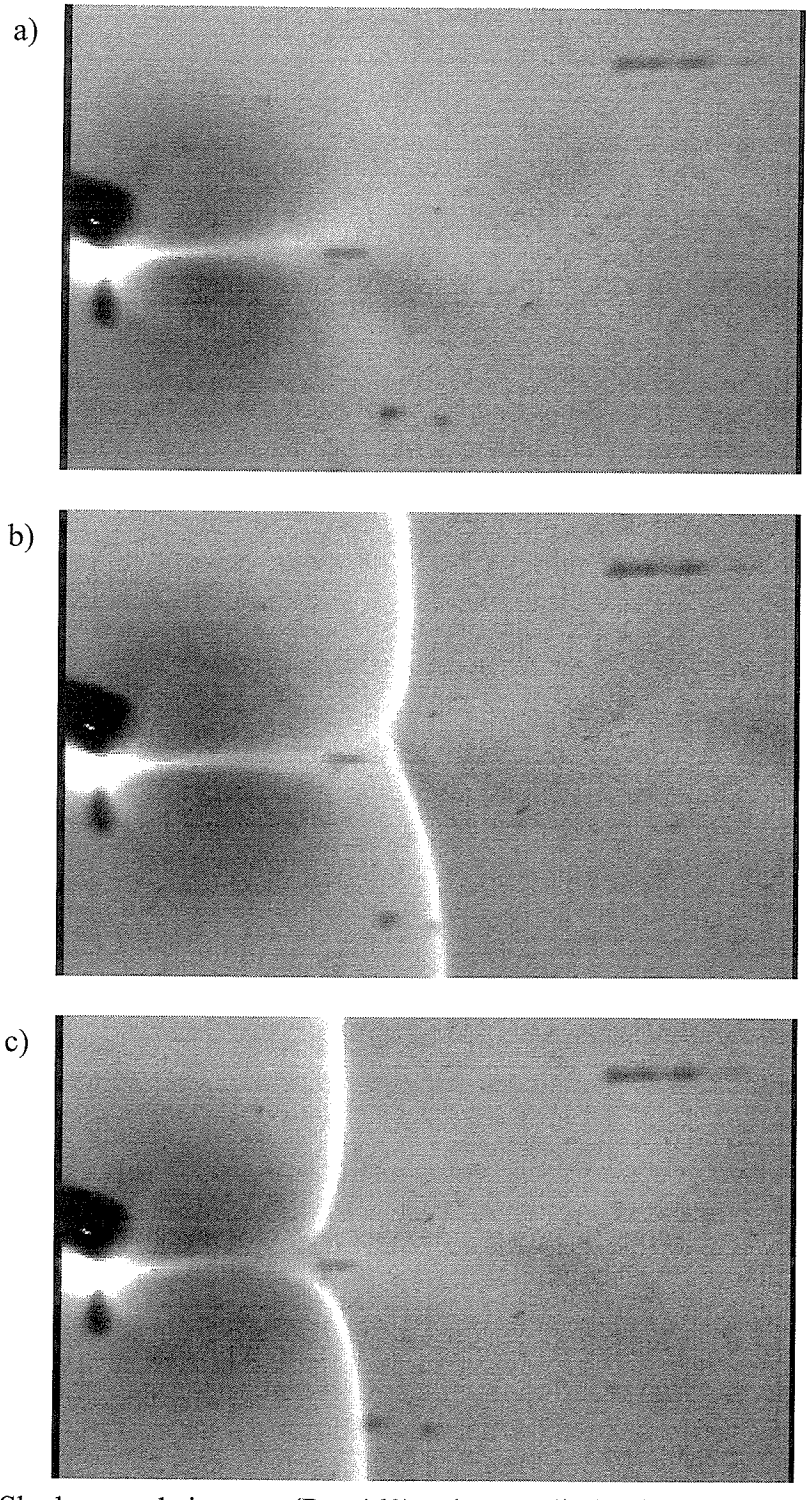

Figure 4.19: Shadowgraph images (Re=460) where cylinder is contaminated for three cases where ridge is far downstream (a) and ridge in near vicinity of the cylinder (b) and closer to cylinder (c) where ridge is not attaching to cylinder. Note that dark spots are due to scratches on test section.

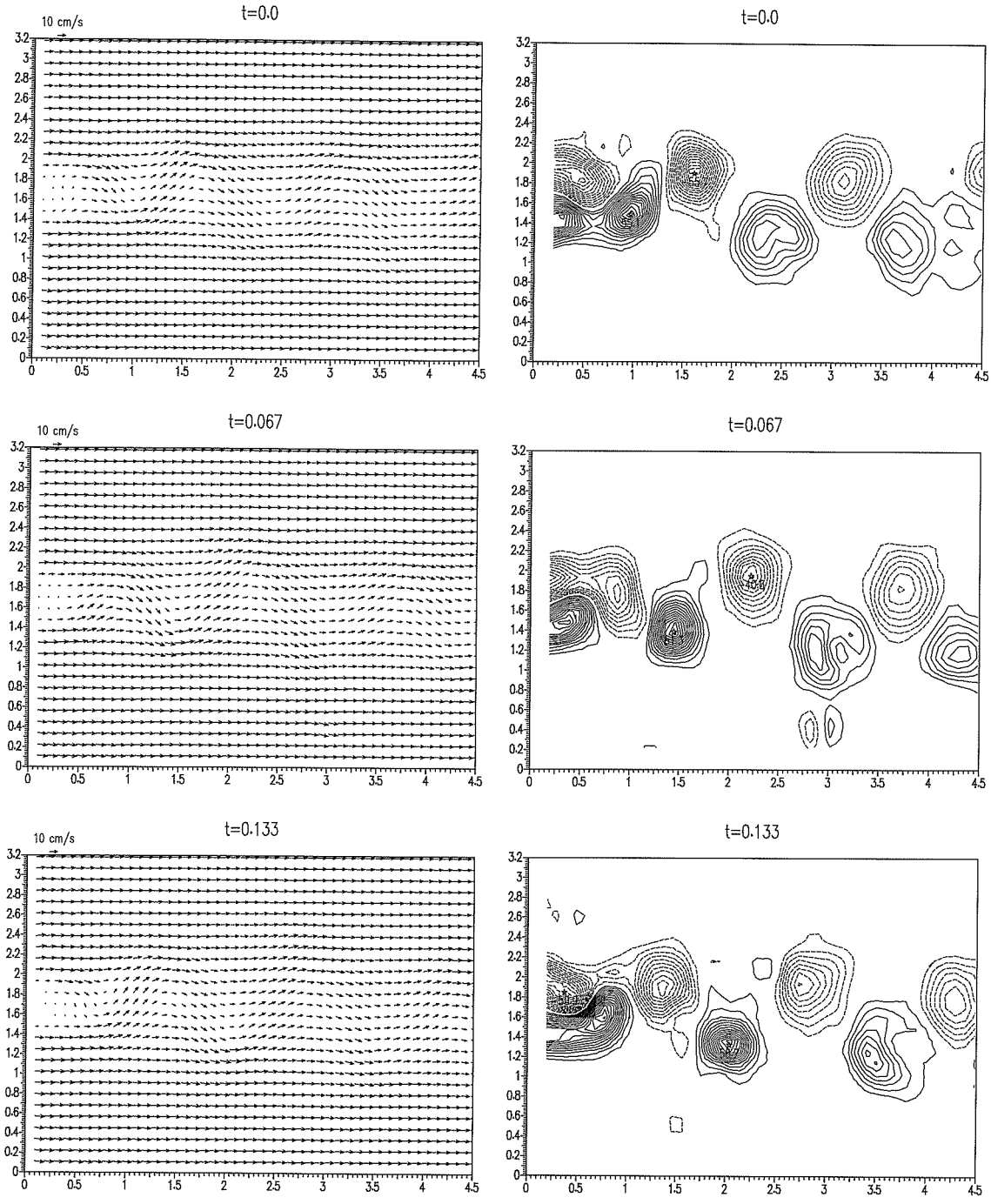

Figure 4.20: Sequence of velocity/vorticity plots (vorticity contour levels 4,8,12,..1/s) for a clean free surface (axis units are centimeters and time is in seconds).

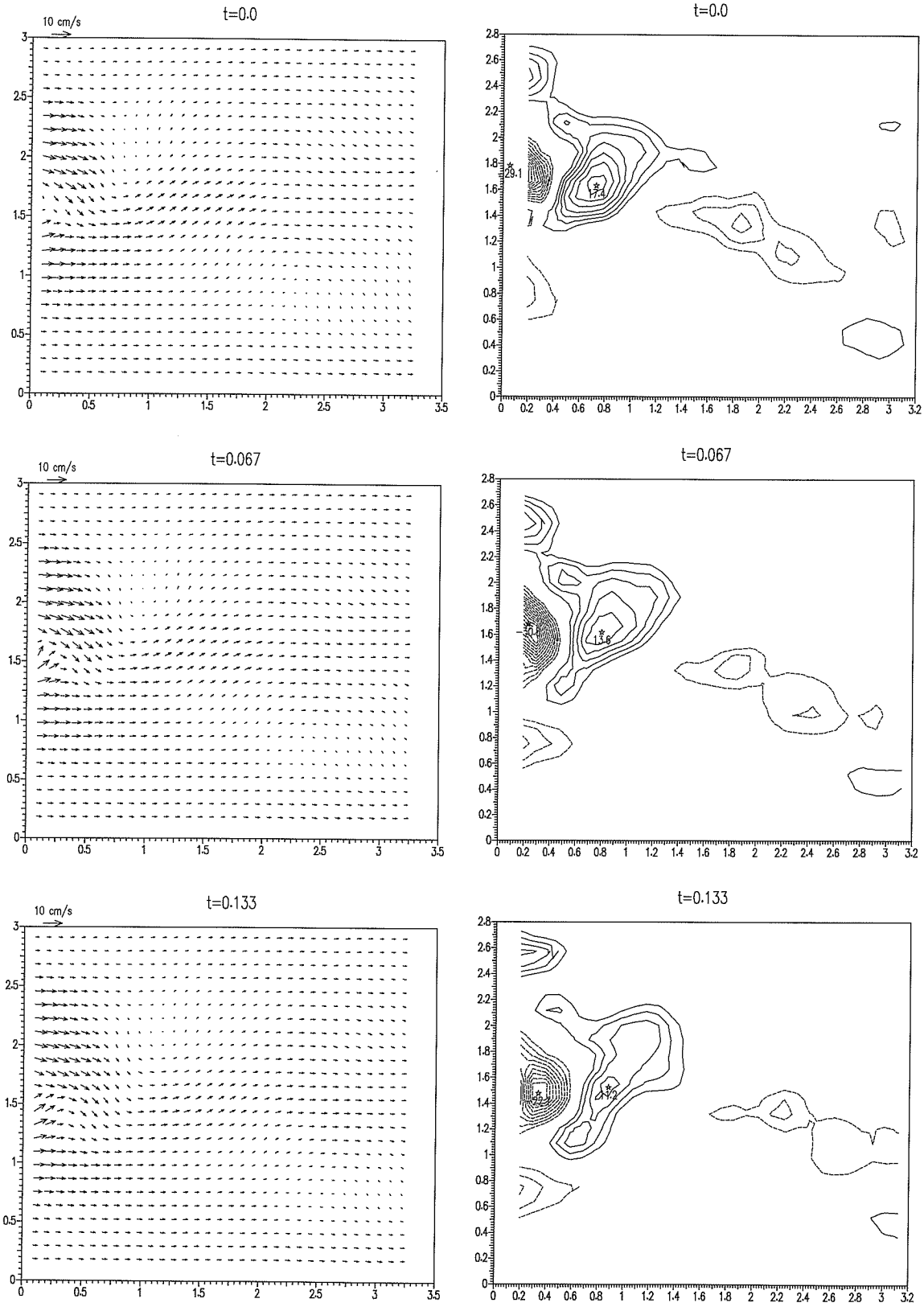

Figure 4.21: Sequence of velocity/vorticity (4,6,8...1/s) plots for the contaminated wake.

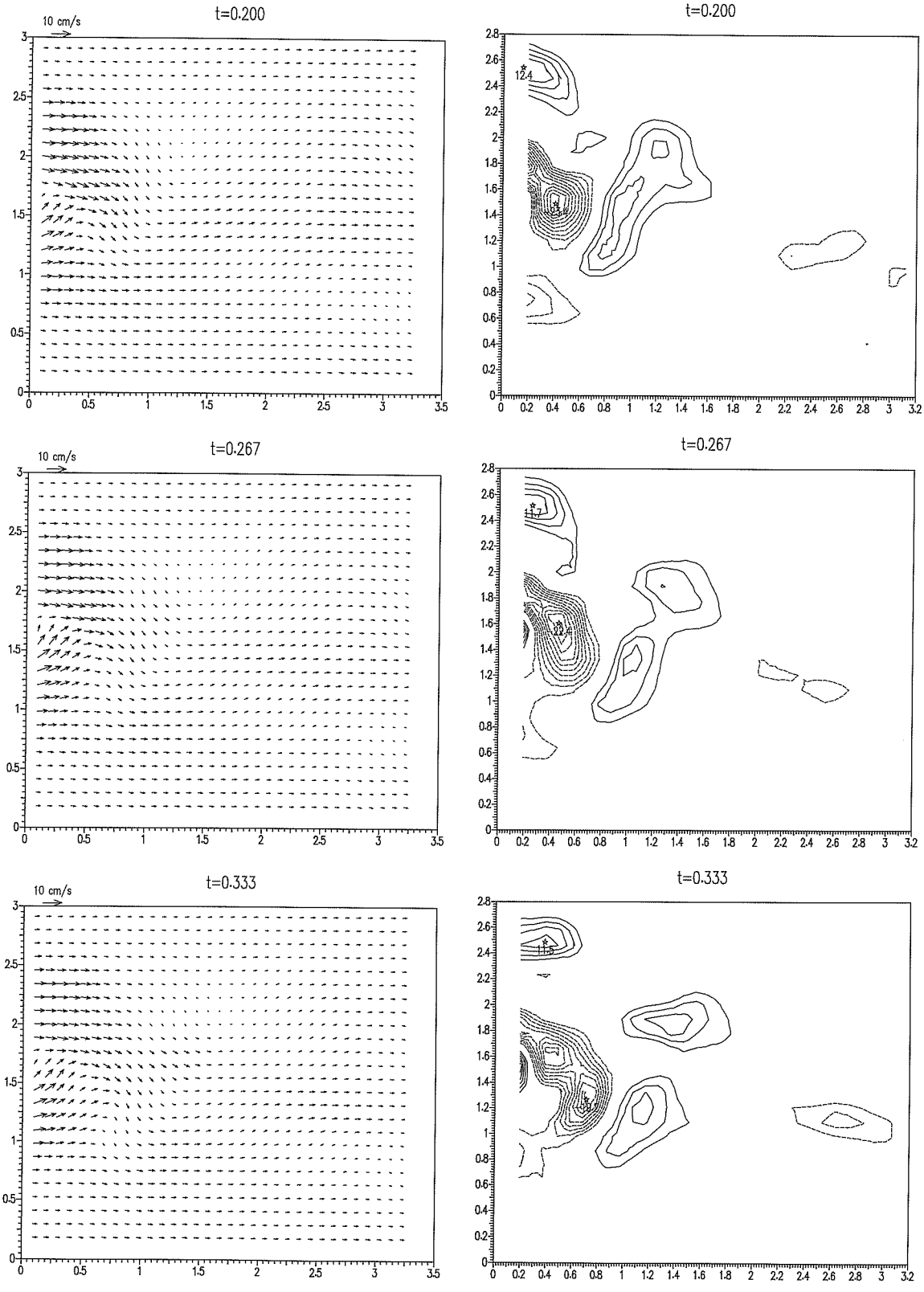

Figure 4.21: continued.

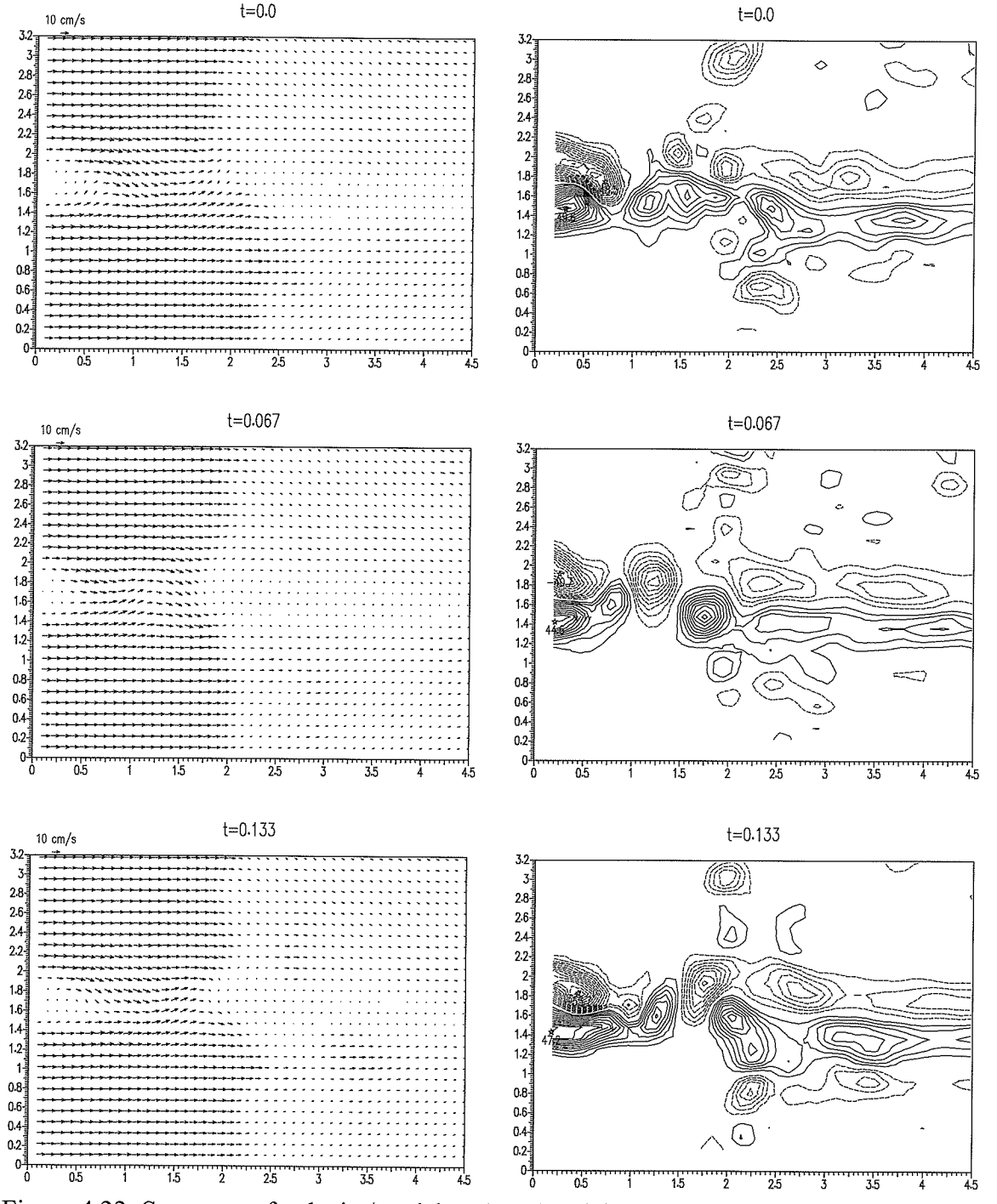

Figure 4.22: Sequence of velocity/vorticity plots (vorticity contour levels 4,8,12,..1/s) for the ridge in the wake of the cylinder (axis units in centimeters and time in seconds).

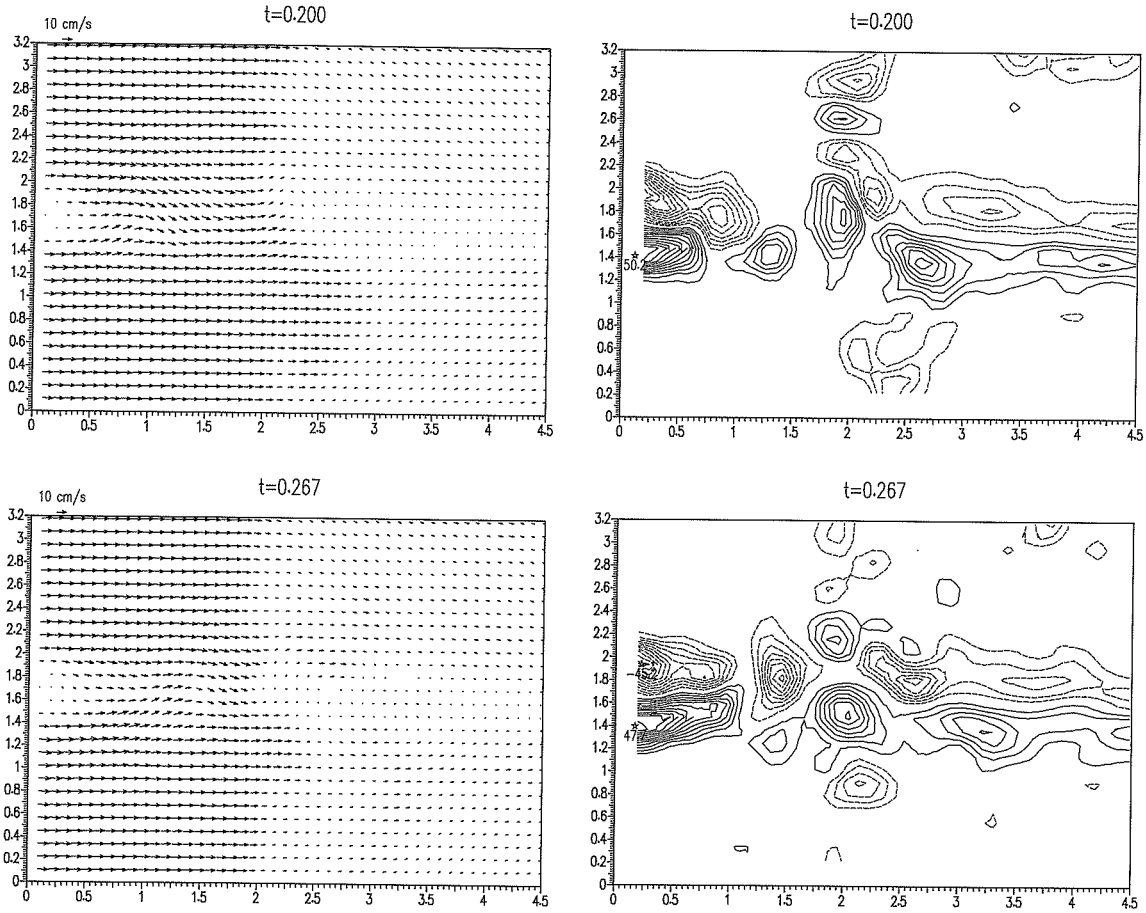

Figure 4.22: continued.

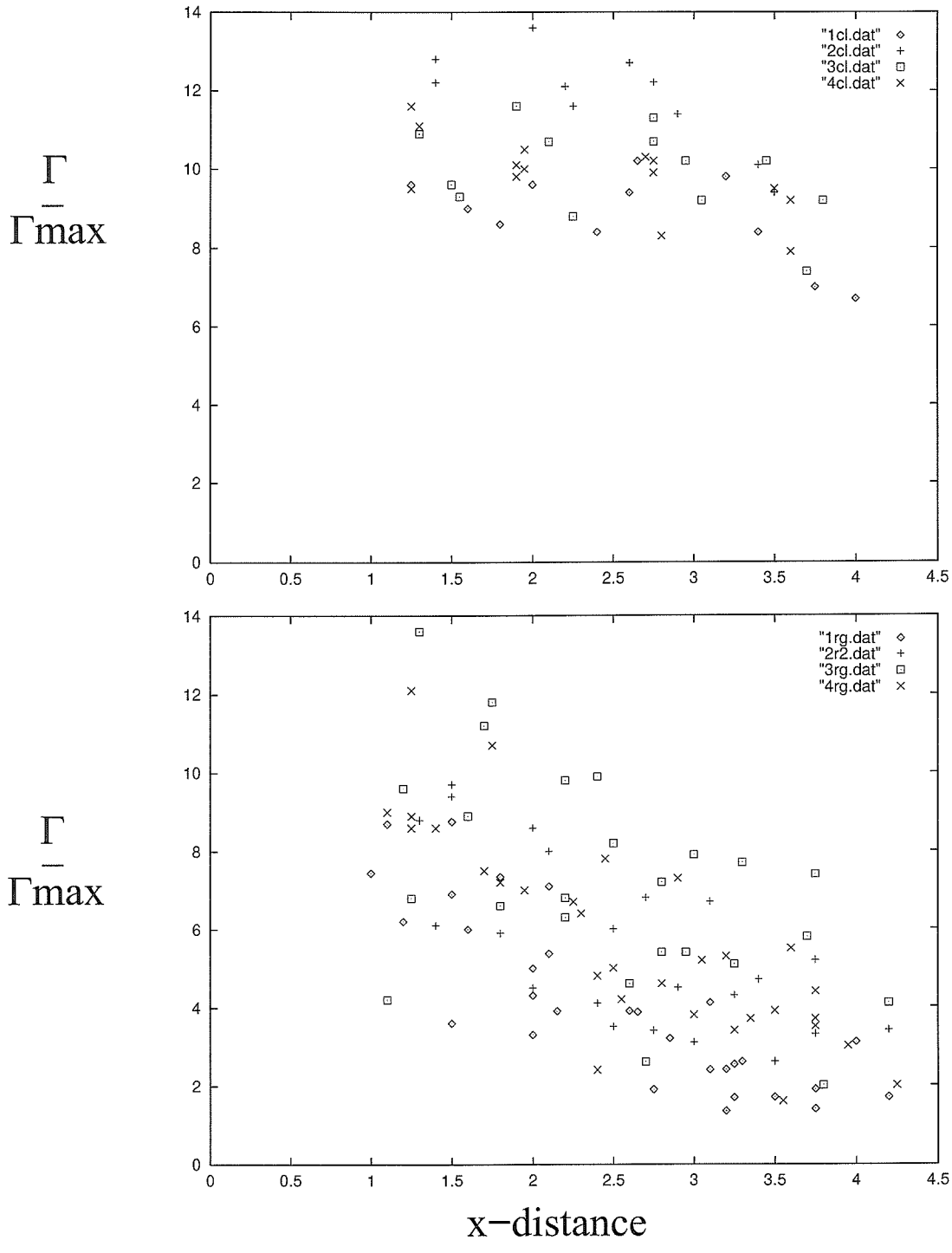

Figure 4.23: Plots of circulation (y-axis) normalized with respect to the maximum circulation for each run for shedding vortex filaments at various downstream distances (x-axis in cm) for a clean free surface (top plot) and for the case where the ridge is sitting at approximately x=1.5 cm (bottom plot).

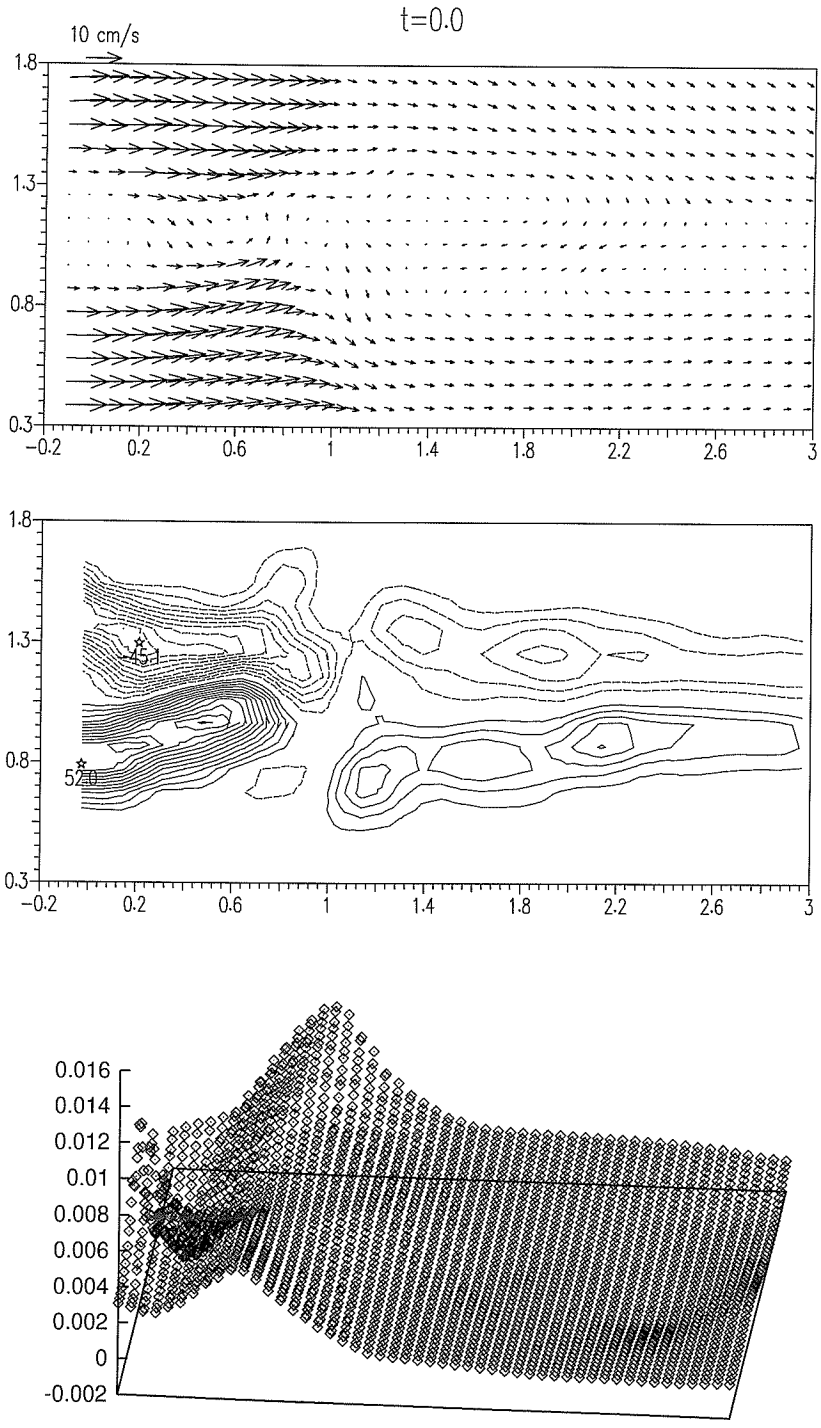

Figure 4.24: Sequence of simultaneous velocity/vorticity (contour levels 4,8,12...1/s) and free-surface height (mm) measurements showing the attachment process.

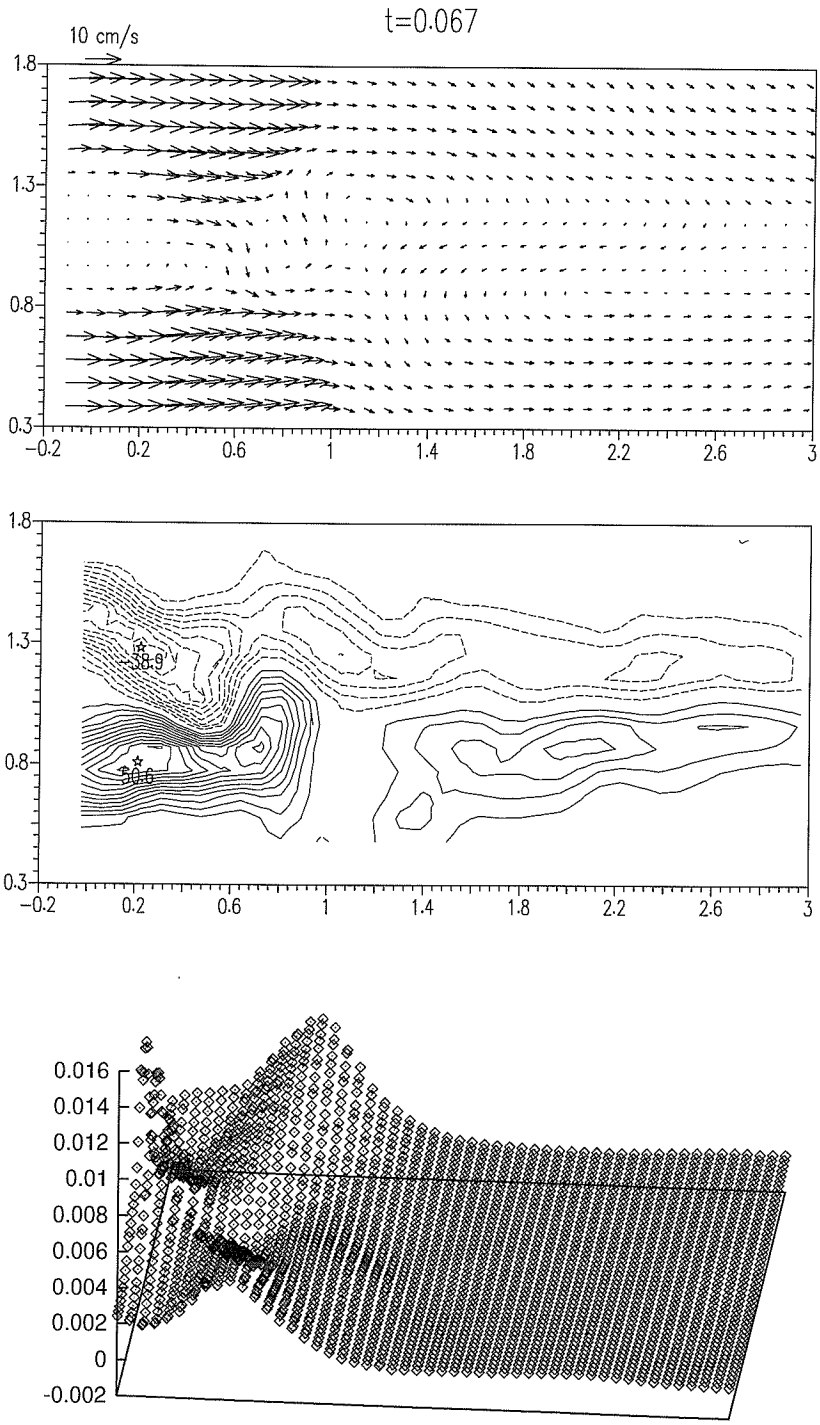

Figure 4.24: continued.

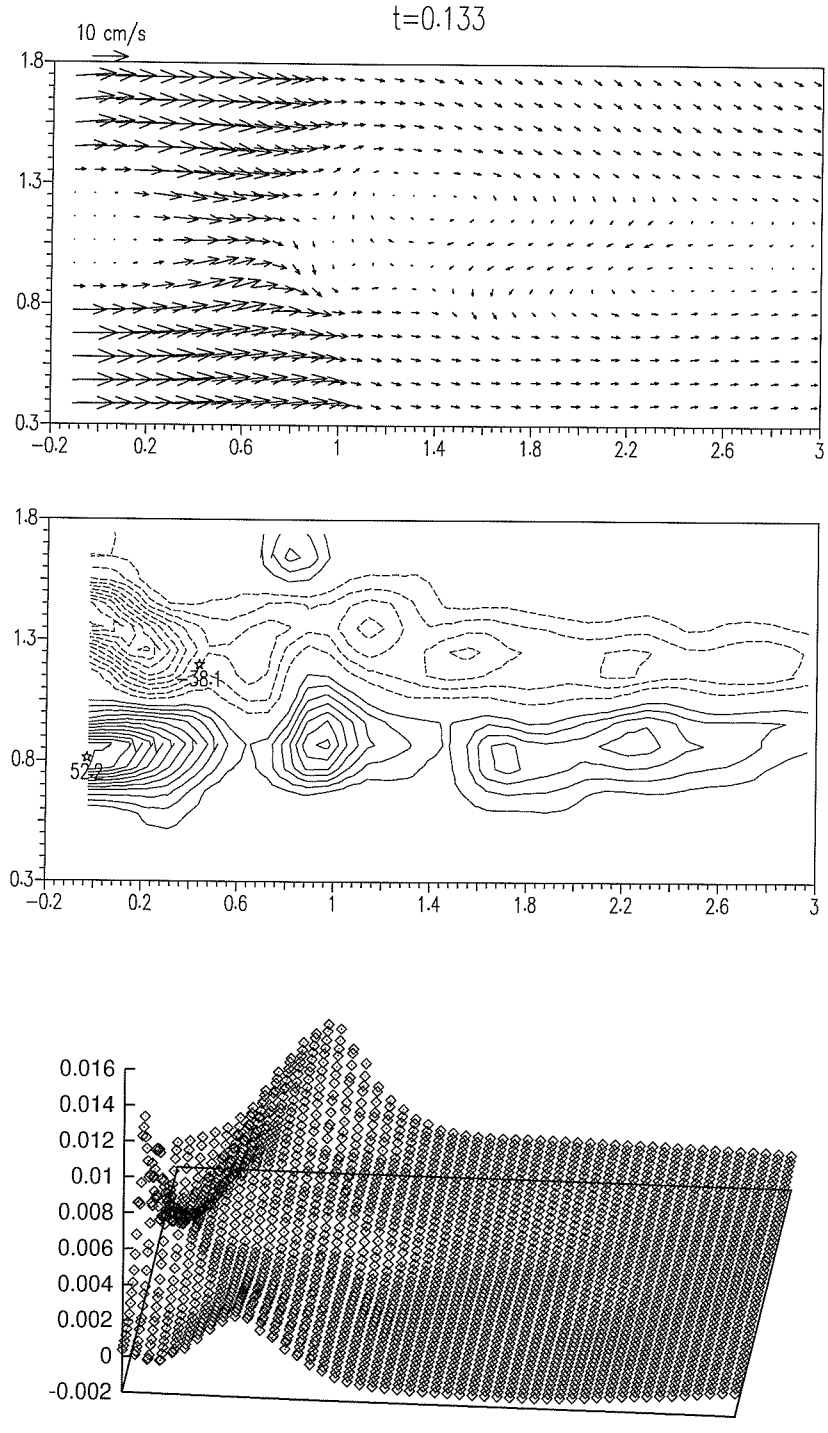

Figure 4.24: continued.

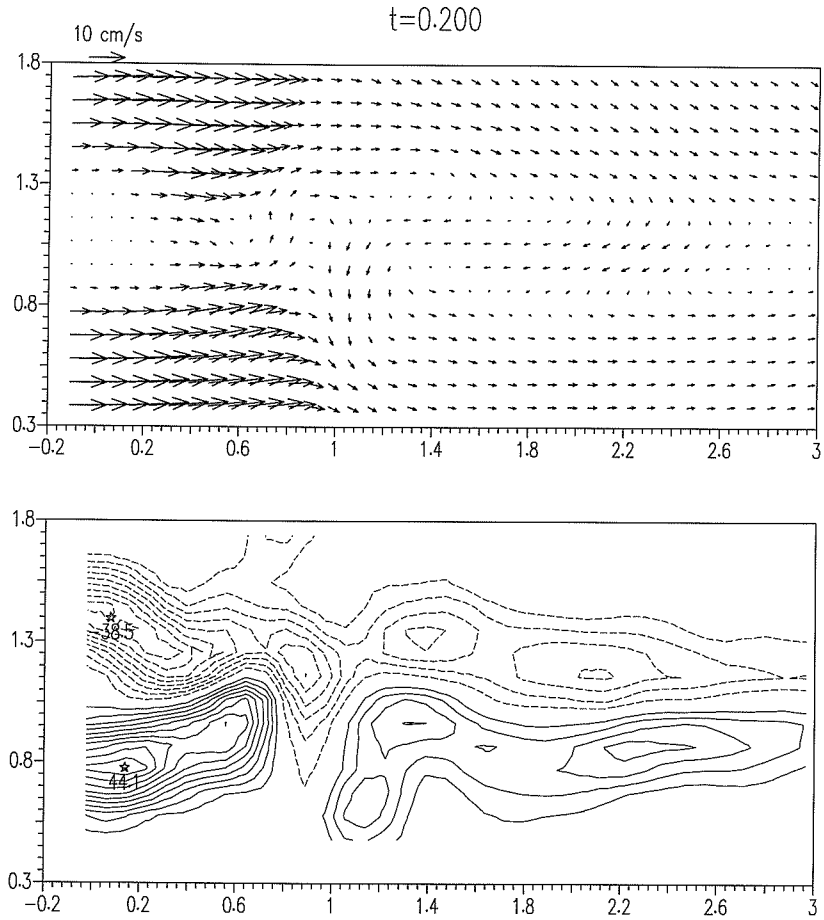

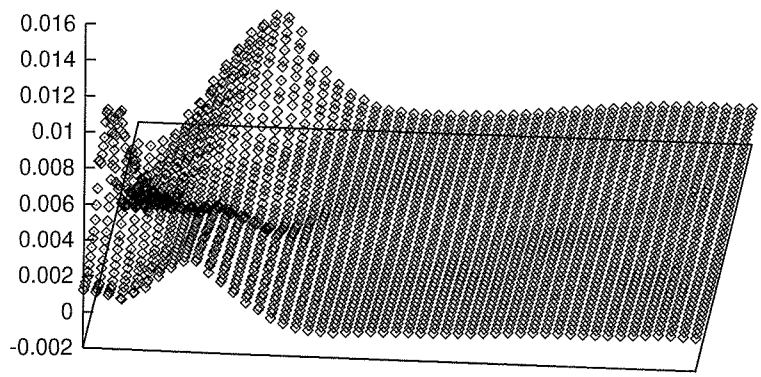

Figure 4.24: continued.

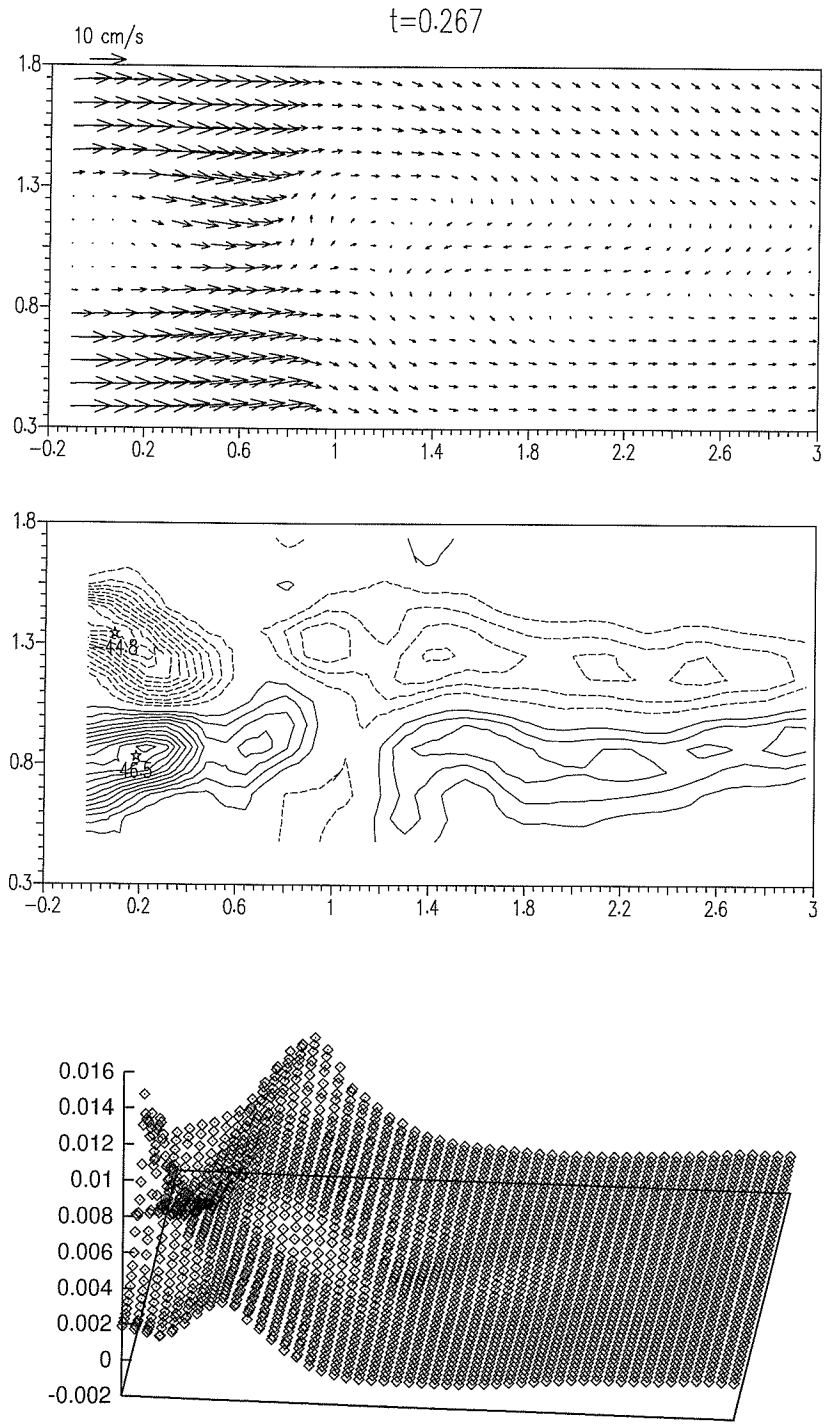

Figure 4.24: continued.

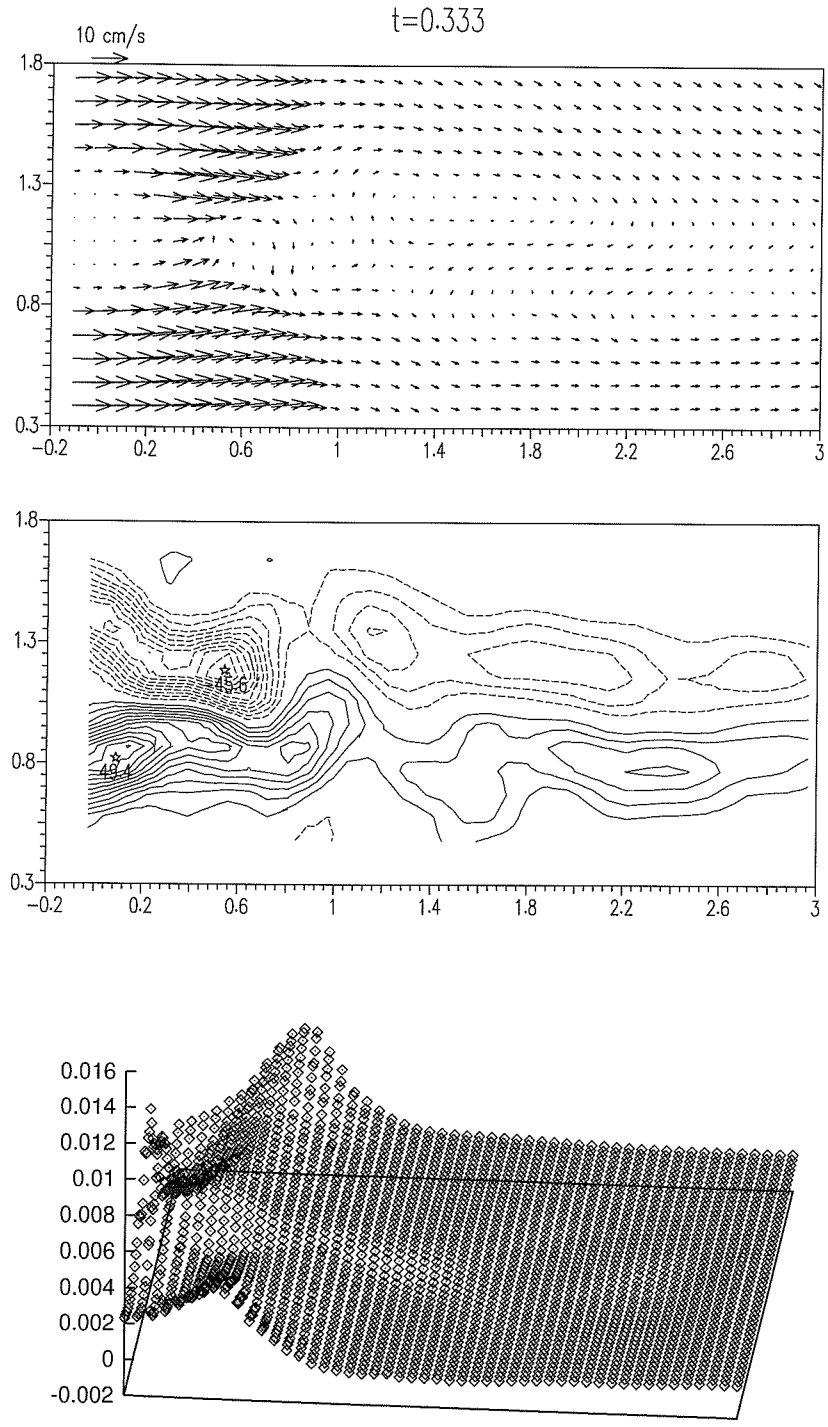

Figure 4.24: continued.

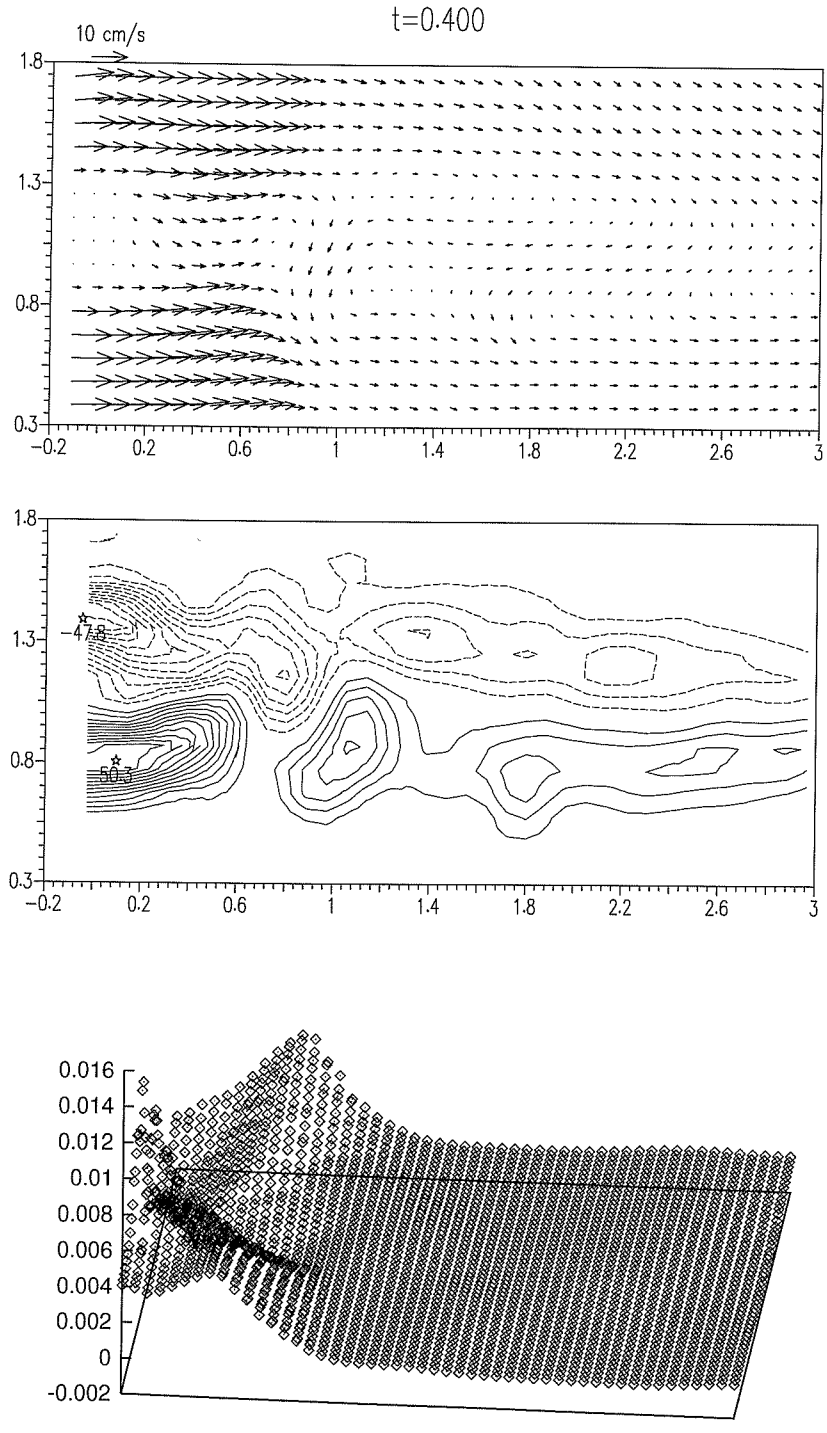

Figure 4.24: continued.

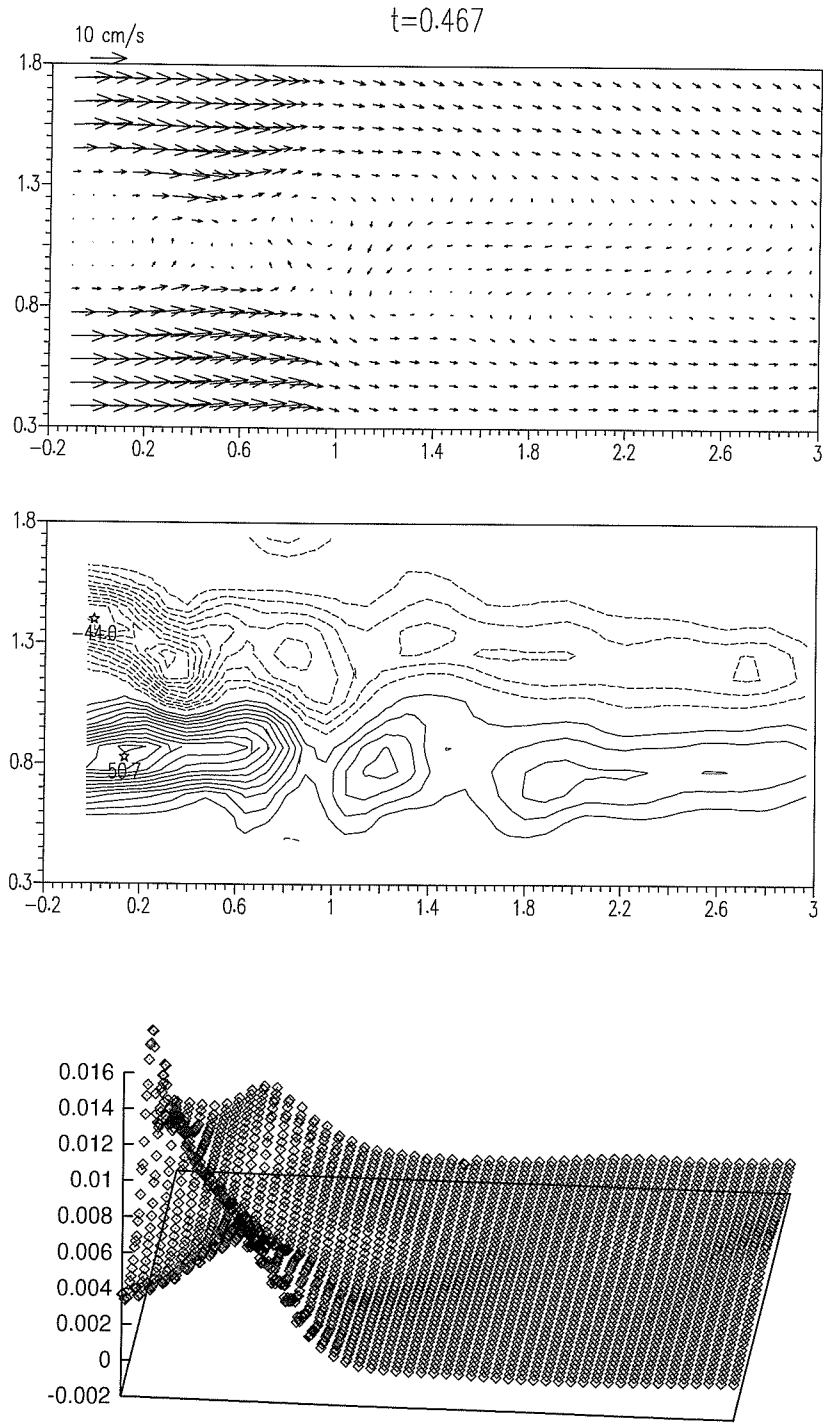

Figure 4.24: continued.

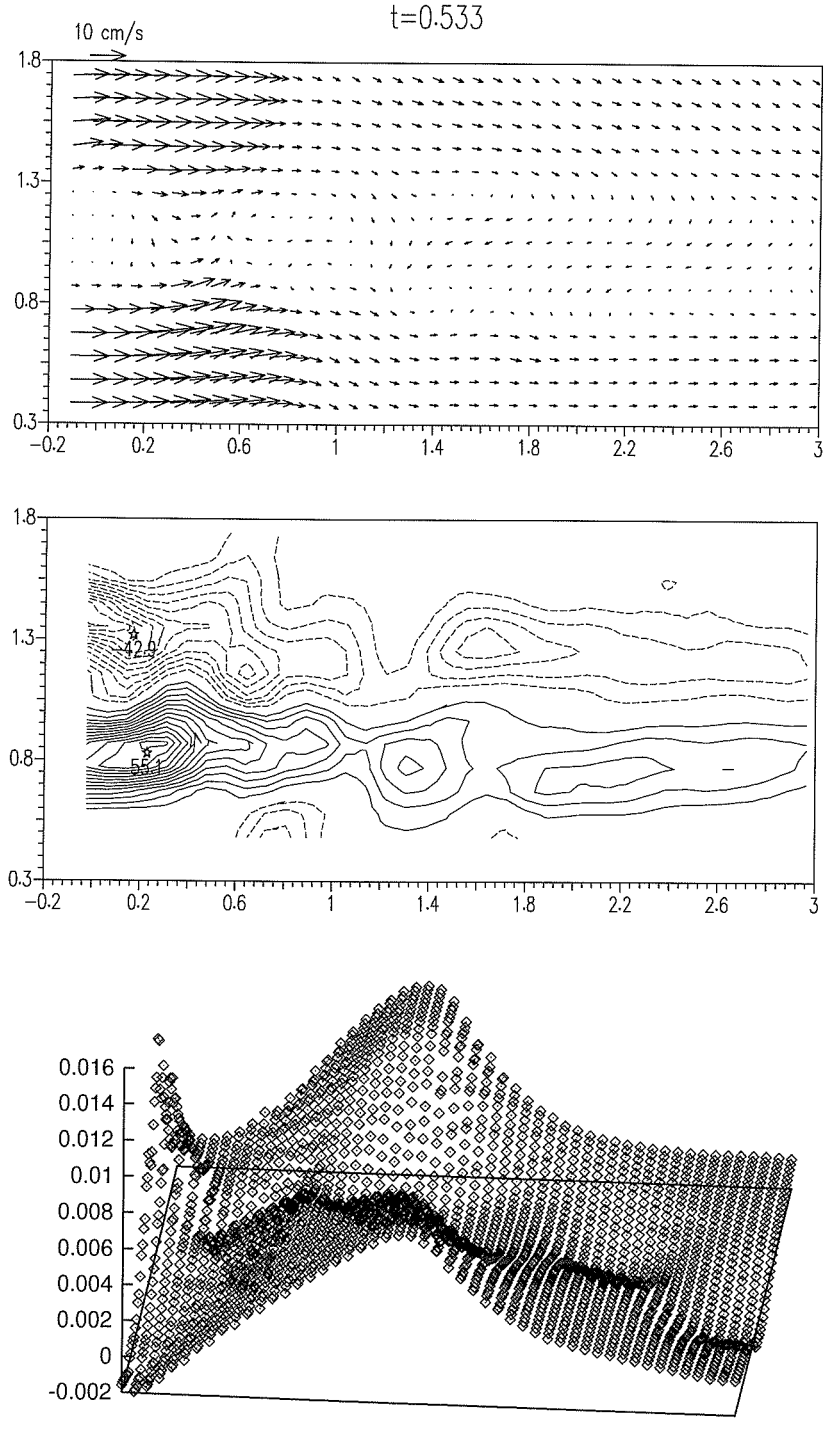

Figure 4.24: continued.

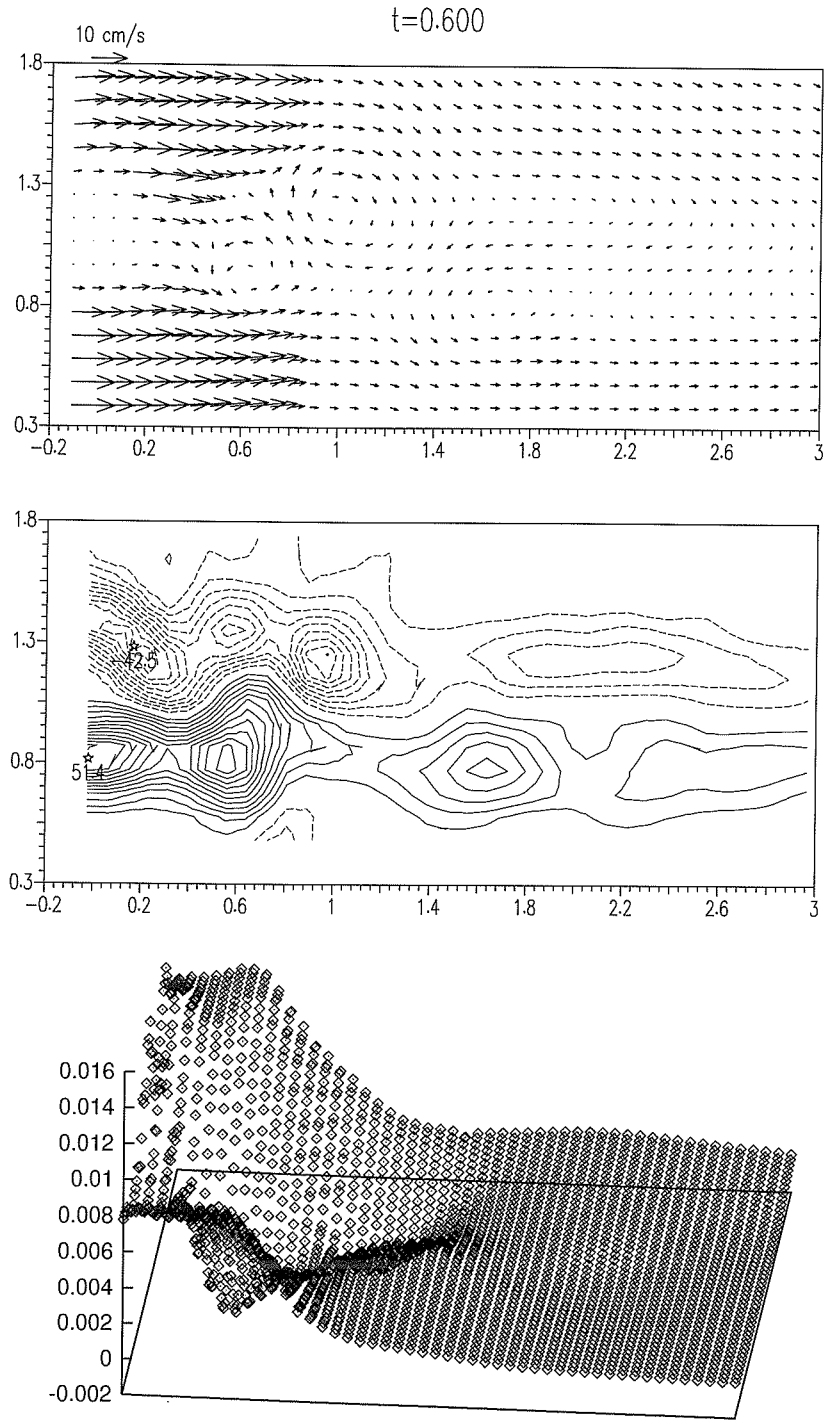

Figure 4.24: continued.

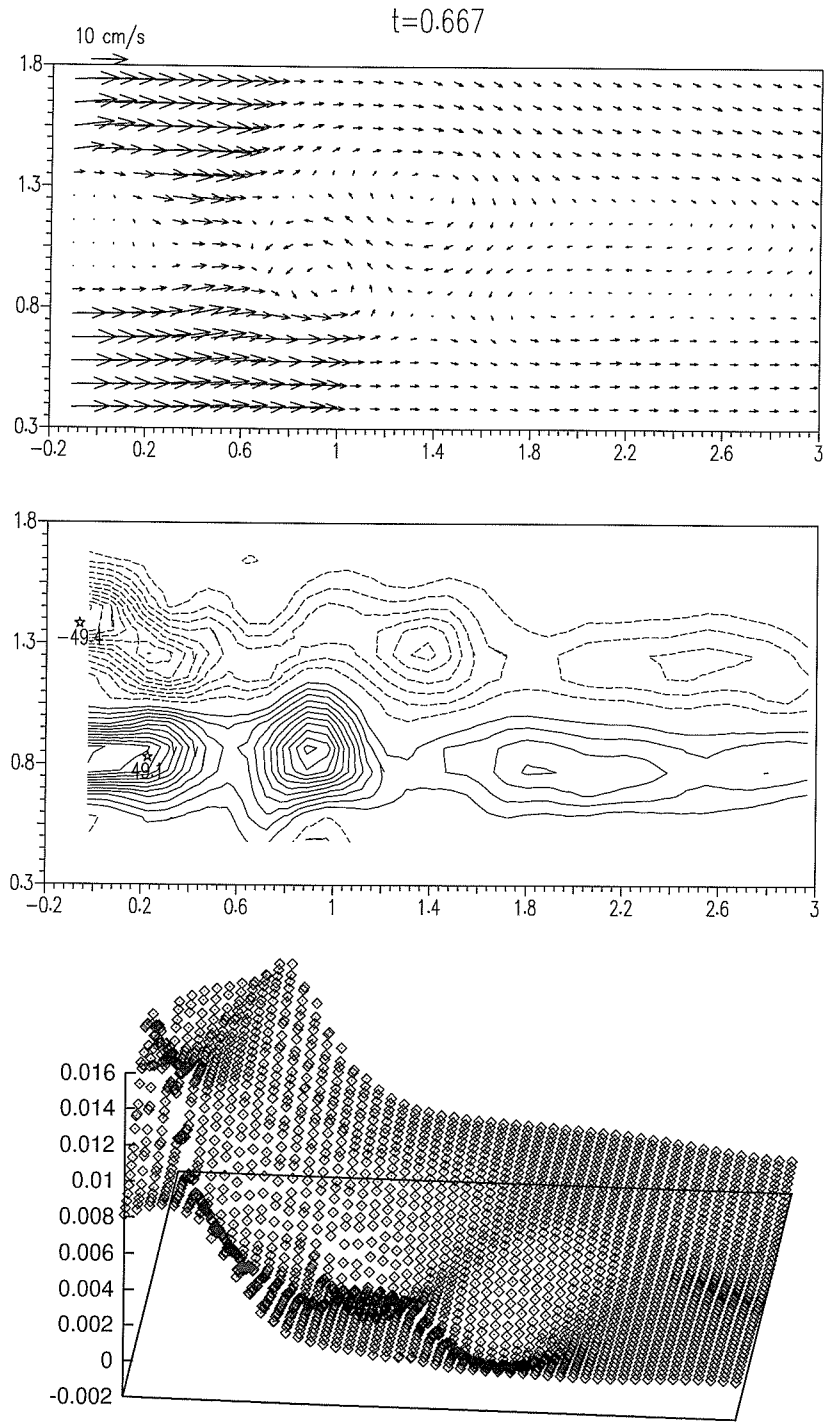

Figure 4.24: continued.

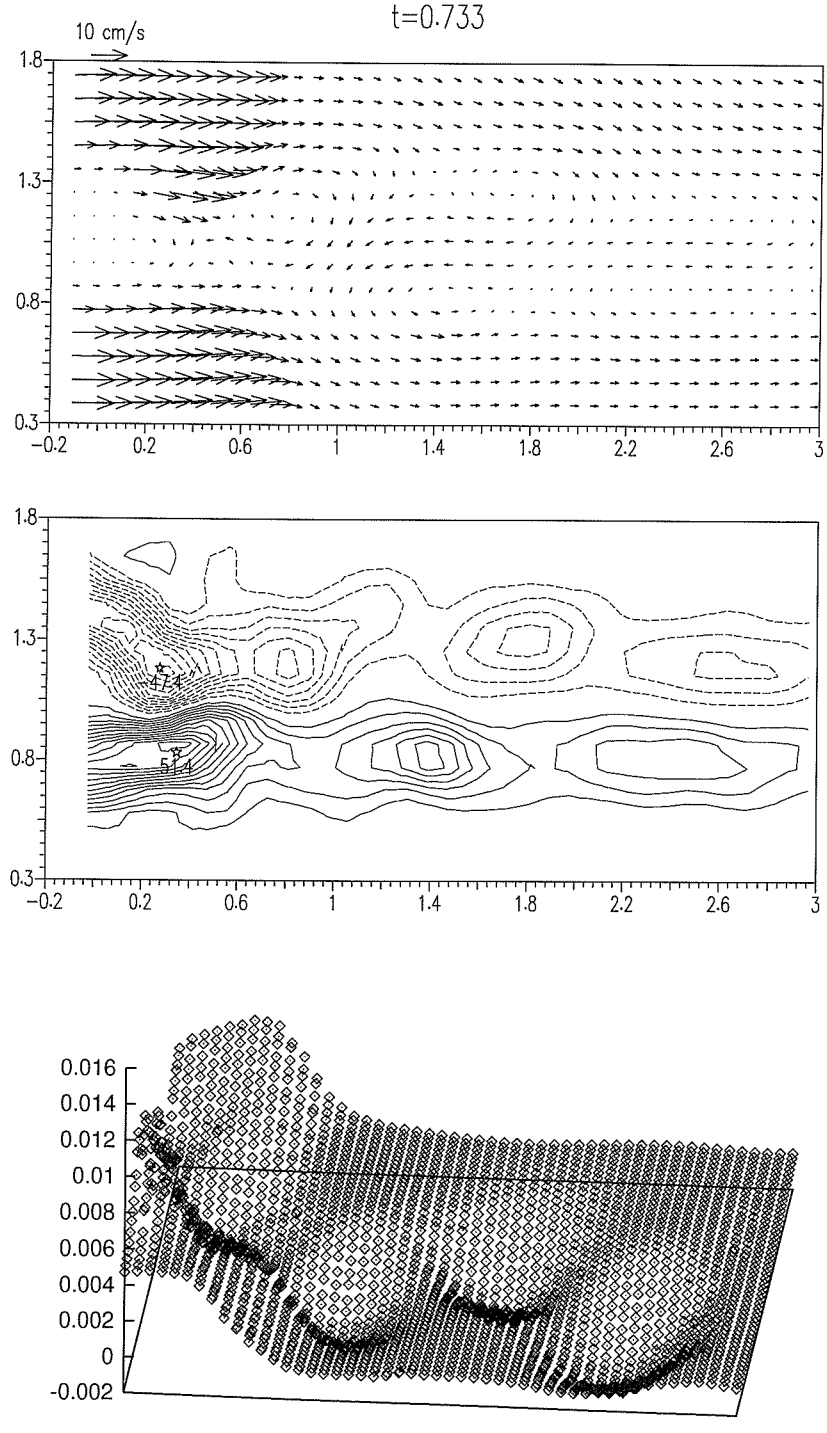

Figure 4.24 continued.

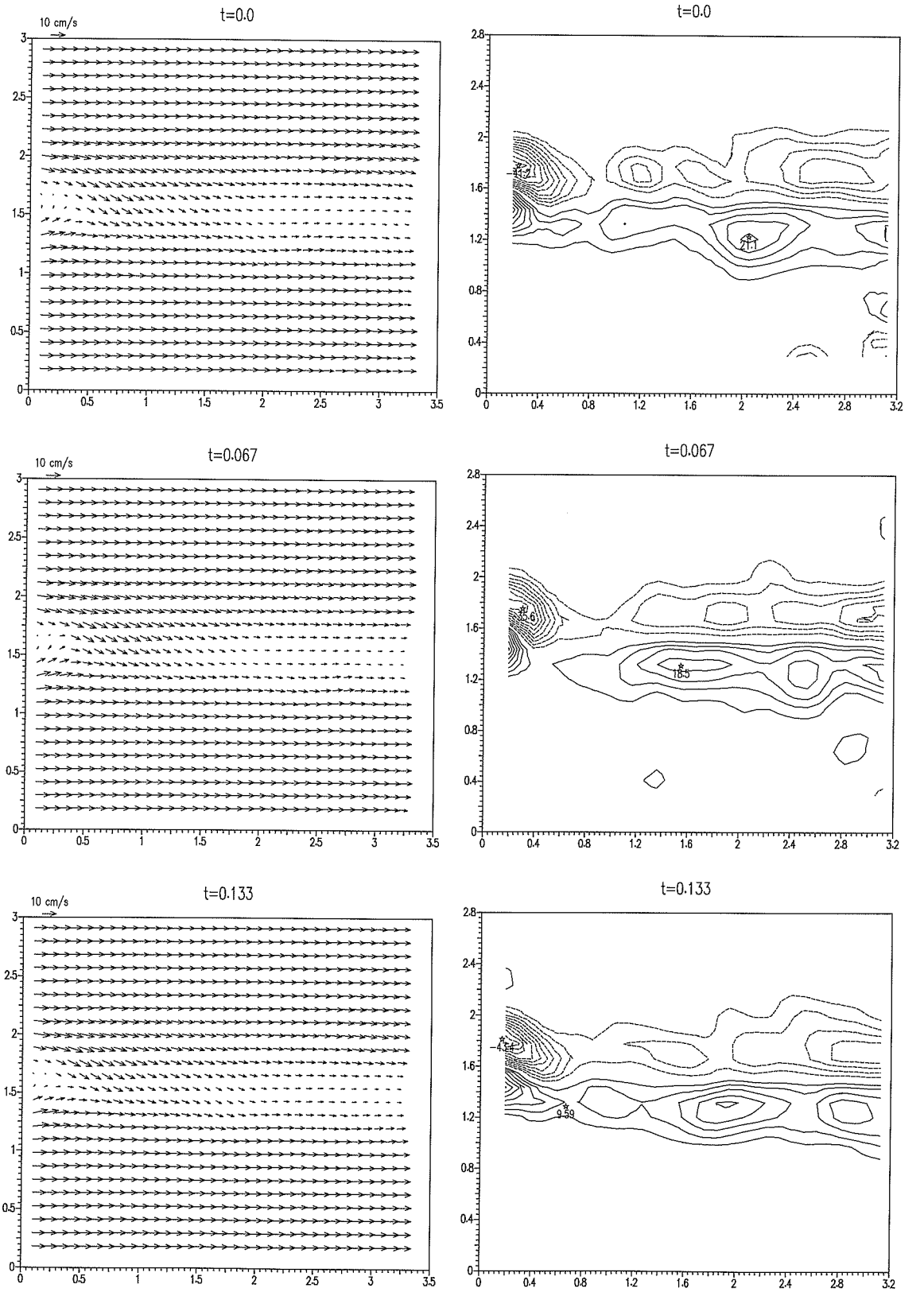

Figure 4.25: Sequence of velocity/vorticity (4,8,12...1/s) plots where surface-parallel cut at 0.55 cm below the free surface.

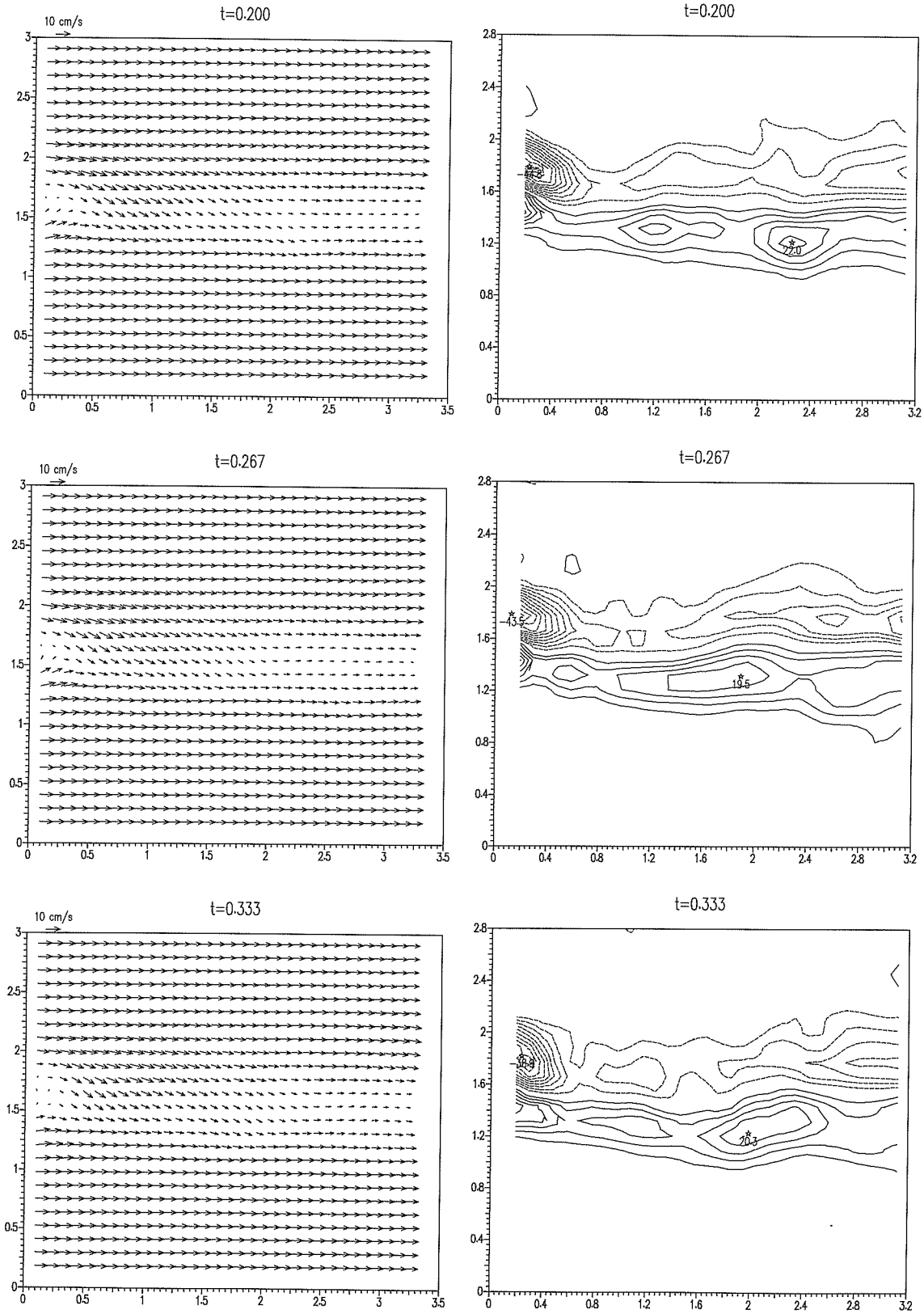

Figure 4.25: continued.

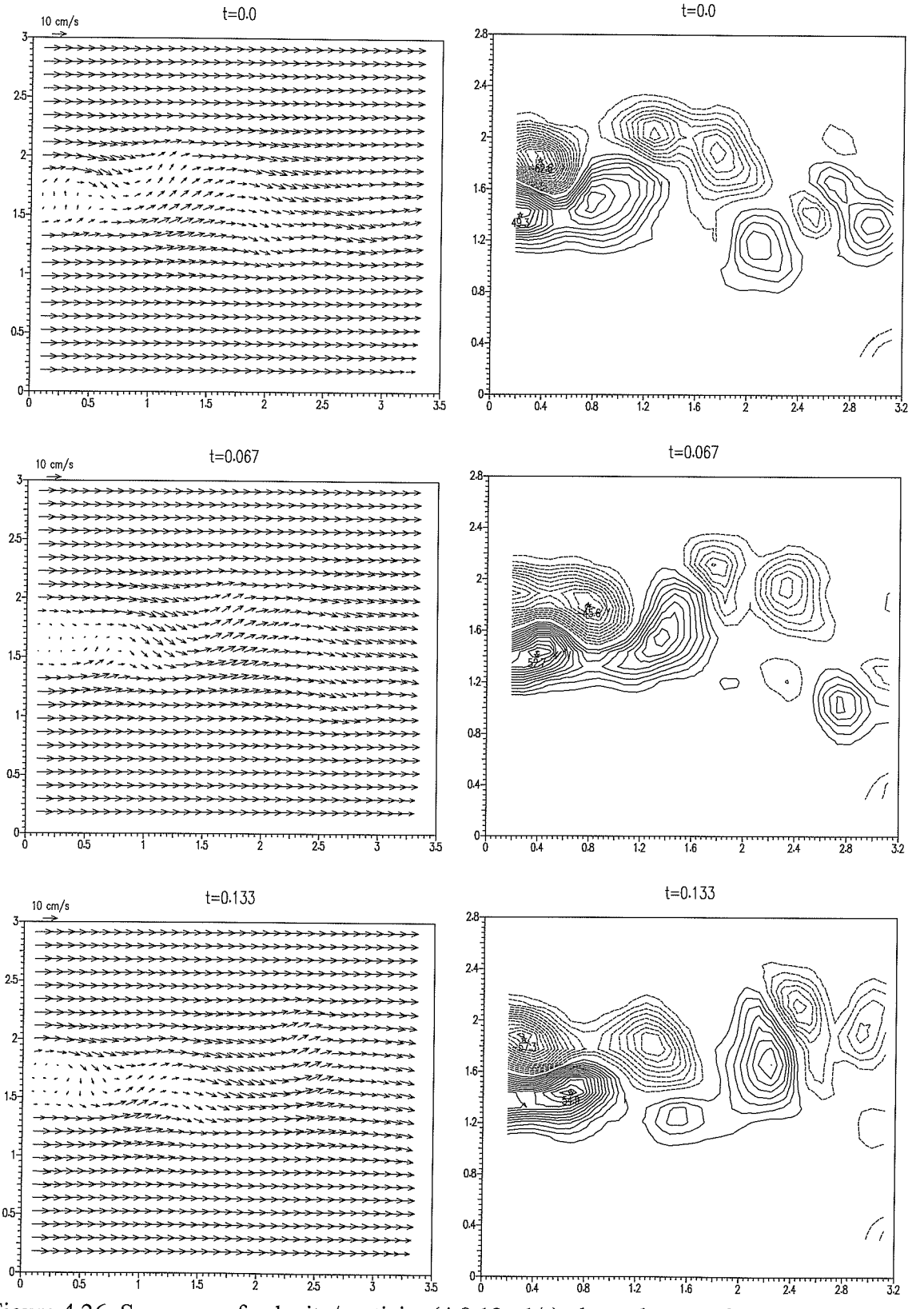

Figure 4.26: Sequence of velocity/vorticity (4,8,12...1/s) plots where surface-parallel cut at 1.10 cm below the free surface.

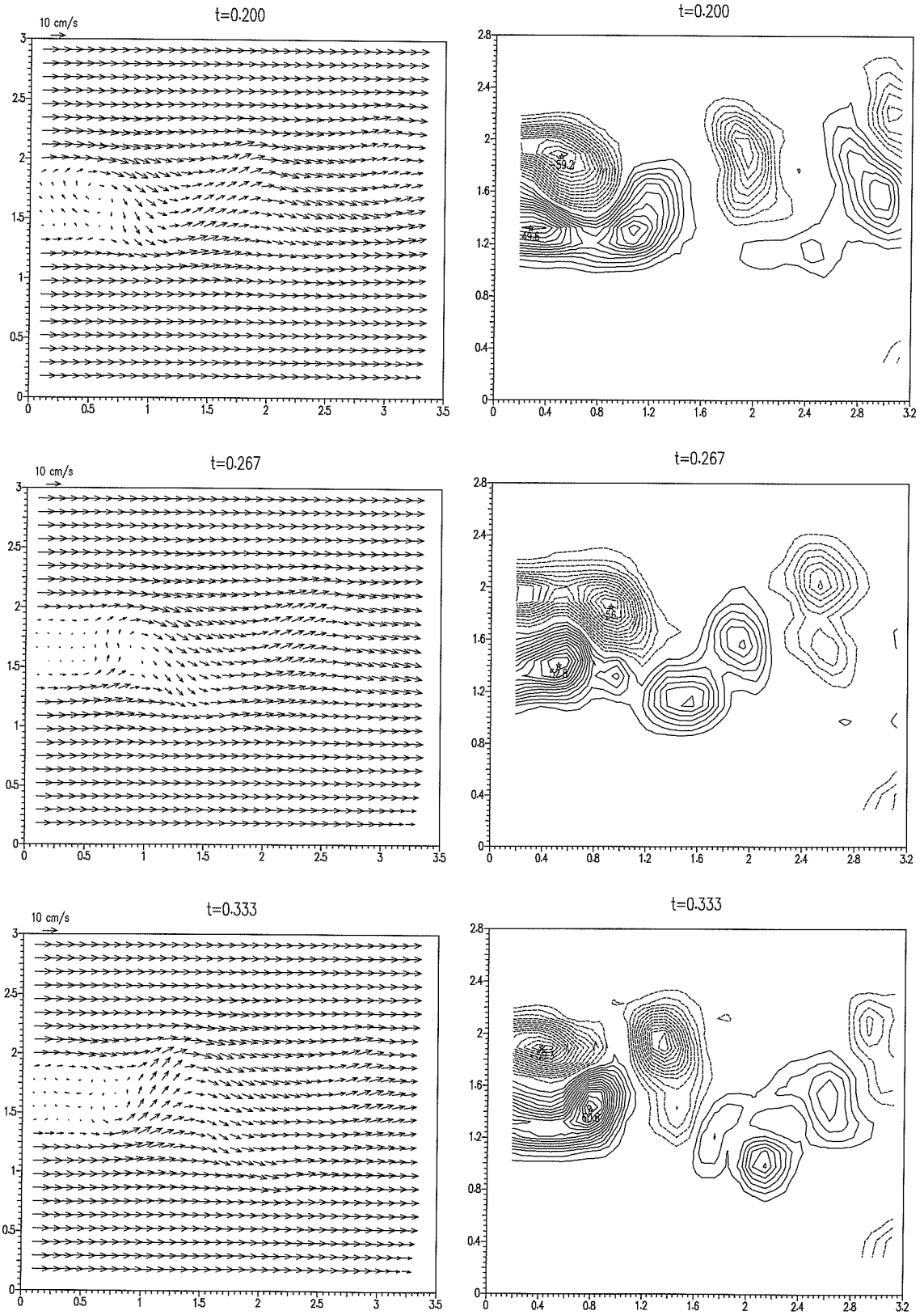

Figure 4.26: continued.

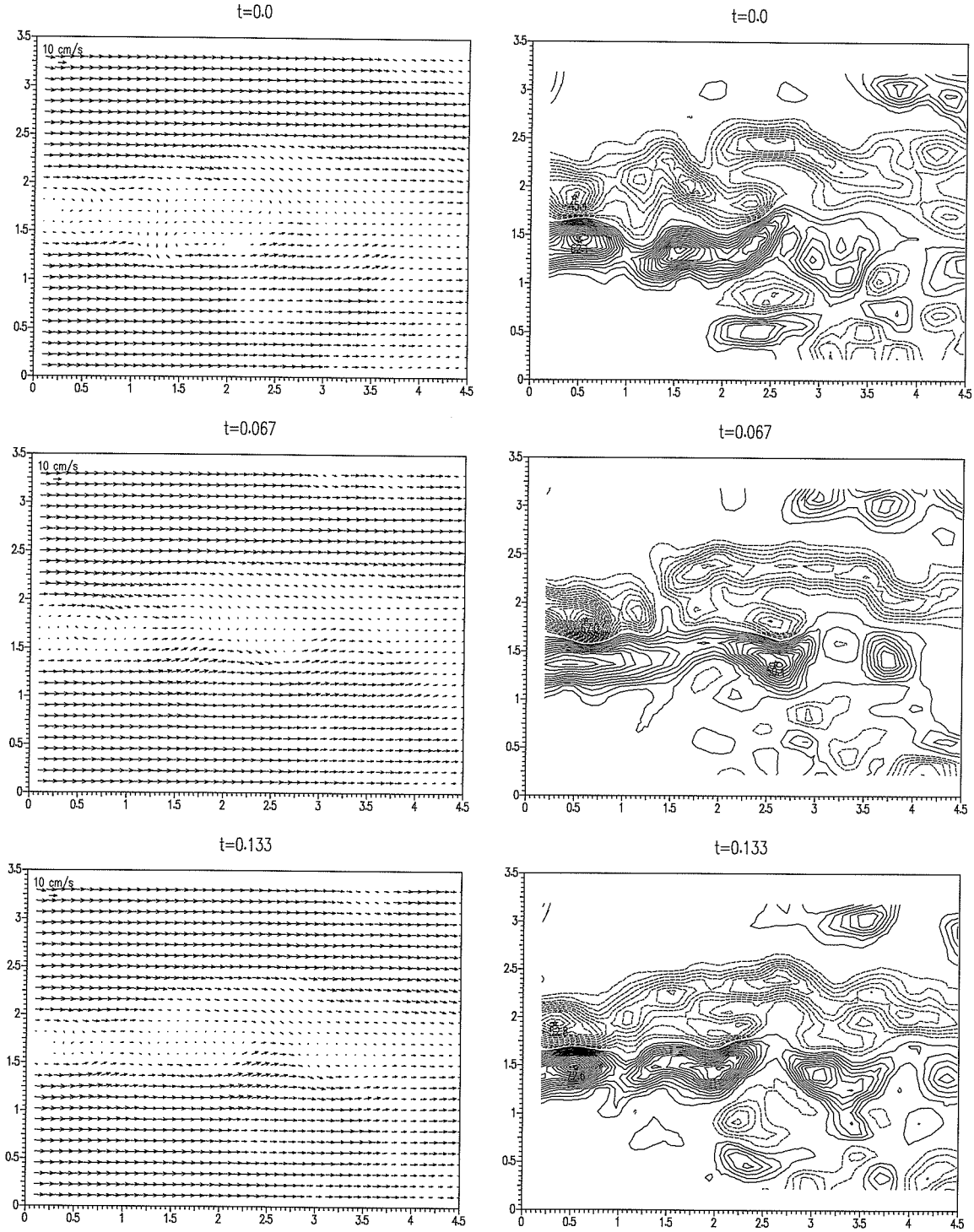

Figure 4.27: Sequence of velocity/vorticity (4,8,12...1/s) plots (Re=410) at the free surface in the case where the cylinder is contaminated and shedding surfactants into the wake.

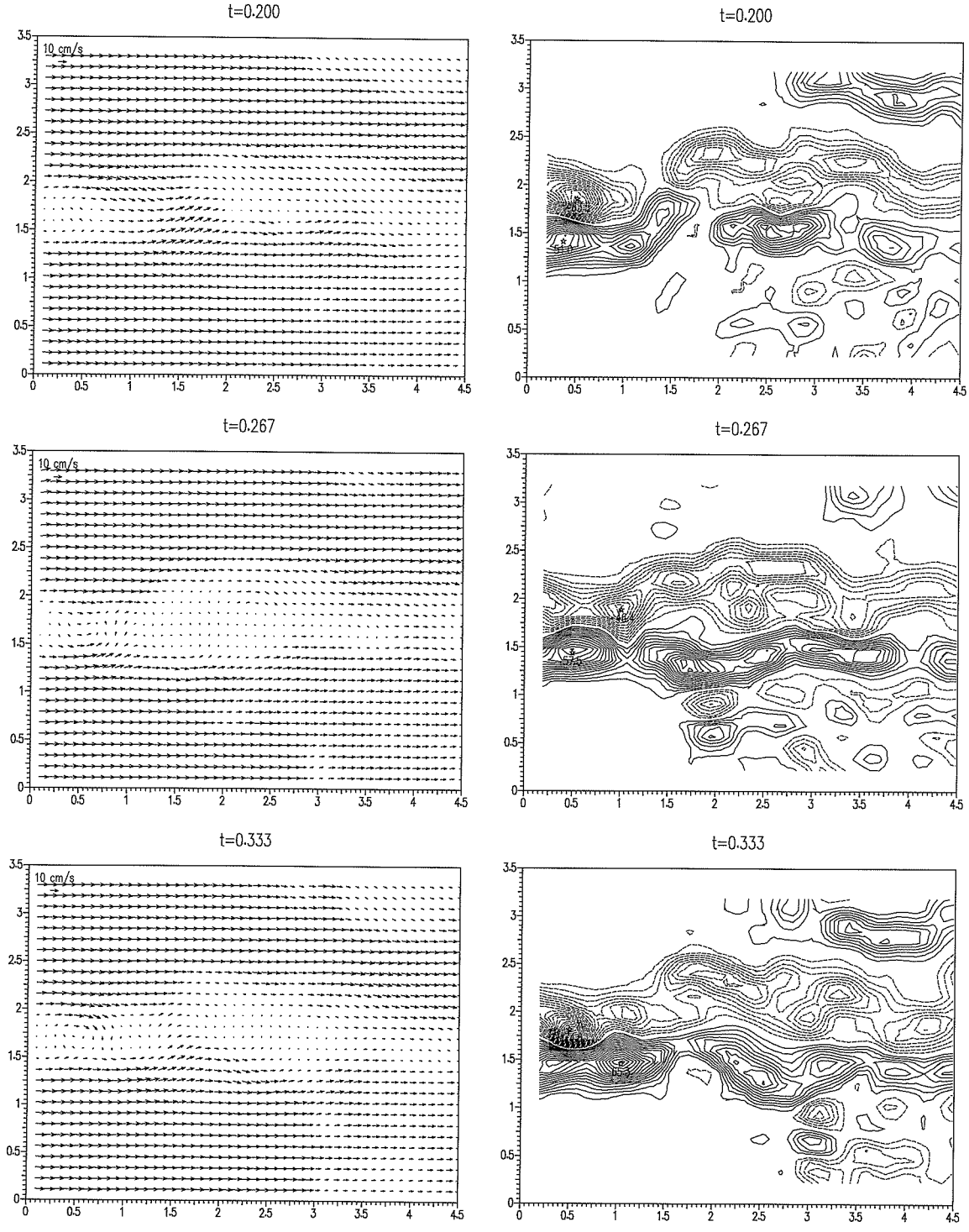

Figure 4.27: continued.

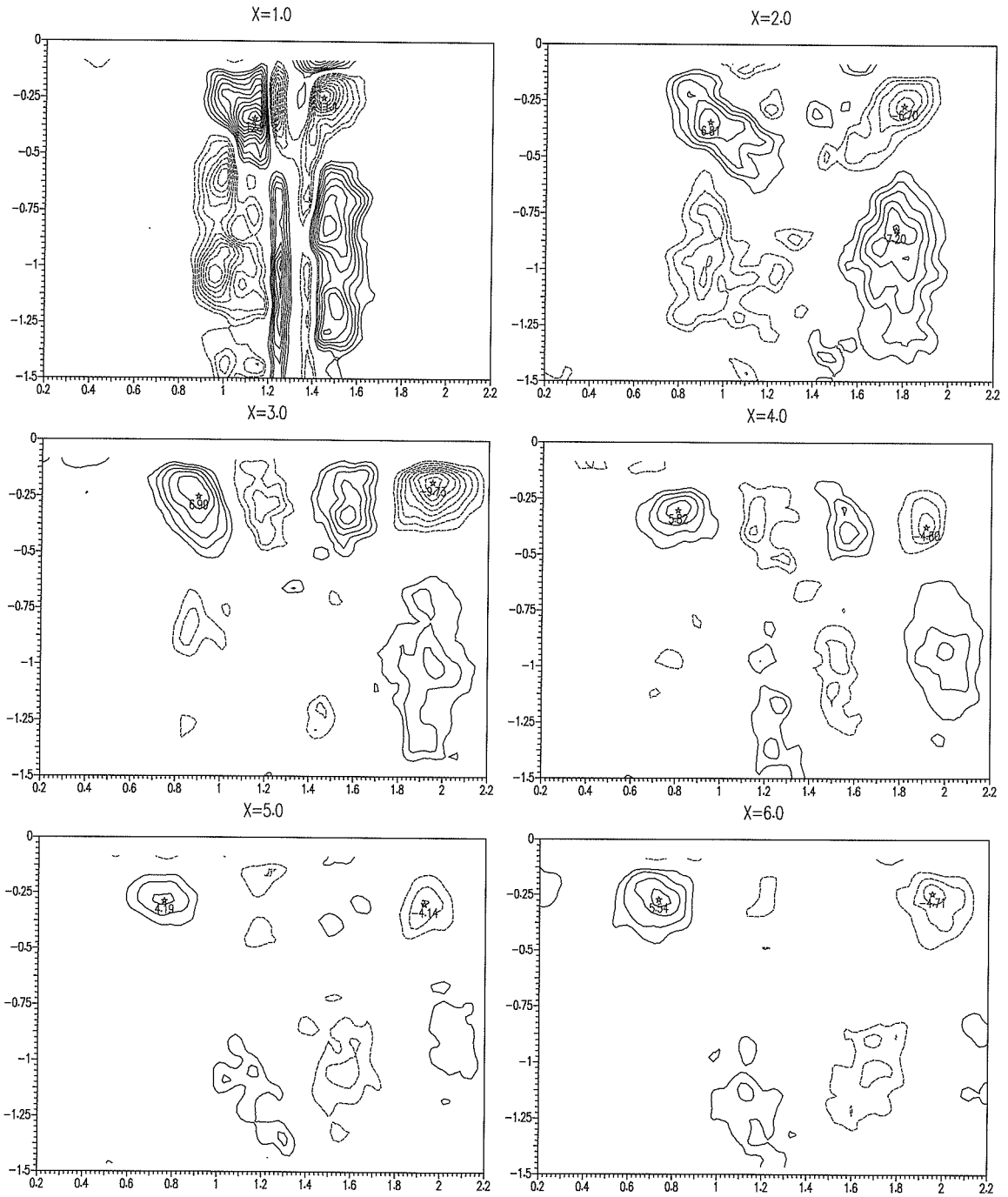

Figure 4.28: Six different downstream distance (X in cm downstream of cylinder) vorticity (contour levels 2,3,4...1/s) plots each averaged over 500 velocity files for Re=410 and a clean free surface.

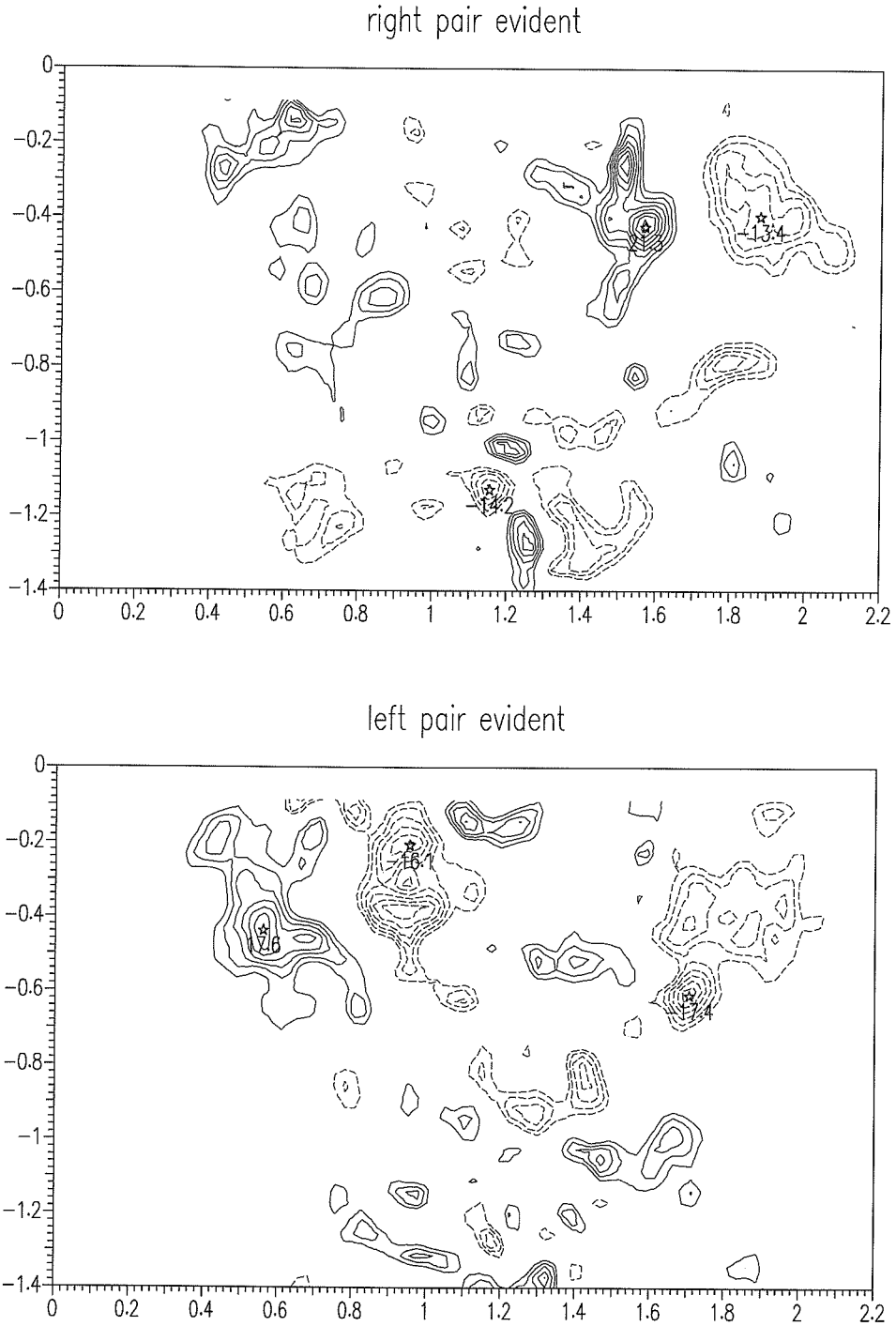

Figure 4.29: Two vorticity (6,8,10...1/s) plots averaged for 10 velocity files located at X=4 cm downstream and Re=410 exhibiting the average of the vortex pair when on the right side and when on the left side of the same zigzag pair.

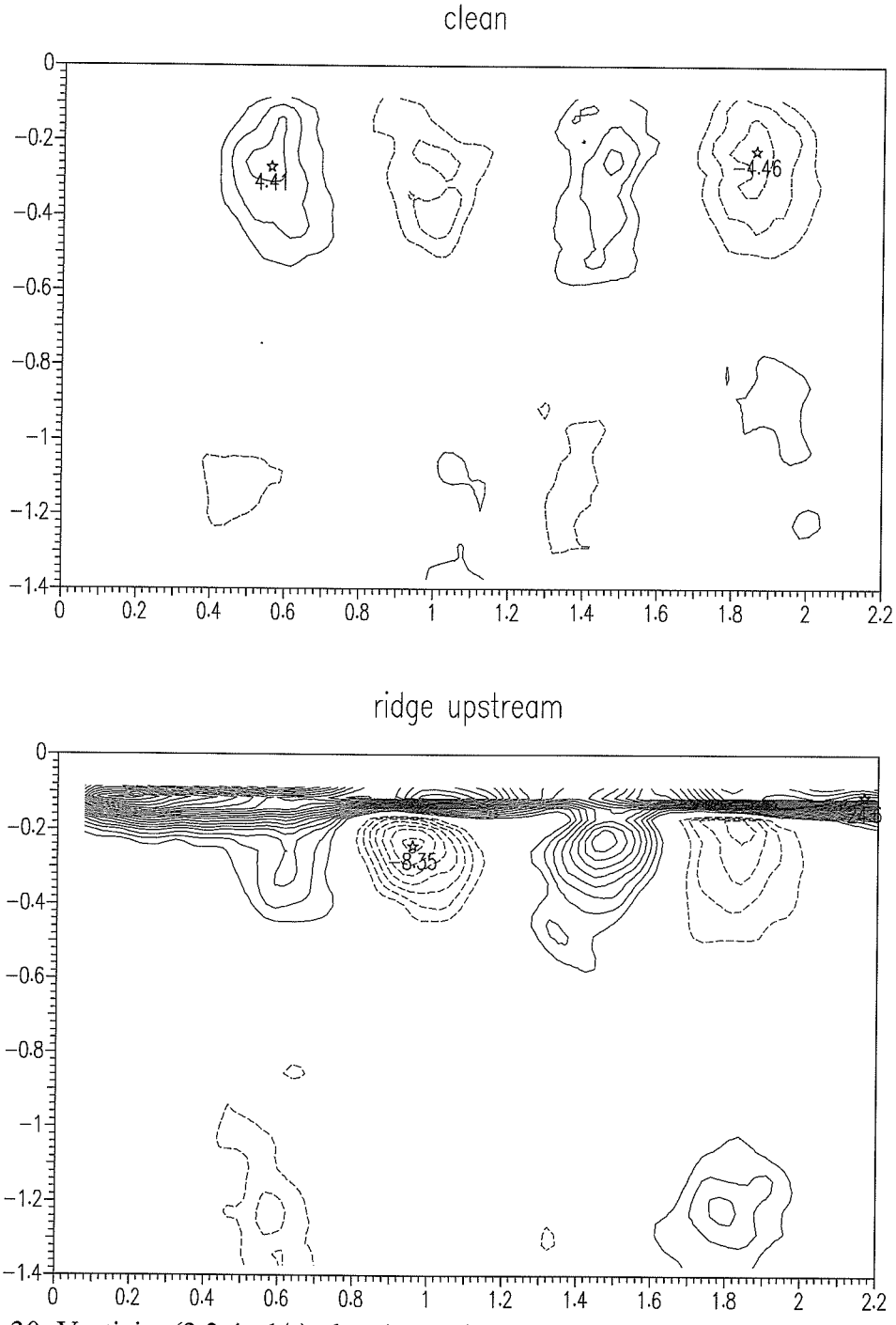

Figure 4.30: Vorticity (2,3,4...1/s) plots located at X=4 cm and Re=350 for the clean case and when the ridge is located upstream 2 cm of the cross-section and unattached to the cylinder.

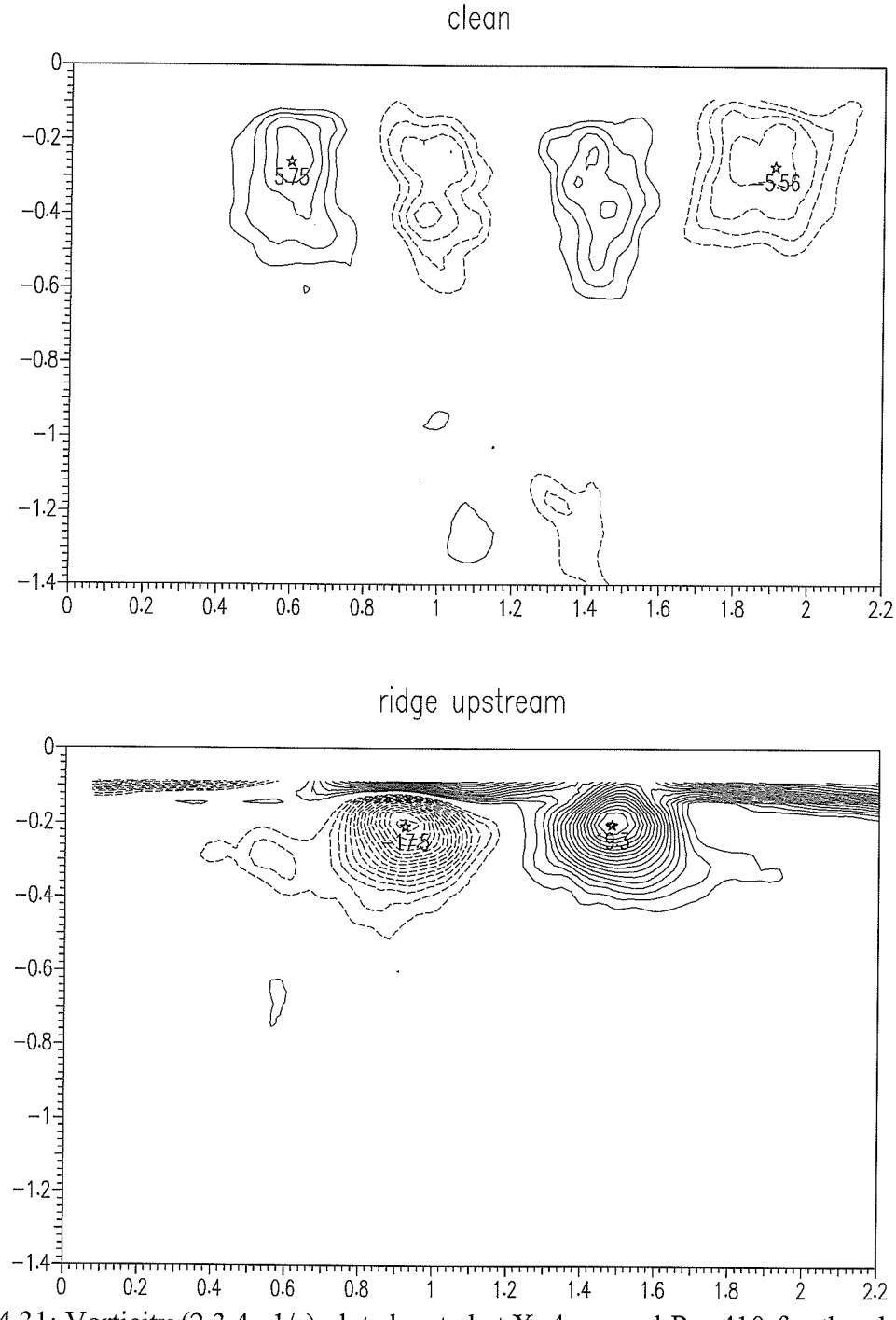

Figure 4.31: Vorticity (2,3,4...1/s) plots located at X=4 cm and Re=410 for the clean case and when the ridge is located upstream 2 cm of the cross-section and unattached to the cylinder.

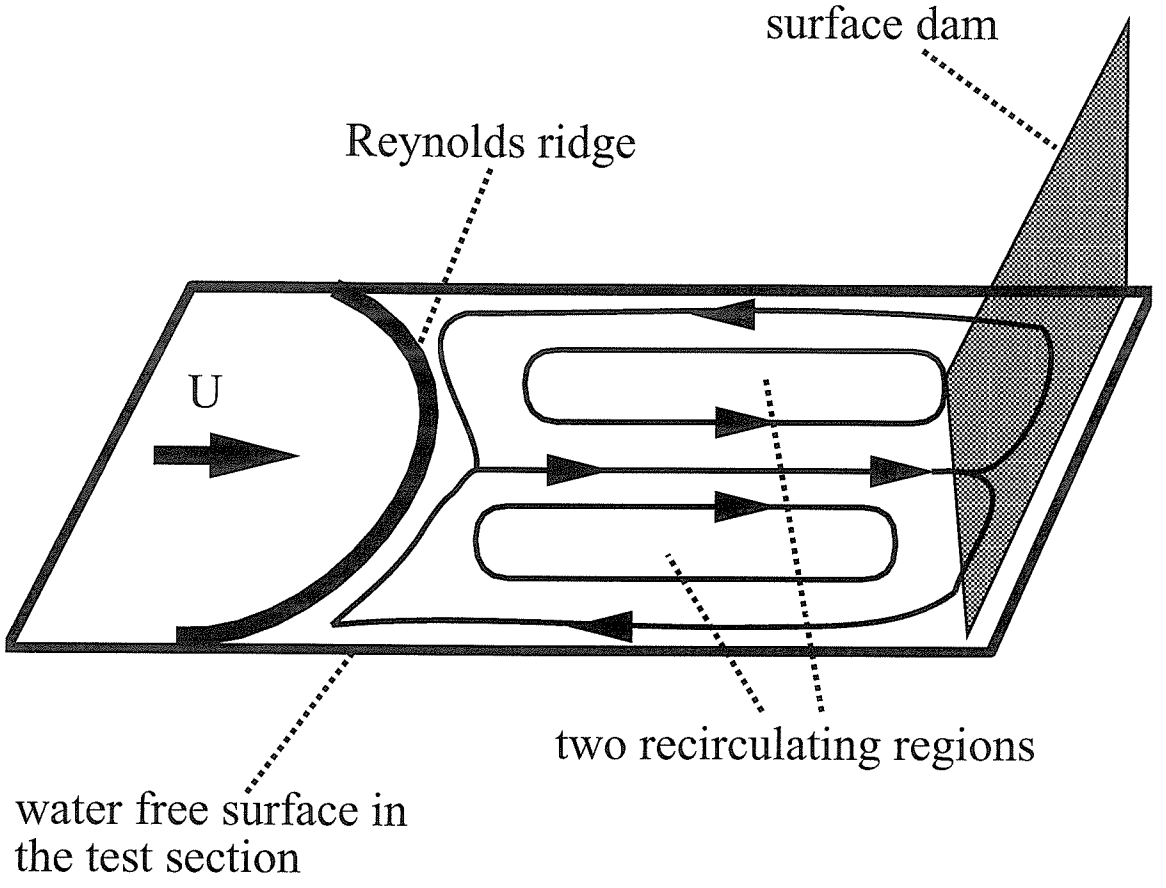

Figure 4.32: Schematic of monolayer flow observed in tunnel test section behind the Reynolds ridge.

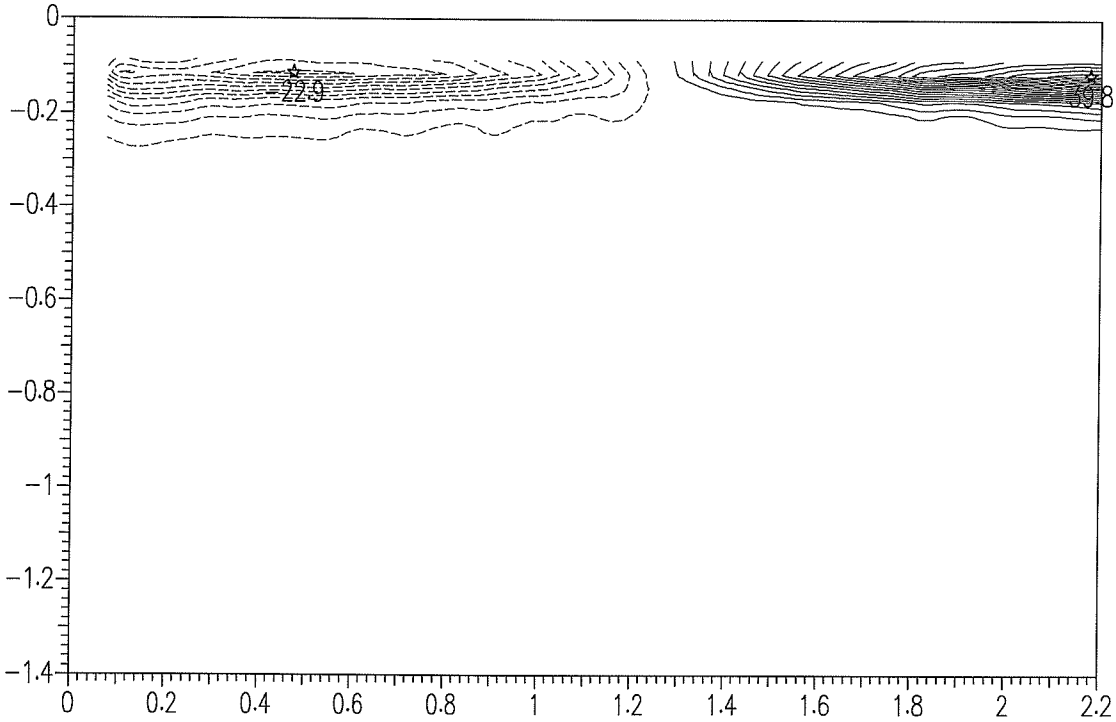

Figure 4.33: Vorticity (2,4,6...1/s) plot averaged for U=13 cm/s and ridge located 2 cm upstream of cross-section.

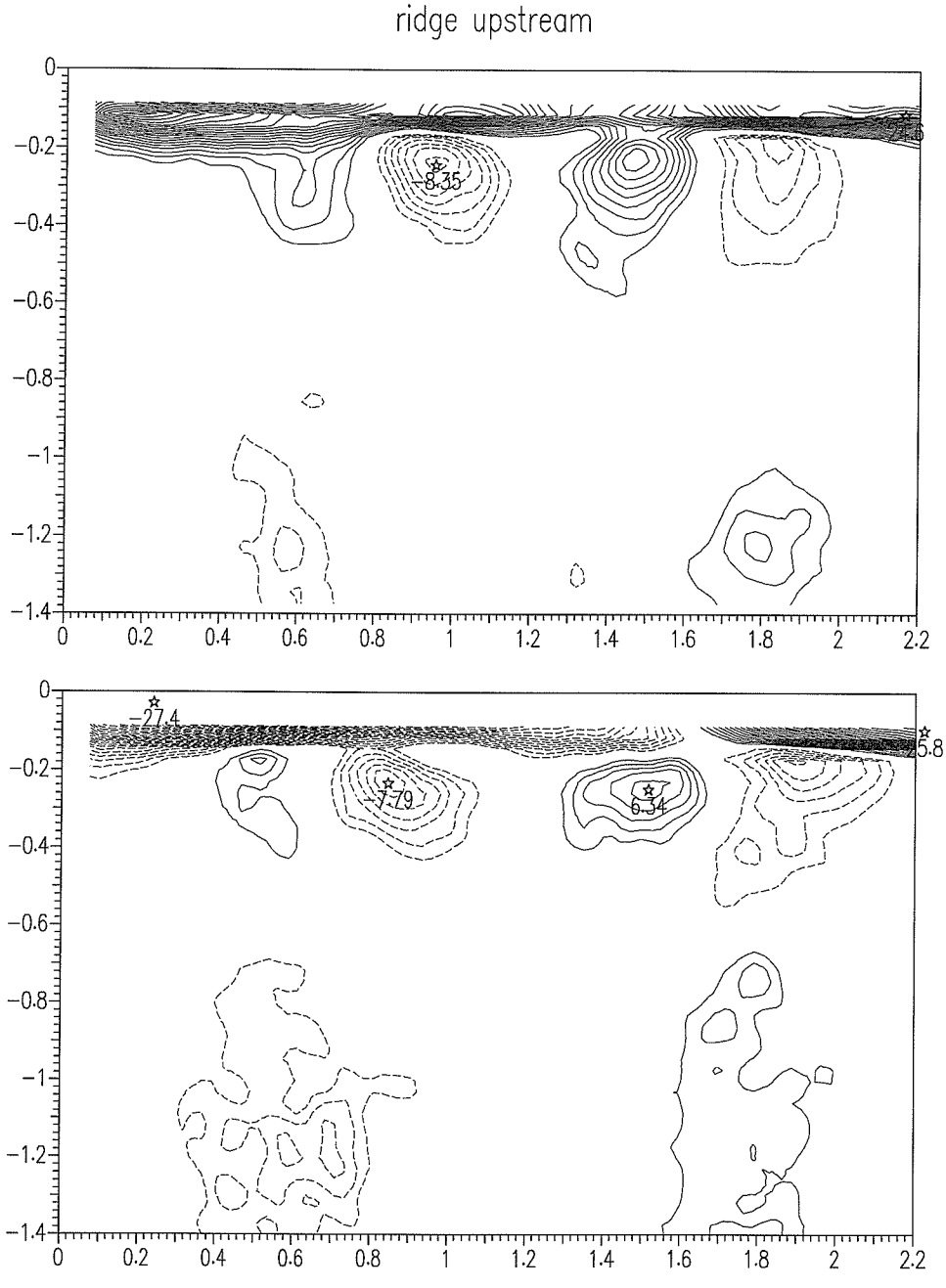

Figure 4.34: Two vorticity (2,3,4...1/s) plots of same case (Re=350 and X=4 cm and ridge located 2 cm upstream of cross-section) but different positioning of the cylinder with respect to the centerline of the tunnel.

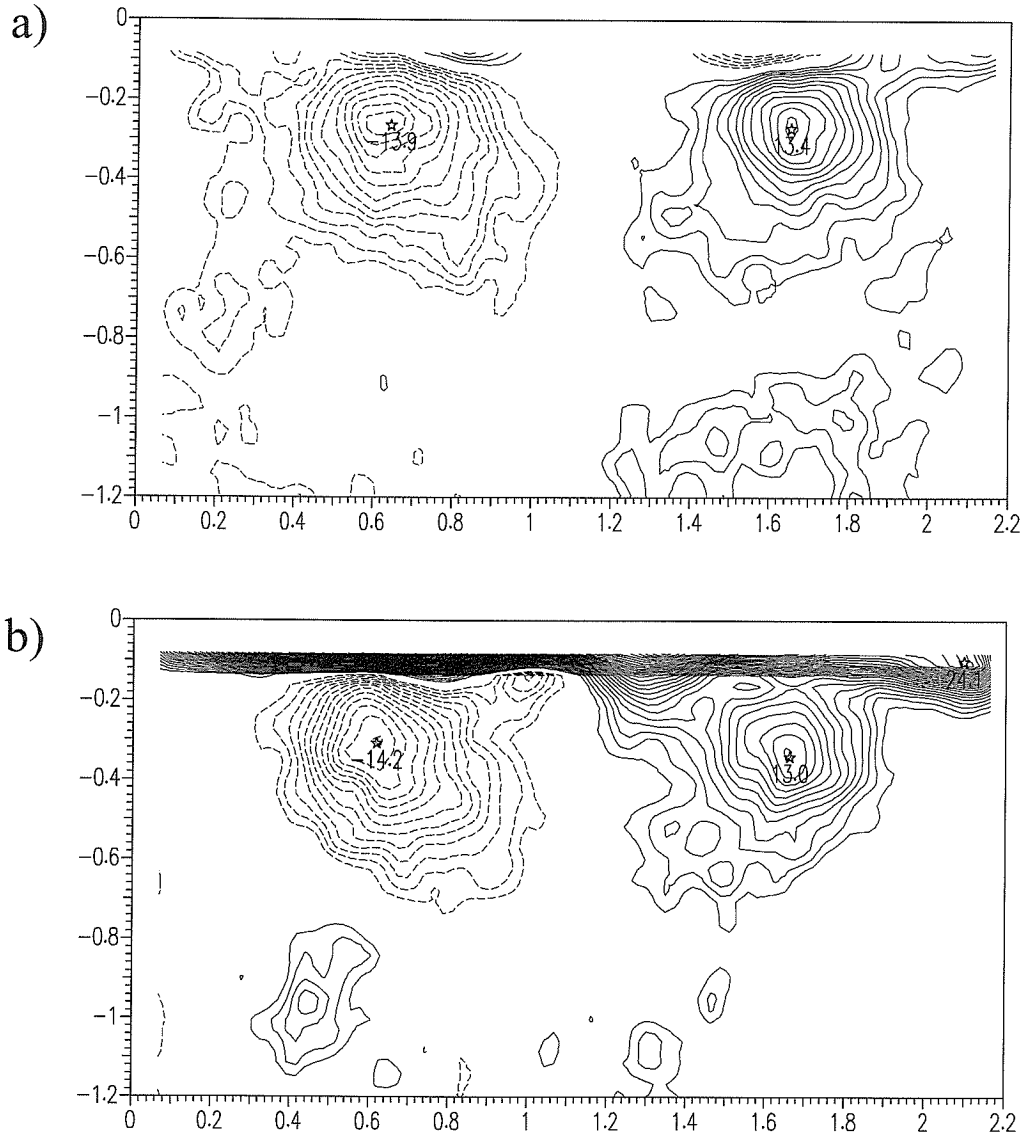

Figure 4.35: Vorticity (2,3,4...1/s) plots for Re=350 and the cylinder is contaminated where (a) ridge is downstream of cross-section and (b) upstream 2 cm of cross-section.

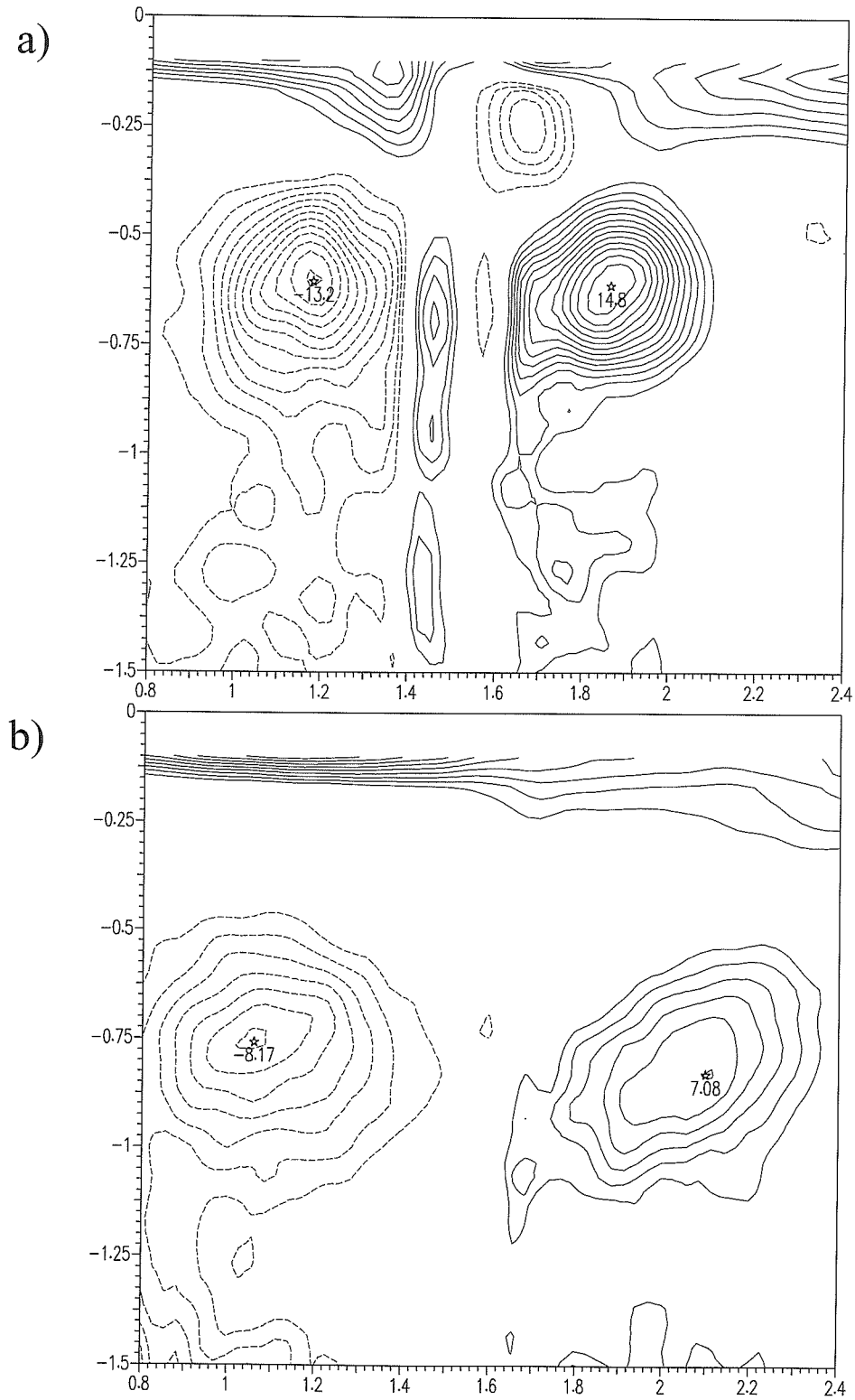

Figure 4.36: Vorticity contours at two downstream cross-sections (a) X=1.75 cm and (b) X=3.75 cm where Re=410 and wake contaminated (ridge 7 cm upstream of cylinder).

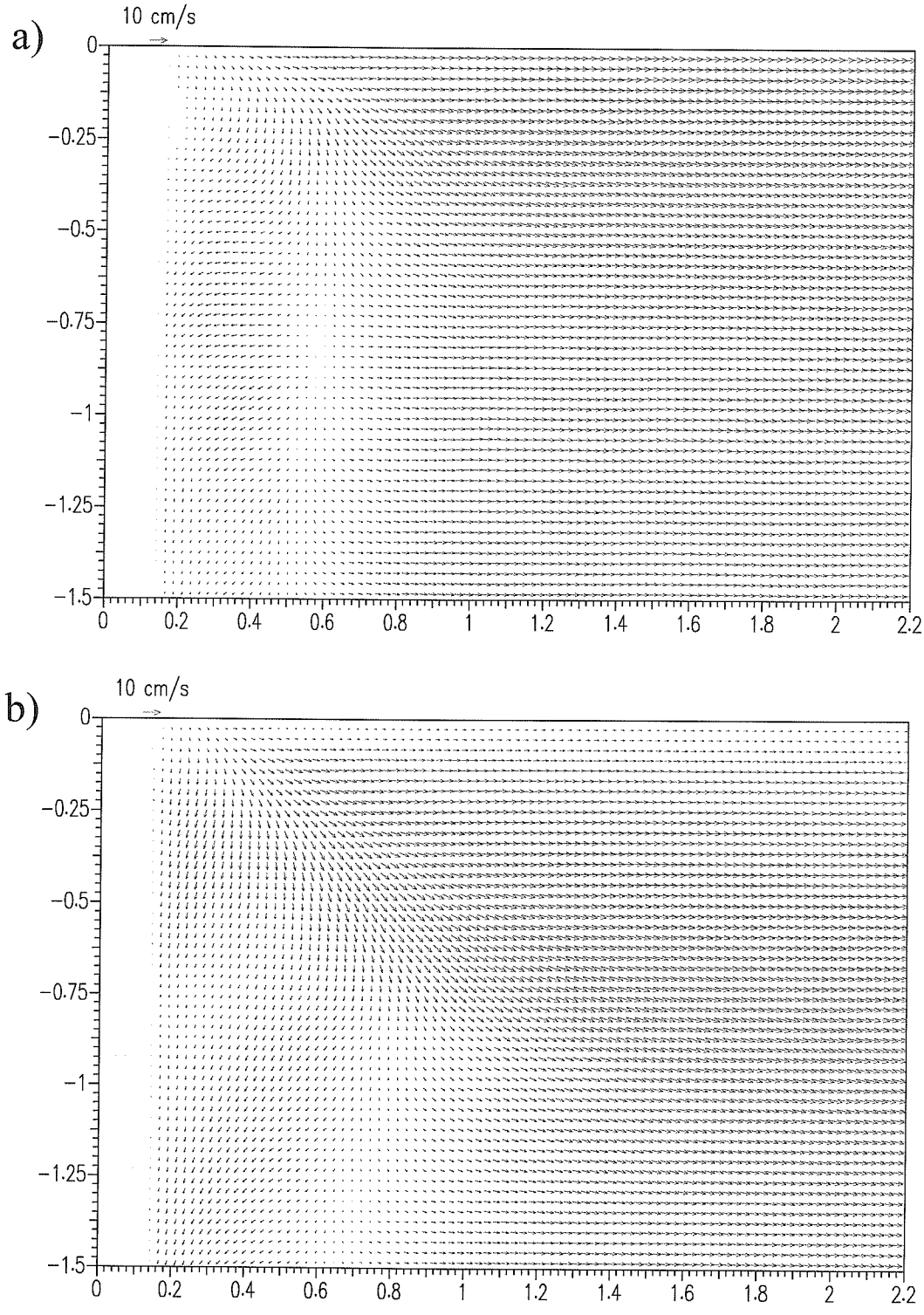

Figure 4.37: Velocity field for (a) clean case and (b) contaminated case (ridge 7 cm upstream of the cylinder) and Re=350 of the center cross-section.

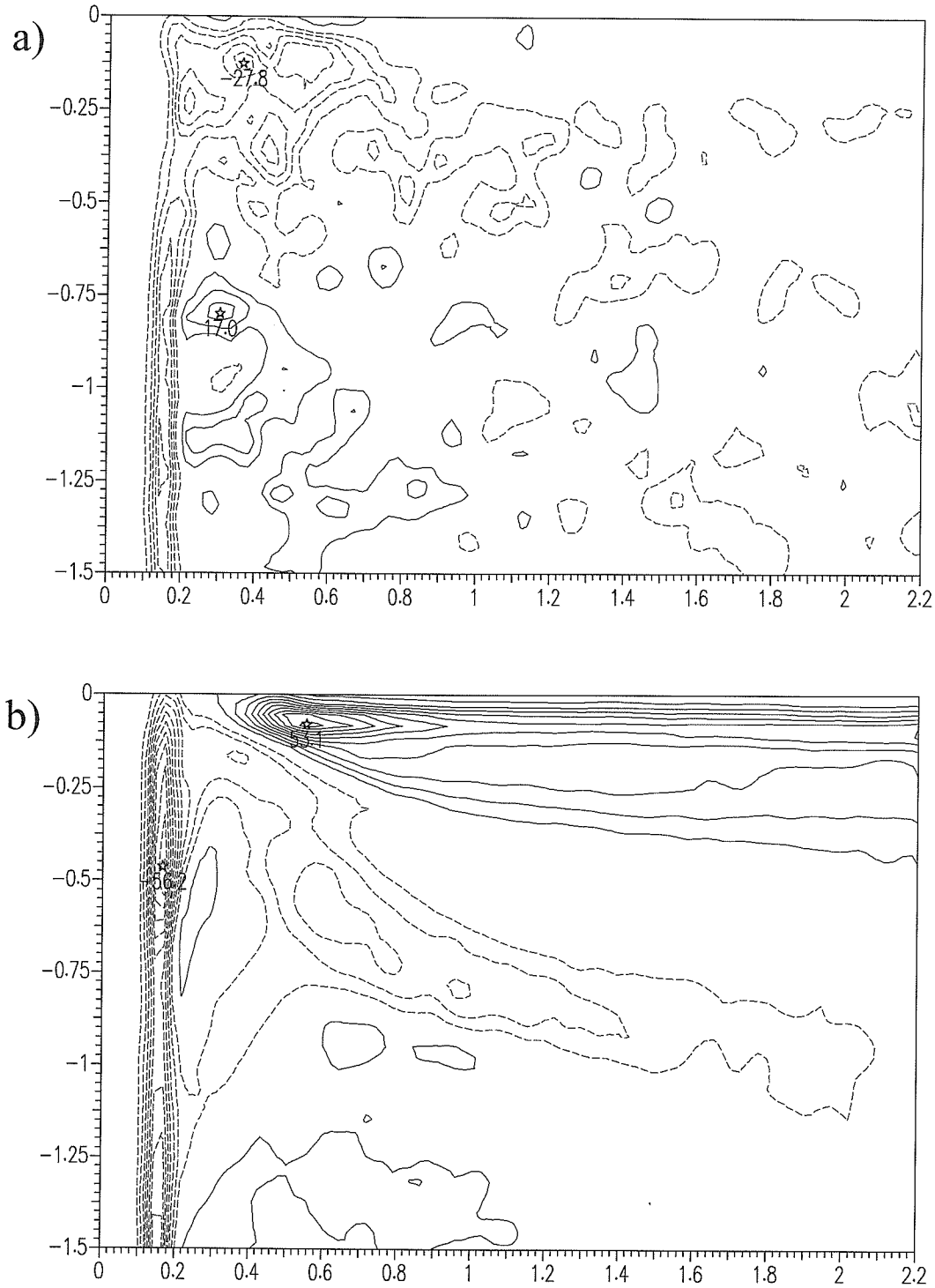

Figure 4.38: Vorticity (contour levels 5,10,15...1/s) field for (a) clean case and (b) contaminated case (ridge 7 cm upstream of the cylinder) and Re=350 of the center cross-section.

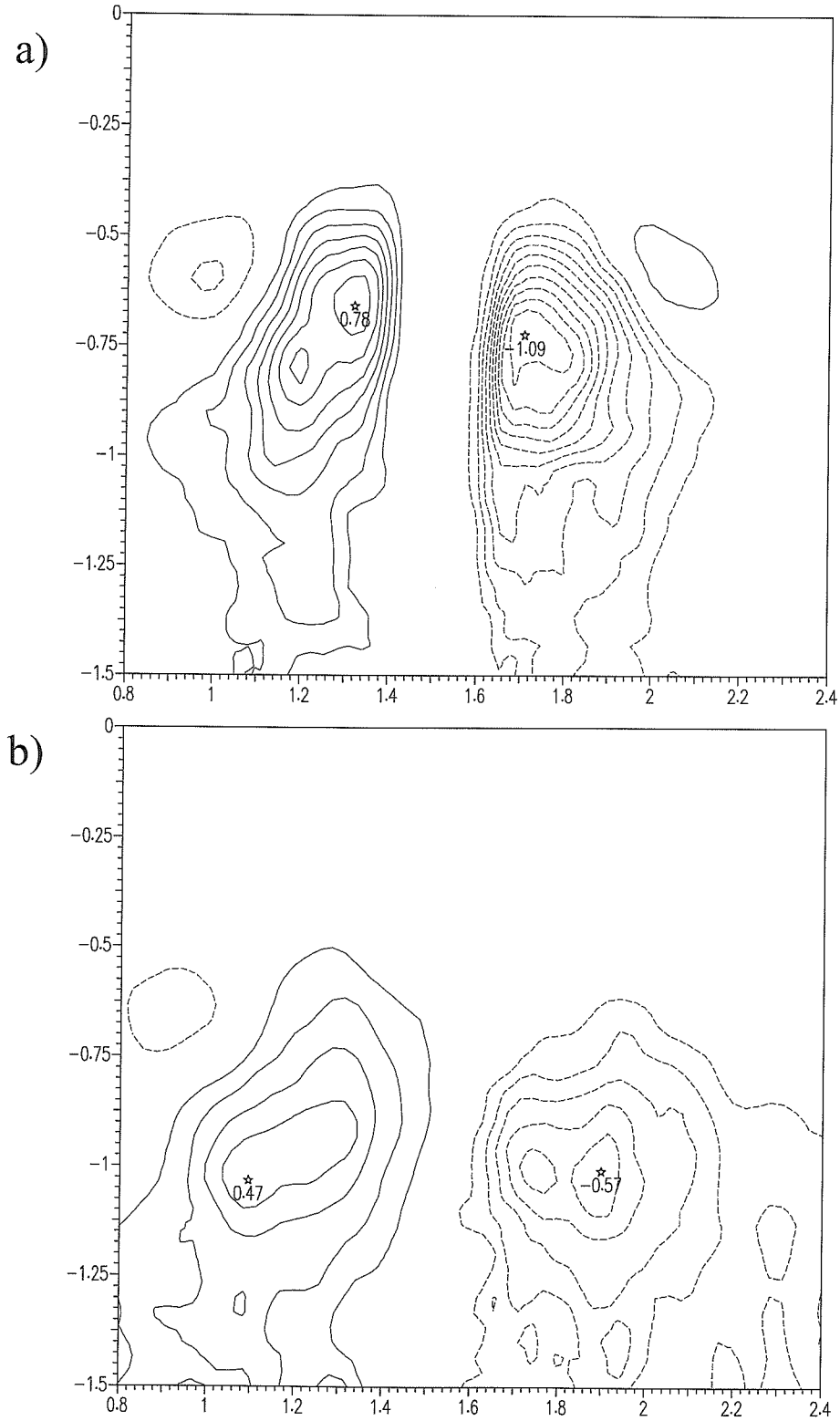

Figure 4.39: Reynolds stress contours (0.1,0.2,0.3...cm^2/s^2) for downstream cross-section where Re=410 and surface contaminated (ridge 7 cm upstream of cylinder) at (a) X=1.75 cm and (b) X=3.75 cm downstream.

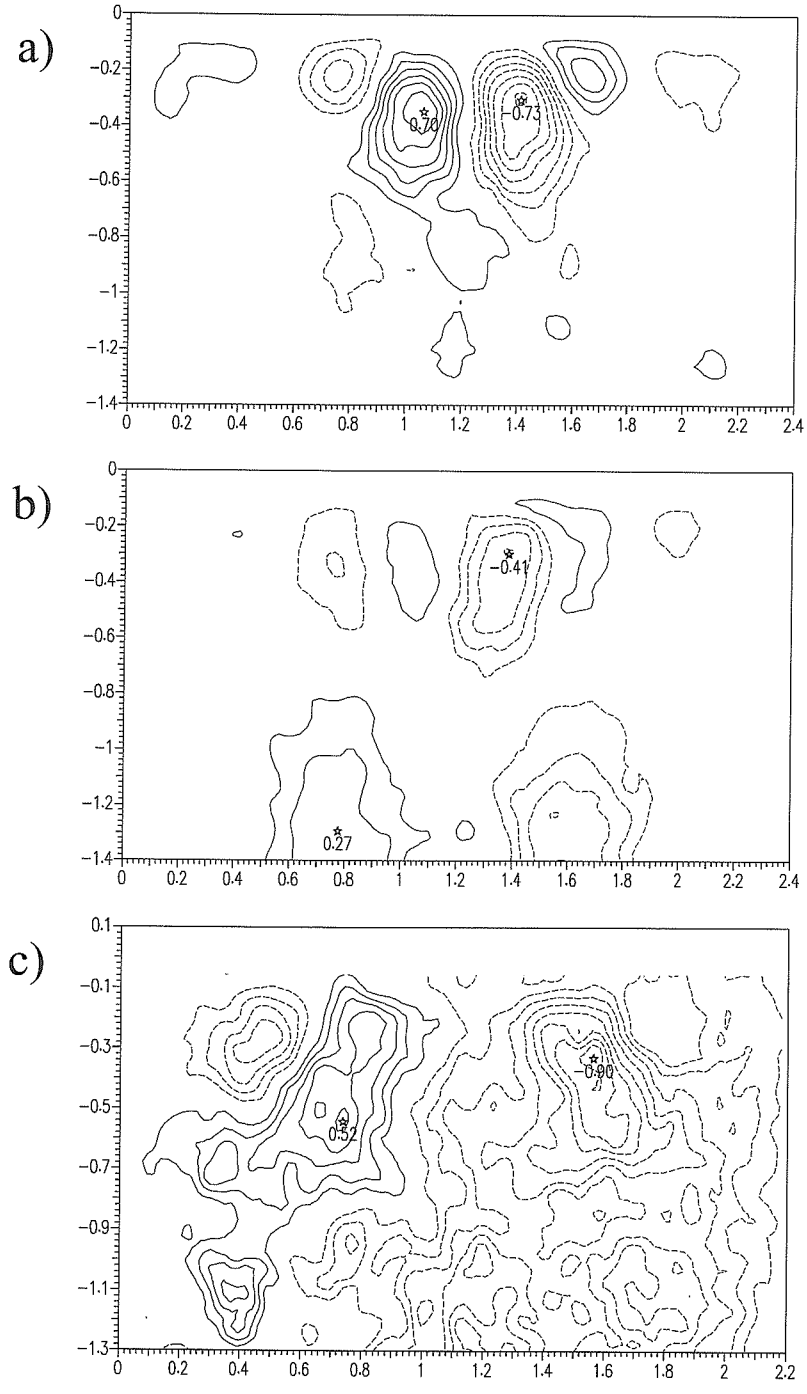

Figure 4.40: Reynolds stress contours (0.1,0.2,0.3... cm^2/s^2) where X=4 cm downstream and (a) ridge is 2 cm upstream of cross-section and Re=410 (b) Re=350 and (c) the cylinder is contaminated and ridge downstream of cross-section and Re=350.

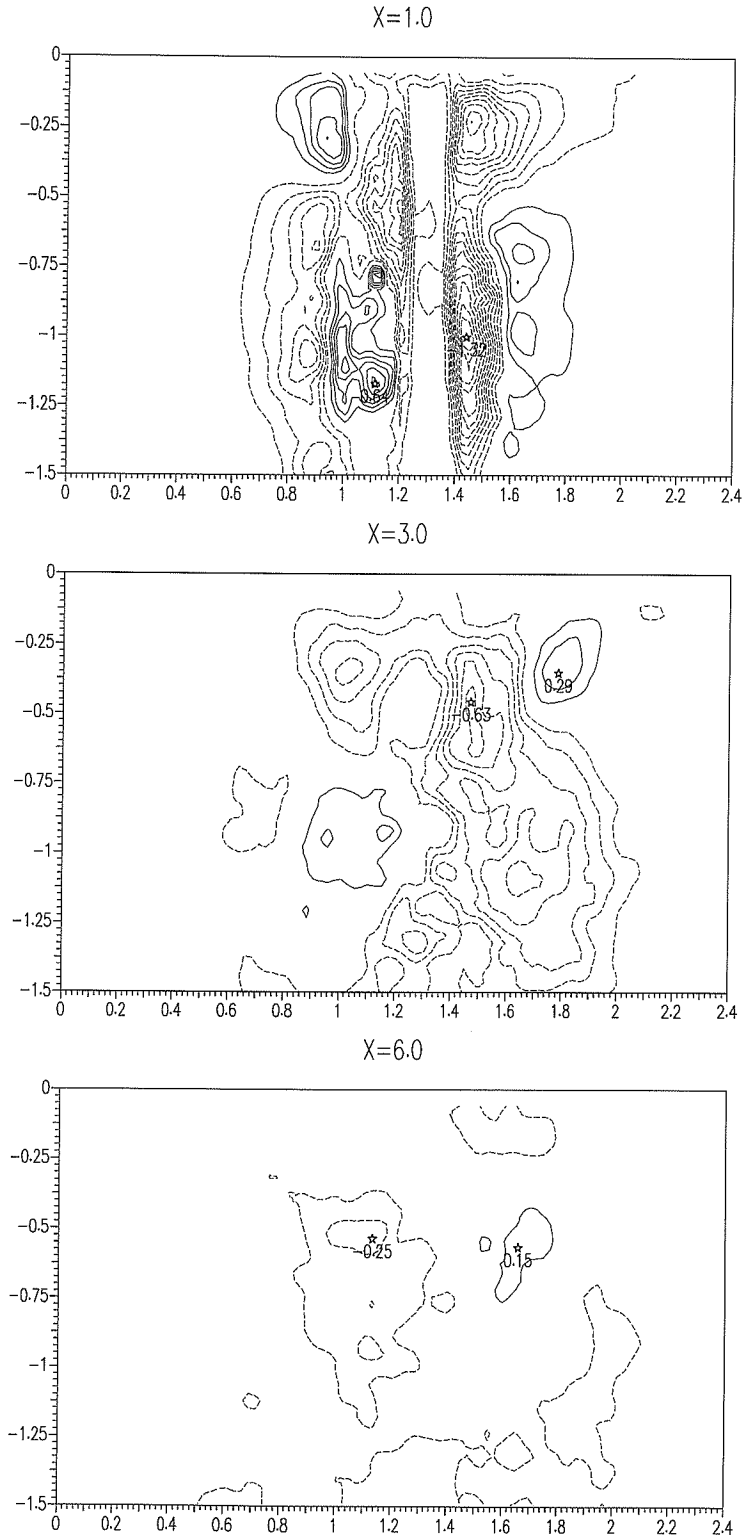

Figure 4.41: Reynolds stress contours (0.1,0.2,0.3,... cm^2/s^2) for the clean case (Re=410) at three downstream cross-sections.

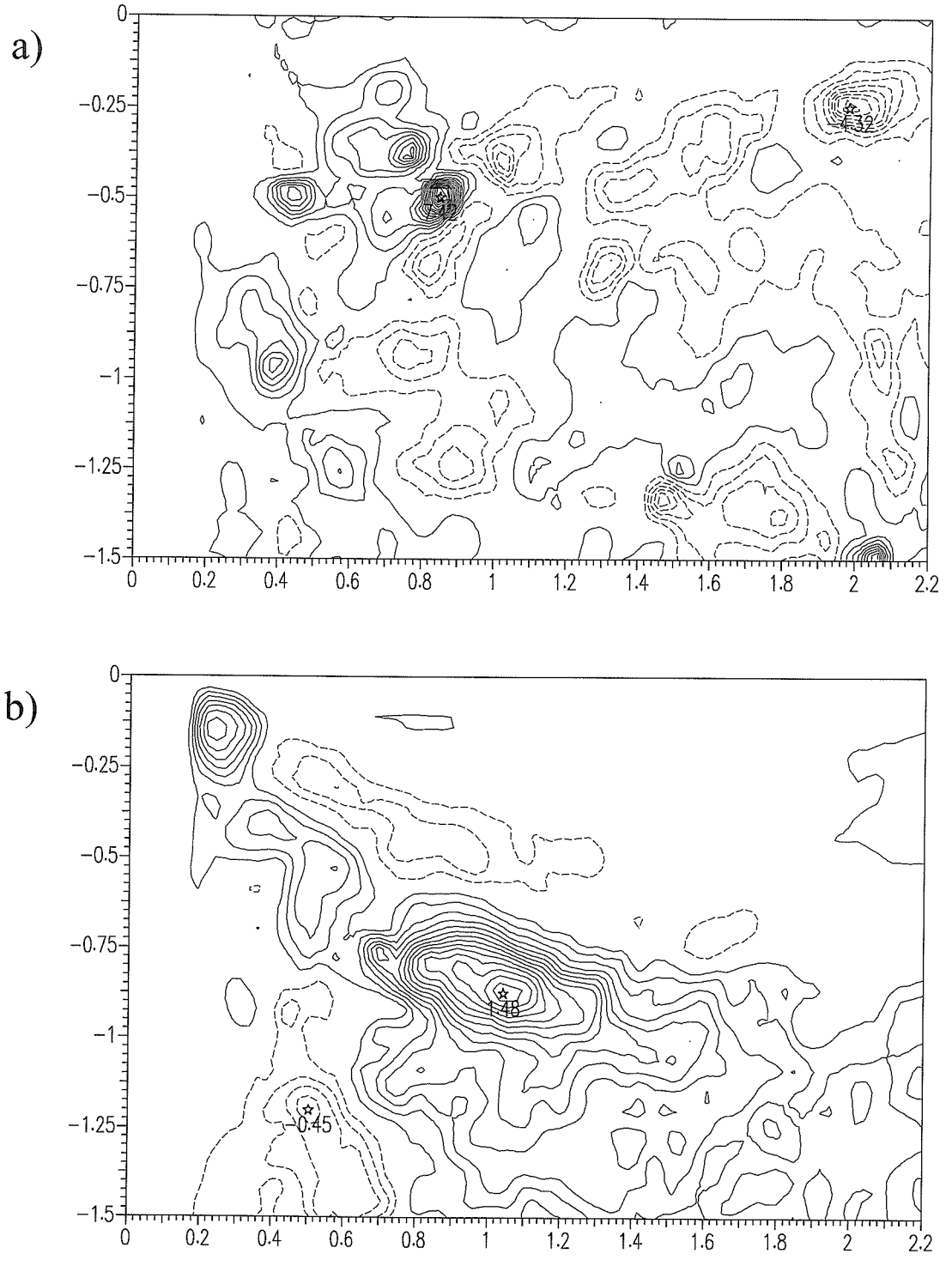

Figure 4.42: Reynolds stress contours for the center cross-section (Re=350) where (a) the surface is clean (contour levels 0.1,0.6,1.1,... cm^2/s^2) and (b) the surface is contaminated (contour levels 0.1,0.2,0.3,... cm^2/s^2).

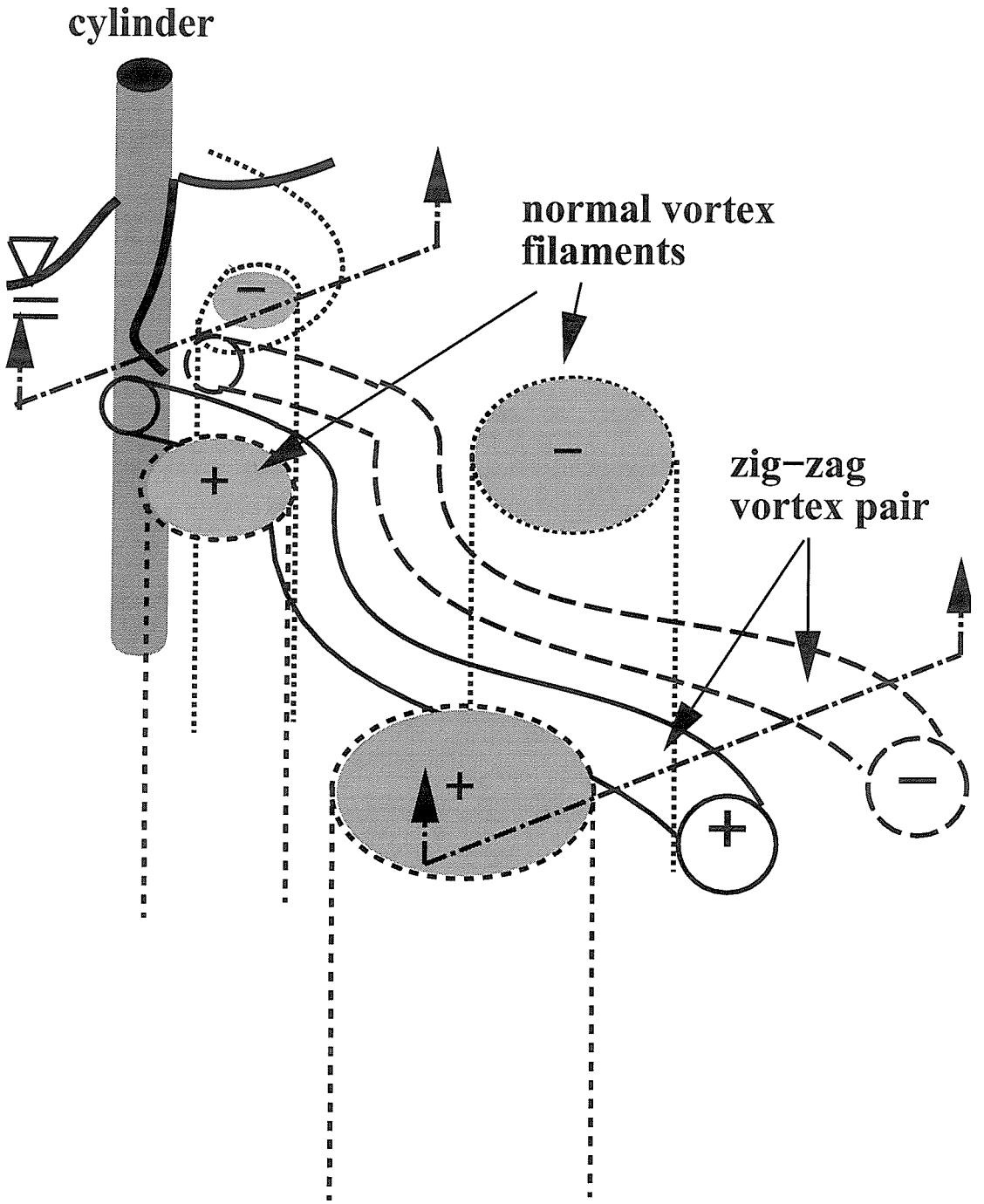

Figure 5.1: Model schematic of cylinder wake for a clean free surface.

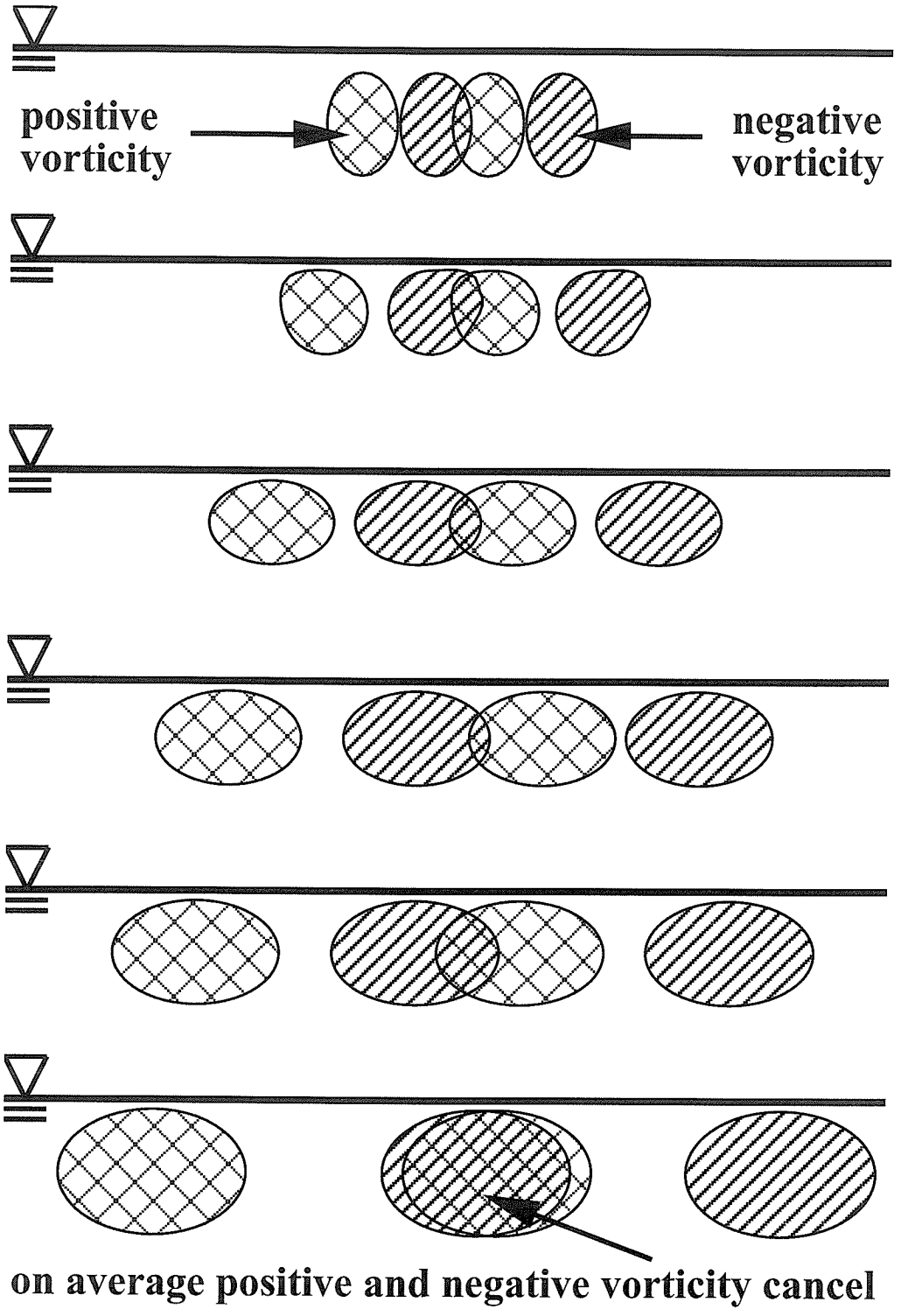

Figure 5.2: Schematic of the six downstream distances for the clean case showing the average placement of the zigzag vortex pair.

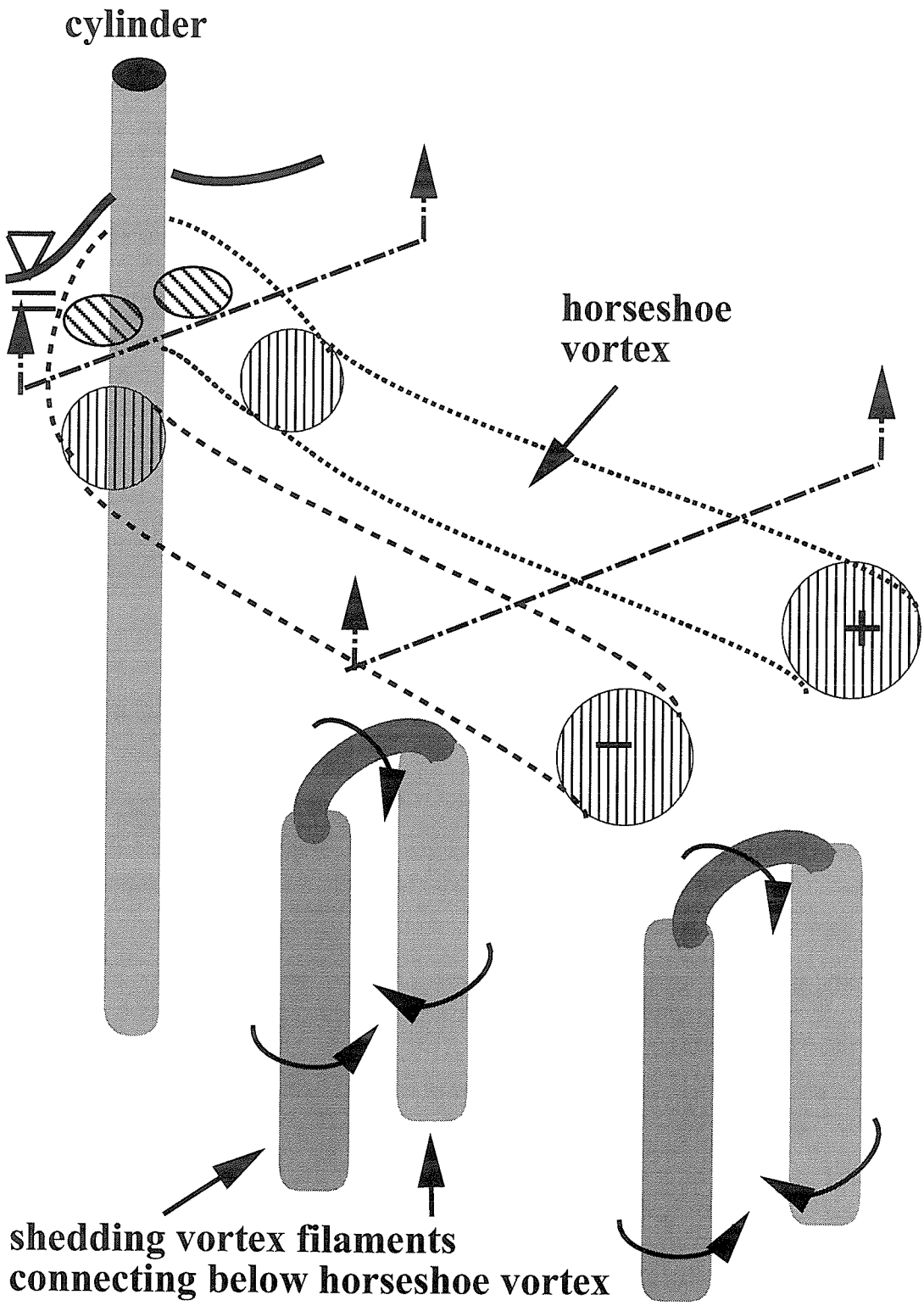

Figure 5.3: Model of cylinder wake where ridge is upstream of the cylinder (contaminated free surface)

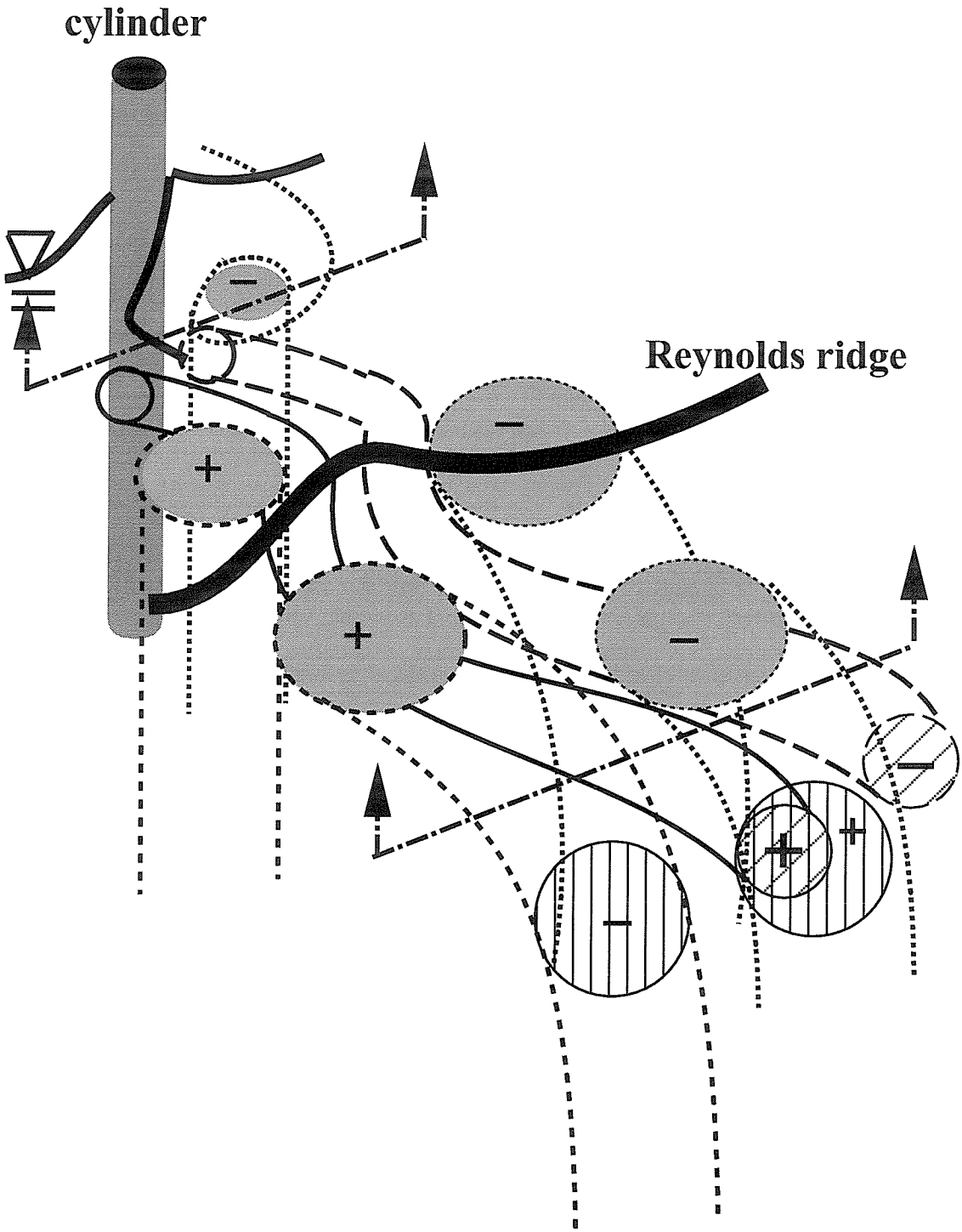

Figure 5.4: Model schematic of cylinder wake for a weak Reynolds ridge.

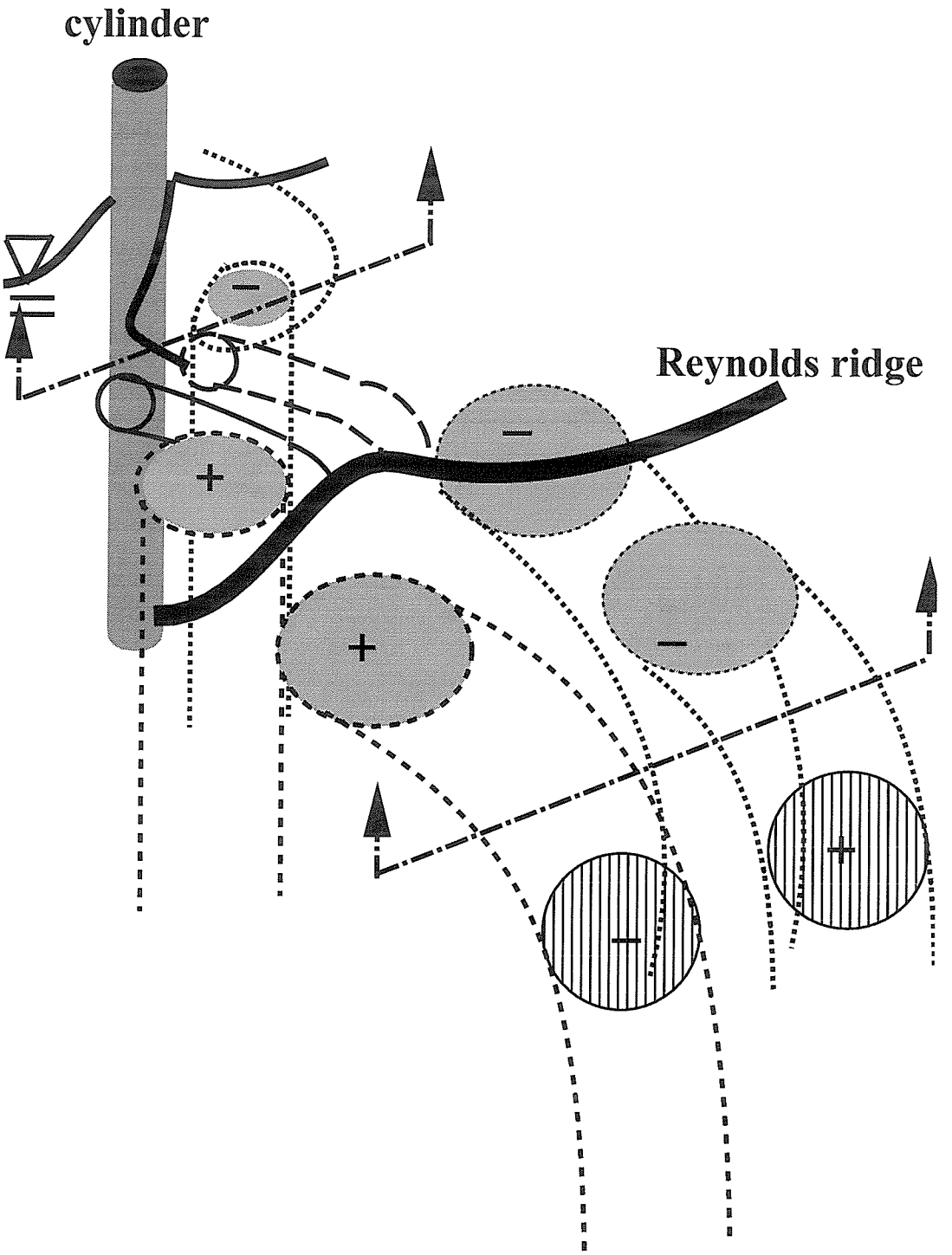

Figure 5.5: Model schematic of cylinder wake for a strong Reynolds ridge (total conversion of vorticity to surface-parallel component).

List of References

Anthony, D. G., Hirsa, A. & Willmarth, W. W. (1991) On the interaction of a submerged turbulent jet with a clean or contaminated free surface. *Phys. Fluids* **A 3** pp.245-247

Bernal, L. P., Hirsa, A., Kwon, J. T. & Willmarth, W. W. (1989) On the interactiion of vortex rings and pairs with a free surface for varying amounts of surface active agent. *Pys. Fluids* **A 1** pp.2001-2004

Camp, D. & Berg, J. (1987) The spreading of oil on water in the surface tension regime. *J. Fluid Mech.* **237** pp.23-32

Chang, C. & Frances, E. (1995) Adsorption dynamics of surfactants at the air/water interface: a critical review of mathematical models, data, and mechanisms. *Colloids and Surfaces* **A 100**, pp.1-45

Davies, J. T. (1965) The effects of surface films in damping eddice at a free surface of a turbulent liquid. *Proc. Royal Soc.* **A**, p.290

DiPietro, N. D., Huh, C., & Cox, R. G. (1978) The hydrodynamics of the spreading of one liquid on the surface of another. *J. Fluid Mech.* **84**, pp.529-549

Edwards, D. A., Brenner, H., & Wasan, D. T. (1991) Interfacial Transport Processes and Rheology Butterworth-Heinemann

Foda, M. & Cox, R. G. (1980) The spreading of thin liquid films on a water-air interface. *J. Fluid Mech.* **101** pp.33-51

Gharib, M. & Weigand, A. (1996) Experimental studies of vortex disconnection and connection at a free surface. *J. Fluid Mech.* **321** pp.59-86

Gharib, M. (1992) On some aspects of near surface vortices.

Harper, J. F. (1992) The leading edge of an oil slick, soap film, or bubble stagnant cap in Stokes flow. *J. Fluid Mech.* **237** pp.23-32

Harper, J. F. & Dixon, J. N. (1974) The leading edge of a surface film on contaminated flowing water. *Proc. 5th Australia Conf. on Hydraulics and Fluid Mech.* Christchurch, New Zealand, pp.499-505

Hirsa, A., Harper, J., & Kim, S. (1995) Columnar vortex generation and interaction with a clean or contaminated free surface. *Phys. Fluids* **7** pp.2532-2534

Hirsa, A., Logory, L., Korenowski, G., Judd, C., & Gaines, G. (1995) Velocity field measurement techniques as applied to the interaction of a vortex pair with a free surface *Laser Anemometry ASME* **229** pp.123-129

Jensen, O. E. (1995) The spreading of insoluble surfactant at the free surface of a deep fluid layer. *J. Fluid Mech.* **293** pp.349-378

Kenning, D. & Cooper, M. (1966) Interfacial circulation due to surface-active agents in steady two phase flows. *J. Fluid Mech.* **24** pp.293-306

Lugt, H. J. (1988) Fundamental viscous flow properties at a free surface. *Fluid Dyn. Trans.* **14** pp.1-20

Lugt, H. J. (1987) Local flow properties at a viscous free surface. *Phys. Fluids* **30** pp.3647-3652

Lundgren, T. S. (1988) A free surface vortex method with weak viscous effects. *Proceedings of the Workshop on Mathematical Aspects of Vortex Dynamics*, Leesburg, VA, pp.68-79

Pauken, M. T., Jeter, S. M., & Abdel-Khalik, S. I. (1996) Surface concentration measurement of a spreading monolayer film using a displacement current technique. *App. Sci. Research* **55** pp.261-282

Roesgen, T., Warncke, A., & Gharib, M. (1997) Fluid surface imaging using microlens arrays. *submitted to Exp. in Fluids*

Rood, E. P. (1995) Free surface vorticity., chapt. 17 in Fluid Vortices S. Green (ed.), Kluwere Academic Publishing, Norwell, MA

Scott, J. C. (1982) Flow beneath a stagnant film on water: the Reynolds ridge. *J. Fluid Mech.* **116** pp.283-296

Scriven, L. E. (1960) Dynamics of a fluid interface. *Chemical Eng. Sci.* **12** pp.98-108

Sellin, R. H. J. (1968) *Nature* **217** pp.536-538

Tryggvason, G., Abdollahi-Alibeik, J., Willmarth, W., & Hirsa, A. (1992) Collision of a vortex pair with a contaminated free surface. *Phys. Fluids* **A 4** pp.1215-1228

Tsai, W. & Yue, D. (1995) Effects of soluble and insoluble surfactant on laminar interactions of vortical flows with a free surface. *J. Fluid Mech.*

Willert, C. E. (1992) The interaction of modulated vortex pairs with a free surface. Ph.D. thesis, UC San Diego

Willert, C. E. & Gharib, M. (1991) Digital particle image velocimetry *Exps. Fluids* **10** pp.181-193

Williamson, C. (1996) Vortex dynamics in the cylinder wake. *Annu. Rev. Fluid Mech.* **28** pp.477-539